Probing and Controlling Electron Dynamics at the Attosecond Timescale

by

John Vaughan

A dissertation submitted to the Graduate Faculty of
Auburn University
in partial fulfillment for the Degree of
Doctor of Philosophy

Auburn, AL
May 1, 2021

Approved by

Guillaume Laurent, Chair, Professor of Physics
Michael Fogle, Professor of Physics
Michael Pindzola, Professor of Physics
Uwe Konopka, Professor of Physics
Hans-Werner van Wyk, Professor of Mathematics

I would like to dedicate this dissertation to my father and mother,
Charles and Lisa Vaughan, for always believing in me.

Acknowledgements

During the course of my PhD, there were many people that supported me. First, I must give a special thanks to my advisor, Professor Guillaume Laurent. He created the conditions for a world-class research experience, and continues to share his immeasurable quantity of priceless advice. I still remember the day I was introduced to him by Andy Edmonds, and there is no doubt in my mind that was one of the most important events of my life. I am fully certain that the principles and work ethic I carry from my PhD training, to think critically and solve problems, will always remain with me. I would also like to especially thank Dr. Uwe Konopka, who served not only as member of my PhD committee, but as a mentor during my years at Auburn University. He was the first influence in my academic pursuits who showed me that pleasure can be found in learning, and doing things the right way.

I must thank our machinist, Rick Stringer, who possesses an immense wealth of knowledge, technical expertise, and professional character. We worked so closely with him in each and every stage of our group's experimental development. We basically consider him a member of the ASAP group. I also thank Bob Letiecq, our staff service engineer from Coherent Inc., for servicing and showing our group how to tune our laser system, as well as sharing his perspectives from his career and life experiences. I thank Jennifer Morris, Mary Prater, and Glenda Stroud, as well, for their exceptional service in handling our administrative and financial tasks. I thank Max Cichon for his help during the construction phase of our lab when he would lend us a hand to move cargo and lend specialty tools.

I am fortunate to have had such good-natured student colleagues in the ASAP group. I thank Geoffrey for his work creating the DAVIS algorithm, and talks when we shared an office together. I am delighted to have worked with Brady Unzicker, with whom I have had many enjoyable discussions about physics, music, and life in general. I would like to sincerely thank Spenser Burrows for many thoughtful exchanges about physics and life experiences, and invitations to go grab lunch or play trivia. I am also very glad to know Trevor and Swap, and especially enjoy the humor they bring to any situation. They are also beginning to shoulder the responsibilities of the new laboratory and I am certain things are in good hands with them.

I thank my dear friends Mohammadtaghi Soroush, Tyler Markham, Lu Wang, Pierce Jackson, Trevor Hart, Travis Keller, Patrick Gemperline, Stacie Baumann,

and Joshua Hopkins for many fun and unforgettable memories as we pursued our education, careers, and made the most of our young lives.

I thank Professors Uwe Konopka, Mike Fogle, and Michael Pindzola (from the Department of Physics) as well as Professor Hans-Werner van Wyk (University Reader, from the Department of Mathematics and Statistics) for being on my committee. I humbly thank them all for their time and contributions.

I thank Dr. Timothy Gorman and Dr. Tim Scarborough for having me as their guest at The Ohio State University as they conducted attosecond measurements of autoionizing resonances.

I thank Professor Luca Argenti, of the University of Central Florida, for sharing his perspectives and professional advice as one of the foremost theoretical physicists in attosecond science, as I prepared to conclude the measurements for my last study.

I would like to thank Jason Pohly, Advanced Sensors and Systems Branch Manager, Dynetics, who mentored me while I was an intern during my last summer as a graduate student. He introduced me to new computing practices as well as concepts in physics and technology which was a refreshing experience near the end of my doctoral studies.

I thank the U.S. Marine Corps and Marines I served with, for providing the conditions to sharpen my physical and mental discipline. It was an honor to serve in a diverse force alongside some of the finest men and women in our country. Semper Fidelis.

I thank Claire Zhang, for her love and support, as I completed the final stages of my PhD. She was a source of immense encouragement during my final two and a half years that I spent working on my dissertation.

Finally, I thank my loving family. I thank my parents, Charles and Lisa Vaughan for their unwavering support and always believing in me. They brought me into this world and trained me to always do my best, act with integrity, and be curious and creative. I thank my two brothers, Calder and Caleb, for their friendship and all the times we spent together, even as we grew busier each day. I am truly lucky to have such a wonderful family.

Abstract

A recently established attosecond beamline, for studies controlling and probing electron dynamics, has been stabilized with attosecond precision. The design and performance of the active stabilization system is presented. The system uses a continuous wave (CW) laser which is propagated coaxially with the beams in the interferometer. The stabilization is achieved with a standalone feedback controller that adjusts the length of one of its arms to maintain a constant relative phase between the CW beams. The time delay between the pump and probe beams is stabilized within 10 as rms.

Coherent control of photoemission in atoms was performed via attosecond pulse-shaping. The photoelectron emission from argon gas was produced by absorption of an attosecond pulse train (APT) made of extreme ultraviolet odd and even harmonics. The photoemission can be manipulated along the direction of polarization of the light by tuning the spectral amplitude and phase of the pulse. In addition, the APTs produced with a two-color (400-nm plus 800-nm) femtosecond driving field exhibit high temporal tunability, which is optimized for an intensity ratio between the two colors in the range of 0.1% to 5%.

A methodology is demonstrated for isolating the continuum-continuum delays of an atomic target during laser-assisted photoionization. Argon gas is ionized by an APT, and dressed by a probe-pulse in configurations like those reported for the Reconstruction of Attosecond Harmonic Beating by Interference of Two-photon Transitions (RABBITT) technique. Complementary measurements are performed that allow the continuum-continuum delays to be obtained across excitations from 23 eV to 30 eV. These delays are compared to calculations based on the asymptotic approximation of transition matrix elements.

Introduction

The research work completed in this dissertation was carried out at the Auburn's Source of Attosecond Pulses (ASAP) laboratory in the Department of Physics at Auburn University. This laboratory was established in 2016, as the result of the departmental desire to expand its research activity. Currently, the active theoretical and experimental research areas in the department include (1) Atomic, Molecular, and Optical (AMO) Physics, (2) Biophysics, (3) Condensed Matter Physics, (4) Plasma Physics, and (5) Space Physics. The early experimental AMO group has carried out research studies of fundamental atomic and molecular processes through interactions with electron impact and synchrotron radiation. Within the AMO subdivision activities, the ASAP laboratory aims to provide complementary measurement capabilities of the intricate dynamics of atoms and molecules directly in the time domain.

I was the first graduate student to join ASAP, so my PhD spanned from the day the laboratory construction began to the experiments reported in this dissertation. The construction of the lab was led by Dr. Laurent with assistance from myself and valuable contributions from Rick Stringer (our highly skilled and professional machinist), Max Cichon (engineering etaff), and Andy Edmonds (who was an undergraduate at the time). I contributed to, and gained valuable technical experience from, building the attosecond beamline. My scientific contributions include the development of a novel technique to stabilize attosecond pump-probe measurements and leading research of electron dynamics at the attosecond timescale. The group now includes more than a dozen actively involved graduate and undergraduate students, and our members have presented their work in a number of conferences, and had their work published in peer-reviewed journals.

Attosecond Physics is a subfield of ultrafast science. It has its theoretical roots in quantum mechanics, which was originally formulated to describe the wave-particle duality of light and particles, as well as light-matter interaction. Before ultrafast science arrived, the most popular experiments to measure quantum phenomena involved particle accelerator collisions, photodissociation, and photoionization, which were unable to measure the temporal aspects for the fundamental physics of atoms, molecules, and complex systems. Attosecond physics uses pulses of light with attosecond duration to measure quantum phenomena at the same timescale.

To date, it is the most precise method to measure the dynamics of light matter interaction including photoionization, electron rearrangement of atomic systems, and resonant phenomena. This is possible through pump-probe experiments, where an attosecond pulse excites the system which absorbs the light and produces an electron wavepacket which acts as a replica of the attosecond pulse. A second pulse of laser light is overlapped with the attosecond pulse, and as the time-delay between the pulses is changed with time, the dynamics of the system is interrogated. The field of attosecond physics continues to grow at a rapid pace as the technology and measurement techniques proliferate.

Our research line represents the first and only Attosecond Physics group in the state of Alabama. At the National Level, major laboratories exist at the University of Central Florida, The Ohio State University, and University of California, Berkeley. At the international level, major laboratories exist across Europe. There are other groups across the country and around the world, that are established or starting up, but the field is relatively small compared to most scientific disciplines. Currently, our principal areas of research in ASAP include the development of novel sources of attosecond pulses of light in the extreme ultraviolet (XUV) wavelength regime, the development of innovative methods to characterize the temporal profile of such attosecond pulses, and their application to the study of ultrafast dynamical processes in matter down to the attosecond timescale.

Contents

List of Figures

List of Acronyms

APT	Attosecond pulse train.
ASAP	Auburn's Source of Attosecond Pulses.
BBO	Beta Barium Borate.
CEP	Carrier-envelope phase.
COLTRIMS	COLd-Target Recoil Ion-Momentum Spectroscopy.
CPA	Chirped pulse amplification.
DTFT	Discrete-time Fourier transform.
EWP	Electron wavepacket.
FFT	Fast Fourier transform.
FWHM	Full width at half maximum.
GD	Group delay.
GVD	Group velocity dispersion.
HHG	High harmonic generation.
iPROOF	improved Phase Retrieval by Omega Oscillation Filtering.
IR	Infrared.
NIR	Near infrared.
PAD	Photoelectron angular distribution.
RABBITT	Reconstruction of attosecond harmonic beating by interference of two-photon transitions.
SAE	Single active electron approximation.
SAP	Single attosecond pulse.
SFA	Strong-field approximation.
TDSE	Time-dependent Schrödinger equation.
TOF	Time of flight.
TSM	Three-step recollission model of high harmonic generation.

UV	Ultraviolet.
VMI	Velocity map imaging.
XUV	Extreme ultraviolet.

'We have to remember that what we observe is not nature in itself, but nature exposed to our method of questioning.'

— Werner Heisenberg

1 Fundamentals of Attosecond Science

Contents

1.1 The Path to Attosecond Technology

In 2001, the advent of attosecond light pulses expanded our domain of observations to the timescales of atomic and molecular physics. An intuitive example for such a timescale comes from considering a semiclassical ground-state hydrogen atom, where an electron circulates around a proton. The period of this orbit can be calculated to be 152 as. Indeed, most of the early studies have been on simple atomic systems in

the gas phase, but the field of attophysics has matured. Applications are currently being made to investigate the ultrafast electronic processes in solid materials and surfaces [1], as well as liquid phase [2]. Currently, a new focus of theoretical studies on the ultrafast characteristics in biological systems [3] and photovoltaics [4] direct the attosecond community to more incredible advancements in the next few years.

1.1.1 A Note on Physical Units

To avoid confusion with units, we observe the following conventions. In the attosecond physics community, we almost always use energy units of eV for photon energy, charged particle kinetic energy, and ionization energy. In equations and expressions involving energy, like Equation 1.6, assume units of eV. In the atomic molecular and optical (AMO) community, which often uses atomic units, energy and frequency are on the same footing. In this dissertation, sometimes characters, like Ω, will represent frequency or energy. Context will decide whether characters represent energy (Equation 1.6), or frequency (Equation 1.1). Furthermore, when atomic units are in use (especially in Chapter 4 and Chapter 5), it will be stated explicitly beforehand. In all other expressions, such as Equation 1.4, the reader should assume the use of SI units.

1.1.2 Laser Seeds

Attosecond pulses are not lasers, but they are the product of a nonlinear process called high harmonic generation (HHG) which is driven by ultrashort pulse lasers. Unlike continuous wave lasers, which are nearly monochromatic, or ultrashort pulse lasers, which have a bandwidth centered about a central wavelength, attosecond pulses consist of a comb of frequencies (Figure 1.1) made of the harmonics of the driving wavelength extending into the extreme ultraviolet (XUV). HHG is a nonlinear light-matter interaction which only occurs if the seed laser is used at an extremely high intensity. A Ti:sapphire laser, such as the one we use at the Auburn Source of Attosecond Pulses (ASAP), represents a typical example of a modern commercial ultrashort laser. The optical peak power of a 1.5-mJ,

35-fs pulse rivals the output of a modern nuclear power plant ($\sim 10^9$W) by a factor of forty (at least within the duration of the pulse). The reader may check this with the formula, $P = 0.94 \times E_{pulse}/\tau_{pulse}$, where the unitless factor of 0.94 is used for a Gaussian pulse shape [5]. As HHG is a nonlinear effect, it relies more on intensity. Beams are focused very tightly to reach intensities of the order of 10^{14}W/cm^2 for HHG to take place. The discovery of HHG circumvented the obstacles of trying to build XUV lasers by conventional laser assembly [6]. The minimum threshold pump power for XUV and soft x-ray light is orders of magnitude larger than that required for visible wavelengths. Additionally, constructing a laser resonant chamber that can support both XUV attosecond pulse bandwidth, and the required pumping intensities is a great challenge.

1.1.3 High Harmonic Generation as a Coherent XUV Radiation Source

Although HHG produces a far smaller amount of XUV and soft X-ray radiation compared to X-ray free electron lasers and synchrotrons, HHG is the only source of attosecond pulses. The attosecond pulses from HHG are produced when the fundamental wavelength of the laser driving the process is converted to many of its higher harmonics. The most striking characteristics of the resulting attosecond pulse spectrum, as seen in Figure 1.1, is that at lower harmonic energies, the power drops rapidly, then continues as a plateau before a cutoff harmonic energy is reached. The measurements of Paul *et. al.* [7] experimentally showed that the product of HHG, driven by an IR femtosecond laser, consists of a phase-locked harmonic spectrum belonging to a train of pulses. The pulses are produced twice per optical cycle of the driving laser. Due to the inversion symmetry of the system, only odd harmonics are produced in this scheme. This is fundamentally due to angular momentum quantum selection rules that are followed. During HHG, a multiphoton process, each photon contributes a change in angular momentum of $\Delta l = \pm 1$. An even number of transitions (that would lead to even harmonics) will not allow a possibility of $\Delta l = \pm 1$ in the final step of the TSM. Developments have resulted in

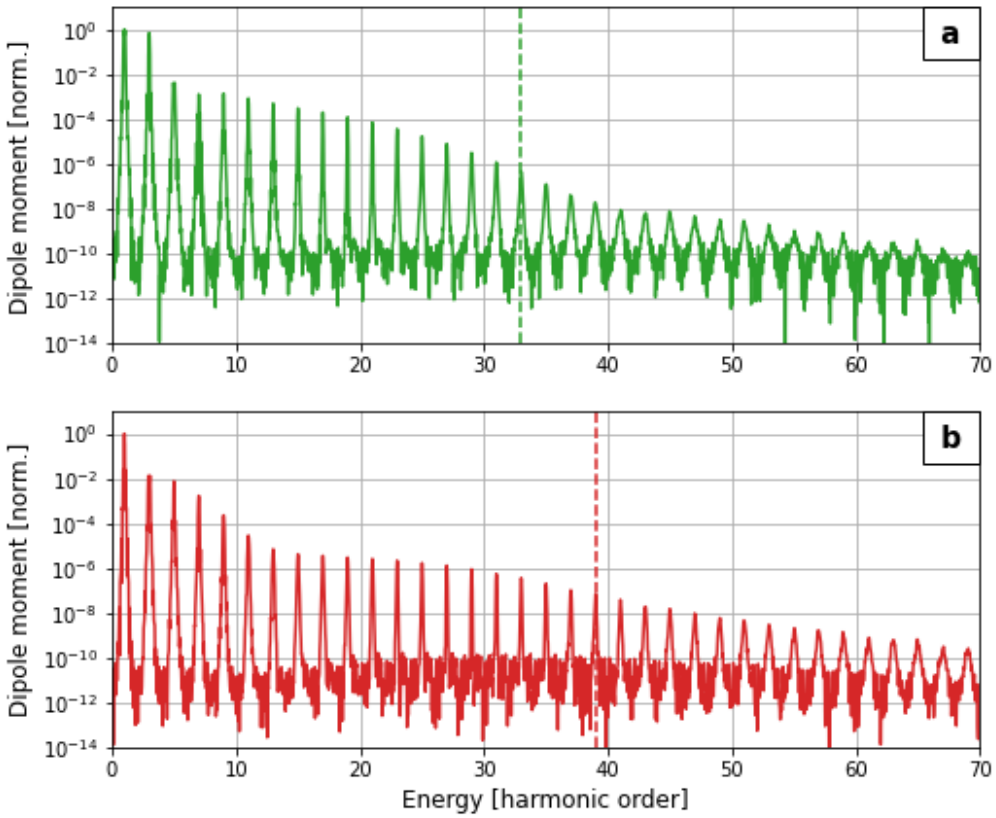

Figure 1.1: An HHG spectrum for Argon (a) and Helium (b). Calculations are made with an in-house Strong Field Approximation algorithm. The Fourier transform of the dipole moment is calculated using atomic units, and log scale is used for the y-axis. The spectrum displays the abrupt drop at lower energies, a plateau extending toward the XUV energy range, and the cutoff at roughly an order of magnituded below the plateau height. The simulation was calculated for an 800-nm laser at an intensity of 2×10^{14}W/cm^2 and 40-fs pulse duration. The dashed lines indicate the harmonic cutoff.

ways to also create the even harmonics by superimposing the second harmonic of the laser in the HHG generation. Furthermore, techniques like polarization gating [8, 9] have been demonstrated to yield single attosecond pulses (SAPs). As the attosecond pulses and probing techniques become more sophisticated, the studies in atomic, molecular, and condensed matter research continue to flourish.

1.2 Attosecond Pulse Generation

Although high intensity laser–atom interactions in HHG can be described by solving the time-dependent Schrödinger equation (TDSE), the numerical computations for even a single atom is tedious. Two important theoretical tools to explain harmonic radiation from HHG were developed in the nineties. The first was a semi-classical model [10] to provide a qualitative description of the harmonic spectrum. It gives a layman's description for HHG, and predicts the harmonic cutoff. The other was the strong-field approximation which provided a quantitative description of the harmonic yield [11]. These descriptions are still used today, and work in a variety of schemes without loss of generality.

1.2.1 Semi-classical Model for High Harmonic Generation

In 1993, P. B. Corkum introduced what is famously known as the three-step recollision model [10] which offers a semiclassical description of what happens during HHG. The three-step model is useful for theoretically predicting the harmonic bandwidth produced in an Attosecond Pulse Train (APT). Early observations of high harmonics by HHG were performed with wavelengths as short as 248 nm, and were the result of focusing the driving laser beams to high intensity. Shorter laser wavelengths were thought to be the best choice for generating higher harmonic energies, but the three-step model shows that longer wavelengths extending into the mid-infrared are a better choice [12].

The three-step recollision model (TSM) of HHG can be summarized as a sequence of an electron tunneling from its parent atom, then accelerating in a strong oscillating laser field, and finally, recombining to its parent ion. This TSM is depicted in Figure 1.2. In step 1, an electron resides in the ground state of its parent atom. When immersed in a strong laser field with intensity of the order of $10^{14}\mathrm{W/cm}^2$ the bound electron can tunnel through the atomic potential distorted by the driving laser. In step 2, the electron is treated classically as a free electron in the presence of an oscillating electric field. In step 3, the electron returns to the ion and releases its buildup of kinetic energy in the form of a harmonic of the driving laser. I present

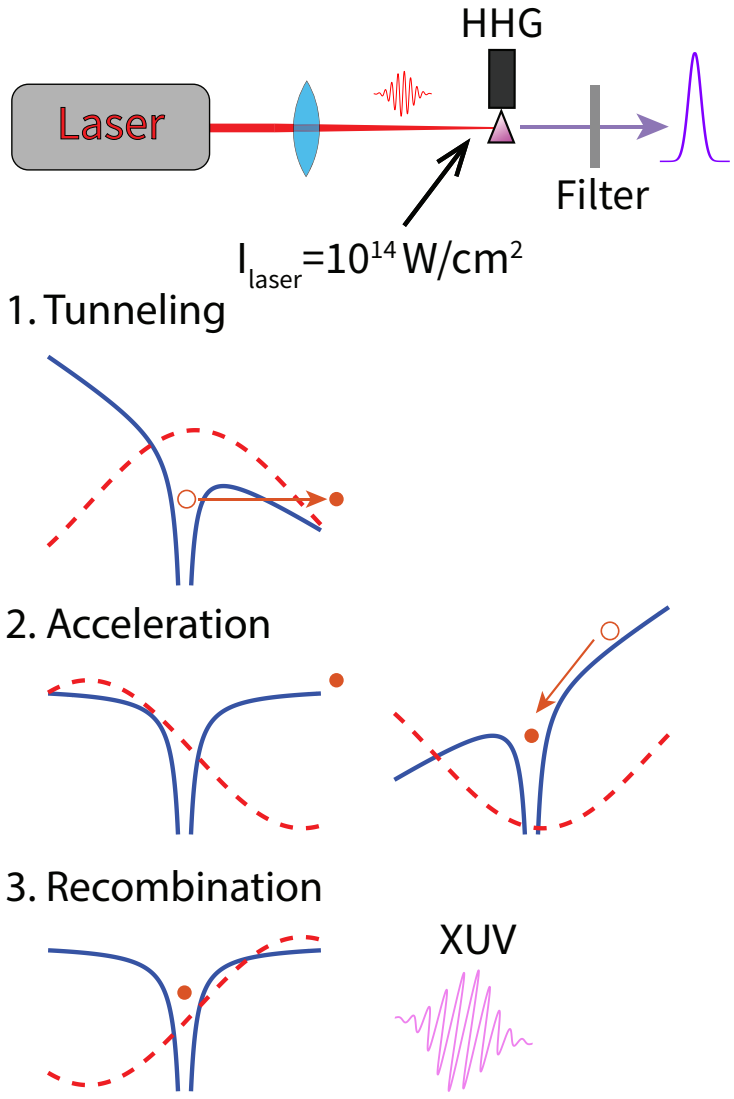

Figure 1.2: The three step model for which an atomic system is in the presence of an intense IR laser. In the figure, the blue lines represent the potential, the orange dot is the electron, and the red dashed line represents the IR laser field driving the HHG process. Near the peak of the wave, an electron will (1) tunnel through the weakened potential, (2) accelerate in the field acquiring energy, and (3) recombine to emit harmonics of the IR fundamental.

a derivation below for the TSM, which is shown very nicely in [13]. For simplicity, let us start by considering the one-dimensional problem (with linear polarization of the laser) where the initial position x_0 and velocity v_0 are zero at the instant after tunneling, the equation of motion is simply

$$\frac{d^2}{dt^2}x(t) = -\frac{e}{m_e}E_L\cos(\omega_L t), \tag{1.1}$$

where E_L is the field of the laser, e and m_e are the electron charge and mass, and ω_L is the laser frequency. In the second step, the electron is accelerated in the field acquiring surplus kinetic energy. In step 3, the electron recombines with the ion and releases the excess energy Ω by

$$\Omega = I_p + 2U_p\sin^2(\omega_L t). \tag{1.2}$$

The term I_p is the ionization potential of the HHG gas in eV, and U_p is called the ponderomotive energy. The ponderomotive energy is also the cycle-averaged kinetic energy of the free electron in the field. It is calculated as

$$U_p = \langle E_K \rangle = \frac{1}{\tau}\int_0^\tau \frac{1}{2}m_e v^2 dx \tag{1.3}$$

where $\tau = 2\pi/\omega_L$. After finding the velocity by integrating Equation 1.1 and substituting that into Equation 1.3, one can find the result of

$$U_p = \frac{e^2 E_L^2}{4m_e\omega_L^2}. \tag{1.4}$$

Another way to understand this expression is in terms of laser intensity I_L and central wavelength λ_L. This offers an interesting qualitative view - the ponderomotive energy is proportional to the intensity, and the square of the central wavelength ($U_p \propto I_L\lambda_L^2$). It is this behaviour that shows why longer wavelengths are better at producing higher harmonic cutoffs.

For the semiclassical treatment to be valid, the ratio of the time which the electron needs to tunnel t_{tun} through the potential barrier compared to the time the barrier is kept lowered by the laser field T_0 should be small. This information is inside the Keldysh parameter [14], from a theory developed in the sixties for

ionization in the presence of a strong field. It is a dimensionless quantity that can be expressed in terms of U_p and I_p as well,

$$\gamma = \frac{t_{tun}}{T_0} = \sqrt{\frac{I_P}{2U_P}}. \tag{1.5}$$

A major strength of the semiclassical model is that it predicts the cutoff photon energy Ω_{max} with good accuracy. An expression for the maximum photon energy in eV is

$$\Omega_{max} = I_p + E_{K,max}. \tag{1.6}$$

Where $E_{K,max}$ is the maximum kinetic energy the electron collects during step 2 of the recollision model. This return kinetic energy depends sensitively on its release time. This release time t' is the moment at which the electron has tunneled from the atom. With every release time, there is a recombination time solution that can be expressed in terms of the period of the laser T_0. If one wishes to see this relationship, then it's necessary to begin by integrating Equation 1.1 twice with integral limits from the release t' to recombination time t. This will return a result for the position,

$$x(t) \propto \frac{1}{2}\left[\cos(\omega_L t) - \cos(\omega_L t') + \sin(\omega_L t')\omega_L(t - t')\right]. \tag{1.7}$$

At the return time t, the position $x(t)$ is zero. This leads to a new form

$$\cos(\omega_L t) - \cos(\omega_L t') = \sin(\omega_L t')\omega_L(t - t'). \tag{1.8}$$

Using Equation 1.8, we can graphically display the dependence of return time to release time at various instants within what is referred to as the Kramers-Henneberger frame. Figure 1.3 shows a graphical solution for Equation 1.8. In the Kramers-Henneberger reference system, the parent ion moves in a cosine displacement with time, while the electron has linear displacement. There is no analytical solution, but the solution can be seen graphically and solved for numerically. It can be shown that solutions exist for trajectories having release times within angular phases of 0 to $\pi/2$. Anything else results in the electron never returning (in the figure the line will not cross the cosine a second time). With these

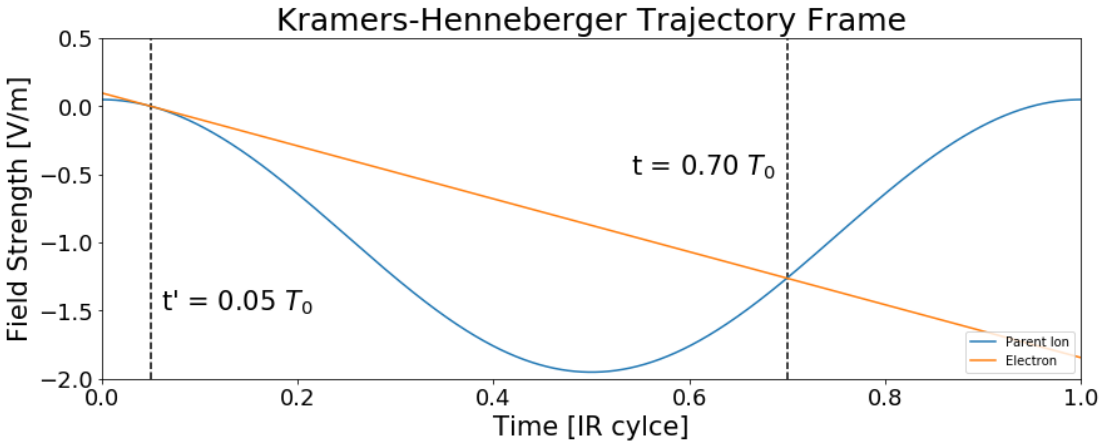

Figure 1.3: An example of an electron trajectory when released at a time $t' = 0.05T_0$. In terms of the phase of the release time itself, trajectories where the electron returns to the parent ion correspond to release phases of 0 radians to $\pi/2$ radians (0 to $0.25T_0$)

pairs of release time and return time, the maximum return kinetic energy can be established by an eyeball extrapolation after plotting the ratio of kinetic energy to ponderomotive energy versus emission phase (Figure 1.4.b)

$$\frac{E_K}{U_p} = 2\left[\sin(\omega_L t) - \sin(\omega_L t')\right]^2. \tag{1.9}$$

The maximum in the plotted return kinetic energy versus release time indicates a maximum energy of about $3.17U_P$ at release phase of $0.05 \times 2\pi$[rad] (return phase of $0.7 \times 2\pi$[rad]). Therefore the maximum harmonic photon energy can be calculated with the following well-known formula

$$E_{\Omega,max} = I_p + 3.17U_p. \tag{1.10}$$

Equations 1.4 and 1.10 together allow one to calculate the cutoff harmonic order.

1.2.2 Strong-Field Approximation for Dipole Radiation

One way in which the semi-classical model falls short is its inability to provide the strength of the harmonic spectrum. Although the harmonic spectrum can be calculated by the TDSE, this method is computationally expensive. The Strong Field Approximation (SFA) allows us to find an analytical solution for harmonic yield. For thorough derivations, please see [13, 15].

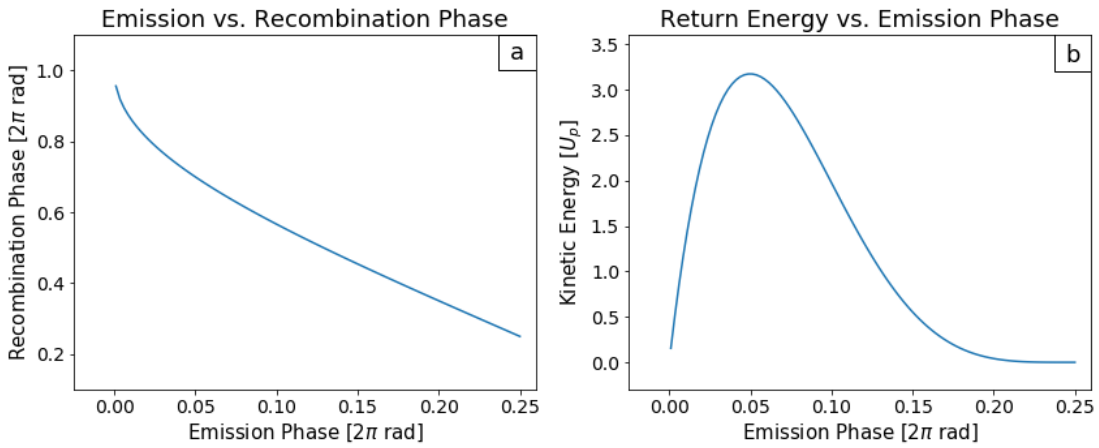

Figure 1.4: In (a), the dependence of the recombination phase to the emission phase is plotted from the numerical solutions to Equation 1.9. In (b) The return kinetic energy versus recombination indicates that the maximum return kinetic energy is $3.17U_p$ for a release time of $0.05T_0$.

To use SFA, we must use two assumptions that simplify the derivation. The first assumption is that the harmonic fields are the result of dipole radiation. In this model, electrons driven by the laser oscillate about the nucleus. Sufficiently far from a classical dipole, the radiated electric field is

$$E_{dip}(t, R, \theta) = \frac{d_0\omega^2}{4\pi\epsilon_0 c^2}\frac{\sin(\theta)}{R}\mathrm{e}^{i\omega(t-R/c)}. \tag{1.11}$$

Here, d_0 is the magnitude of the dipole moment, R is the distance from the dipole, θ is the angle between the R vector and the dipole axis, and ω is the dipole frequency of oscillation. In quantum mechanics, the dipole moment in atomic untis is $-\boldsymbol{r}$. In atomic units, ($\hbar = m_e = e = a_0 = 1$), where a_0 is the Bohr radius. It can be calculated with the expectation value

$$\boldsymbol{r} = \langle\Psi(\boldsymbol{r}, t)|\boldsymbol{r}|\Psi(\boldsymbol{r}, t)\rangle \tag{1.12}$$

where $\Psi(\boldsymbol{r}, t)$ is the time-dependent wavefunction, and we use the bra-ket notation.

In the second assumption, we assume the single active electron (SAE) approximation. This reduces the complexity of finding an analytical solution for an otherwise many-electron problem. The assumption is that in the atom or molecule, only one electron responds to the laser field. In this regime, the Schrödinger

equation takes the form

$$i\frac{\partial}{\partial t}\Psi(\boldsymbol{r},t) = \left(-\frac{1}{2}\nabla^2 + V(r)\right)\Psi(\boldsymbol{r},t), \tag{1.13}$$

Where $V(r) = -\frac{1}{r}$. The wave function is written as the product of its spatially-dependent and time propagating part as

$$|\Psi(\boldsymbol{r},t)\rangle = |0\rangle\, e^{-i(E_g t)}, \tag{1.14}$$

where $|0\rangle$ represents the ground state, and E_g is the ground state energy.

The SFA itself invokes two simplifications. First, it assumes that only ground state electrons are excited into the continuum; no excited bound states or resonances are involved. Secondly, once in the continuum, the electron experiences a dipole potential from the laser, while the Coulomb potential is considered negligible by comparison. The Schrödinger equation now has the form where $V(r) = 0$

$$i\frac{\partial}{\partial t}\Psi(\boldsymbol{r},t) = \left(-\frac{1}{2}\nabla^2 - \hat{\boldsymbol{\varepsilon}}\cdot\boldsymbol{r}\right)\Psi(\boldsymbol{r},t), \tag{1.15}$$

the term $\hat{\boldsymbol{\varepsilon}}$ is the laser polarization. The total wave function for Equation 1.15 can be written in terms of the bound state and free electron continuum state $|v\rangle$ in the following way:

$$|\Psi(\boldsymbol{r},t)\rangle = e^{-i(E_g t)}\left[a(t)\,|0\rangle + \int d^3\boldsymbol{v}\, b(\boldsymbol{v},t)\,|v\rangle\right]. \tag{1.16}$$

The dipole can be calculated by substituting Equation 1.16 into Equation 1.12. If slowly varying terms and continuum-continuum transitions are neglected, what remains is

$$\boldsymbol{r} = \int d^3\boldsymbol{v}\, a^*(t) b(\boldsymbol{v},t)\boldsymbol{d}^*(\boldsymbol{v}) + c.c. \tag{1.17}$$

An insightful interpretation comes from this equation, which contains the product of the ground state and electron wavepacket (EWP) amplitudes inside. Evidently, if the ground state is depleted, the harmonic generation cannot occur. In other words, the harmonics are produced as the result of interferences of the EWP and ground states. If one wants the harmonic strength, they must take the Fourier transform of the dipole, Equation 1.17.

1.3 Applications

The advent of attosecond duration, XUV light pulses opened the door for experimentalists to probe the time domain of electron processes in atoms, molecules, and complex systems. This revolution is best understood by highlighting several remarkable measurements. First, the two most important attosecond measurement schemes will be introduced. Then, we will concentrate on two major applications of attophysics, temporal measurements of electron transitions, and control of electron photoemission from atoms. These experiments are not only historically significant in the attosecond community, they will serve as background to measurements documented later in this dissertation.

1.3.1 Pump-Probe Schemes

The two most widespread techniques employed for attosecond pump-probe measurements are the attosecond streak camera [16, 17] and the reconstruction of attosecond harmonic beating by interference of two-photon transitions (RABBITT) [18, 19]. These techniques rely on systems for which an XUV attosecond light pulse acts as the pump to excite electron dynamics while an IR pulse steers or probes the excitation as the pump-probe delay is varied (Figure 1.5). The attosecond streak camera uses a single/isolated attosecond pulse (SAP) to pump the excitation, and a high intensity ($\sim 10^{13}\mathrm{W/cm}^2$), shorter duration (few-cycle) IR pulse as the probe. The RABBITT technique, on the other hand, uses a train of attosecond pulses (APT) combined with a low intensity ($\sim 10^{11}\mathrm{W/cm}^2$) IR pulse.

1.3.2 Probing Temporal Aspects of Electron Transitions

An early milestone, in terms of applications of attophysics, was achieved when in 2002 Drescher *et. al.* reported temporal measurements of inner-shell relaxation in Krypton [21]. When core electrons are excited in an atomic system, vacancies remain so that ultrafast reorganization relaxes the system towards a lower energy. In this process, the extra energy departs as either an X-ray fluorescence photon or in the form of an ejected Auger electron (Figure 1.6). They used a 97-eV soft

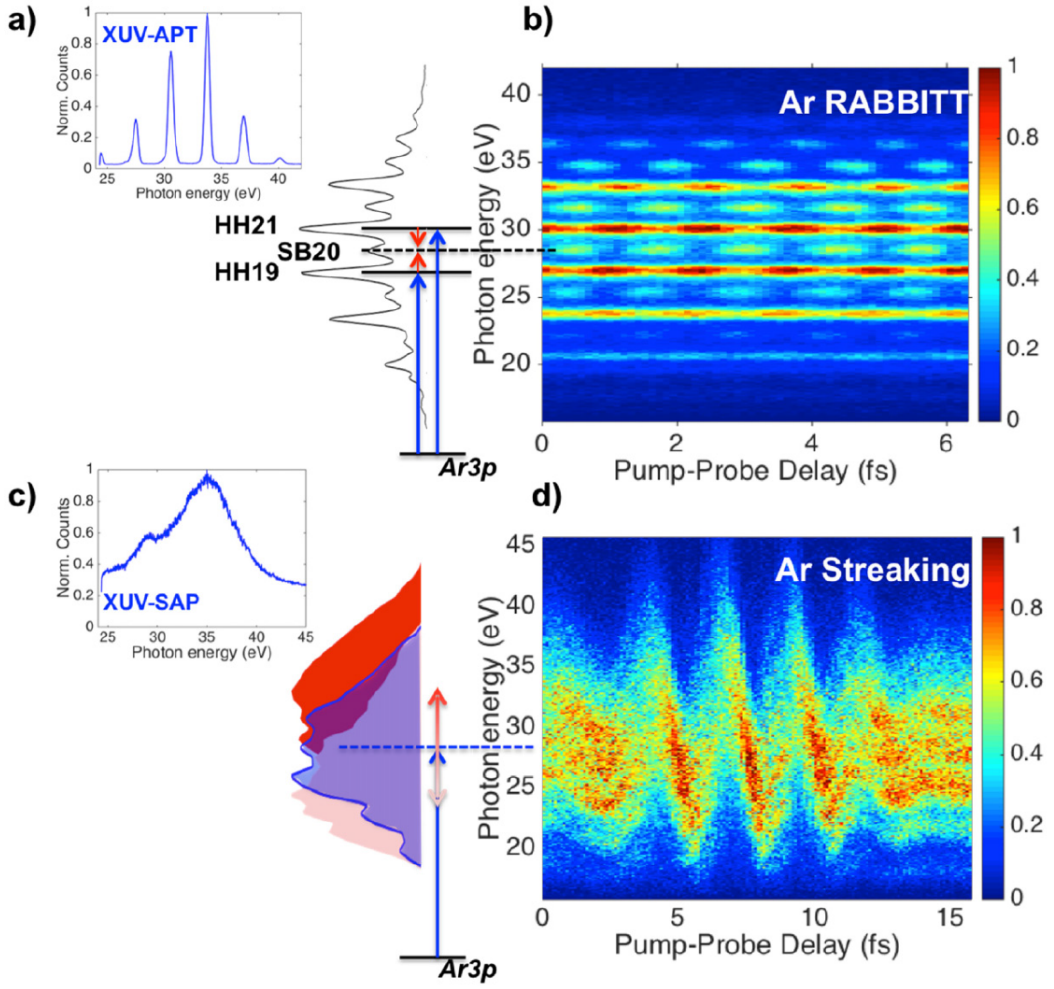

Figure 1.5: A comparison of RABBITT and Attosecond Streak measurements. In RABBITT with a spectrum (a) and spectrogram (b), strong peaks correspond to photoelectrons produced by the odd harmonics of an APT, and weaker sidebands appear in between. An oscillation at twice the fundamental laser frequency is observed. In the attosecond streaking method with spectrum (c) and spectrogram (d), the signal from the SAP dressed by the few cycle IR pulse merges into a single oscillating signal modulating with the shift of momentum of continuum electrons steered by a probe field that is stronger than the typical RABBITT probe. Figure adapted from [20]

X-ray pump pulse and 7-fs, 750-nm probe pulse to trace the M-shell vacancy decay with attosecond resolution. In the study, they found an Auger lifetime of $7.9^{+1.0}_{-0.9} fs$ which checks well with lifetime values derived from Auger spectral linewidths. This experiment is significant because it was the first measurement of a ultrafast phenomena - marking the birth of attosecond physics.

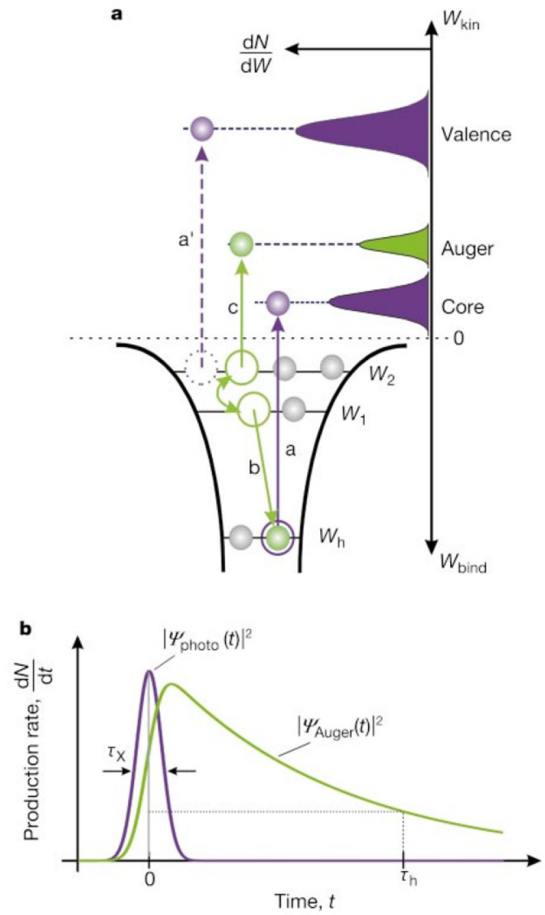

Figure 1.6: The Auger decay process. In (a) an X-ray pulse excites electrons into continuum states, paths a' and a, leaving behind a vacancy (energy W_h). An electron (at W_1) transfers energy to an Auger process, path c, and decays to the hole, path b. In (b) the temporal profiles of the photoelectron and Auger wavepackets are shown. Figure adapted from [21]

An electron tunneling in the presence of an intense near infrared (NIR) laser field is the fundamental starting point of strong field physics. An example of such tunneling is the electronic shakeup that occurs after photoemission, or photoemission followed by Auger decay. In 2007, Uiberacker and coworkers used a high intensity 750-nm, $\tau_L = 5.5$-fs probe pulse and 91-eV, $\tau_X = 250$-as pump pulse to study

NIR probe shakeup and electron tunneling ionization in Neon and Xenon [22]. In the Neon system, the XUV photons did not possess sufficient energy to excite core electrons, meaning the conditions for Auger decay were not satisfied. This type of channel is essentially that which is displayed in Figure 1.7.d. For an Ne^{2+} population, the observed times were measured just under ~ 400 as, serving as a practical upper limit approximation to electron shakeup after XUV excitation. In the Xenon system, Auger relaxations were measured using signals of Xe^{4+} ionic states signal as a function of pump-probe delay. An Auger cascade was recognized with delay separation of 21-fs. This was a meaningful endeavor, because it provided a means to probe transient electronic population dynamics.

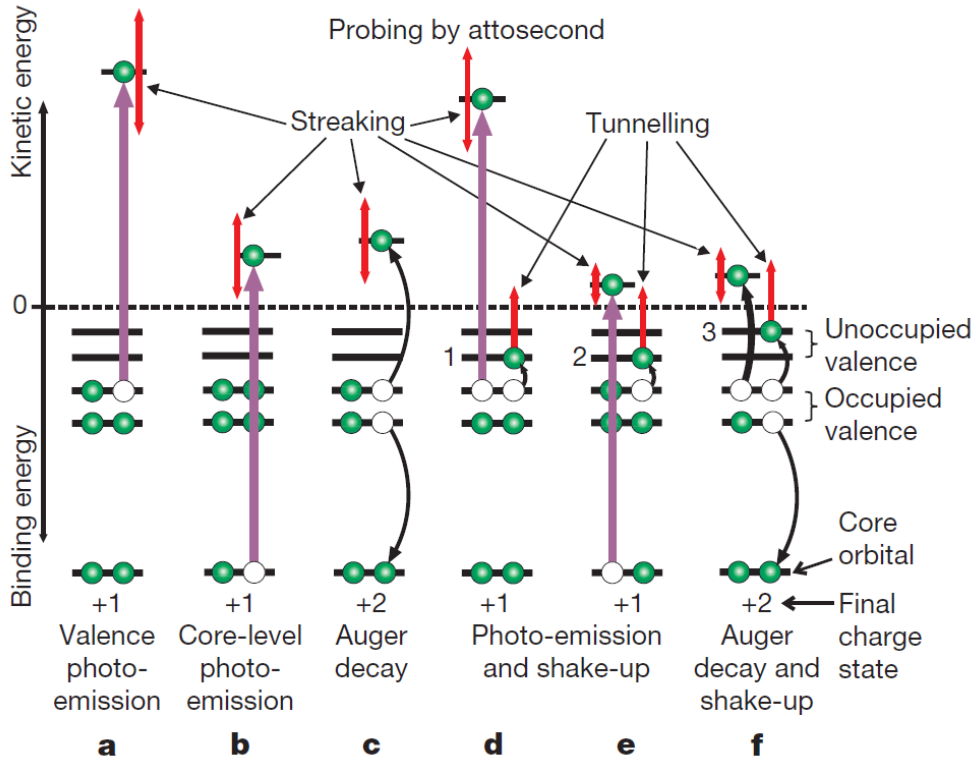

Figure 1.7: In this figure, it can be seen that several processes result in XUV photoionized photoelectron spectra (a-c), while additional channels are possible where NIR-assisted tunnel ionization take place after shakeup with and without Auger processes. Figure adapted from [22]

One of the most fundamental light-matter interactions is photoionization. During this process, a photon with enough energy can free a bound state electron from

its parent atom. While escaping, the electron scatters with the potential, which causes some delay with respect to free-particle motion. The time associated to the scattering is called the Wigner Delay [23]. In 20ll, Klünder and coworkers reported a difference of Wigner delays for the EWPs of the neighboring 3s and 3p shells (Figure 1.8) of Argon [24]. The technique compared the RABBITT sideband signals of the neighboring electron wavepackets which have a form

$$S(\tau) = \alpha + \beta \cos\left[2\omega_L(\tau - \tau_A - \tau_W - \tau_{cc})\right], \tag{1.18}$$

where α and β are constants, τ is the pump-probe delay, τ_A is related to the phase

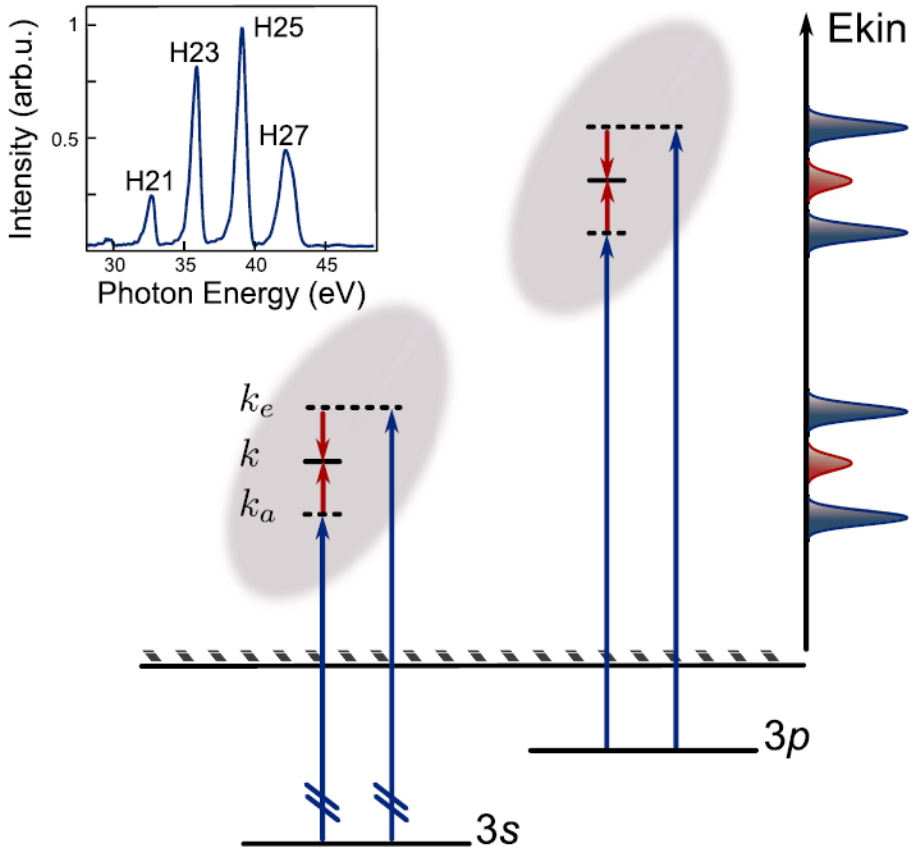

Figure 1.8: Energy diagram for the measurement by Klünder *et. al.* An attosecond pulse train with harmonics (blue arrows) with sufficient energy to ionize the 3s and 3p shells of argon is used. The momenta k_a, and k_e are reached by two neighboring harmonics, and k is reached by additionally absorbing (from k_a), or emitting (from k_e) an IR photon. When the target is dressed by the fundamental, sidebands appear. Figure adapted from [24]

between consecutive XUV harmonics, τ_W is a Wigner-like delay for the single photon ionization, and τ_{cc} is a continuum to continuum delay caused by the absorption or emission of the probe field. It is worth noting that the Wigner delays depend on the EWP kinetic energy and angular momentum transitions. The continuum-continuum delays depend on the EWP kinetic energy and probe field wavelength. The beauty of the experiment comes from the fact that when the phases of the two EWP sidebands, from the 3s and 3p shells are subtracted, all the delay terms cancel except for the Wigner delays. The Wigner delays are large and positive at low photoelectron kinetic energies, but rapidly decrease as they asymptotically flatten at higher kinetic energies. Their results indicated photoionization delays of 140 as at 34 eV and -20 as at 37 and 40 eV. This work was an important step for inspiring more experiments and novel techniques of photoionization delays. More information of the physical concepts involving atomic delays are presented in Chapter 5.

1.3.3 Attosecond Control of Electron Photoemission

Several experiments demonstrating the control of EWP dynamics during photoemission have been reported recently. In these studies, the scattering of electron wavepackets with their parent ionic cores have been imaged. Additionally, the parity interferences of competing two photon quantum paths have been controlled with attosecond accuracy. These experiments serve to inspire exciting applications, and perhaps even more approaches to control electronic structure and EWP behaviors.

An attosecond quantum stroboscope (Figure 1.9) was reported in 2008 by Mauritsson *et. al.* [25]. They used an attosecond pulse train to pump systems, including Argon and Helium, and an intense IR field ($10^{13}\mathrm{W/cm}^2$) was used to steer the photoemission. The APT was generated with two colors, the IR laser fundamental, and UV second harmonic. The IR probe was tailored to be strong enough to drive ionized electrons back to scatter with the parent ion, but weak enough to avoid conditions of tunnel ionization. Mauritsson defined a parameter ,similar to Equation 1.5, as $\tilde{\gamma} = \sqrt{W/2U_p}$ to quantify the regime of the photoemission control. In that equation $W = \Omega - I_P$ where W is the energy

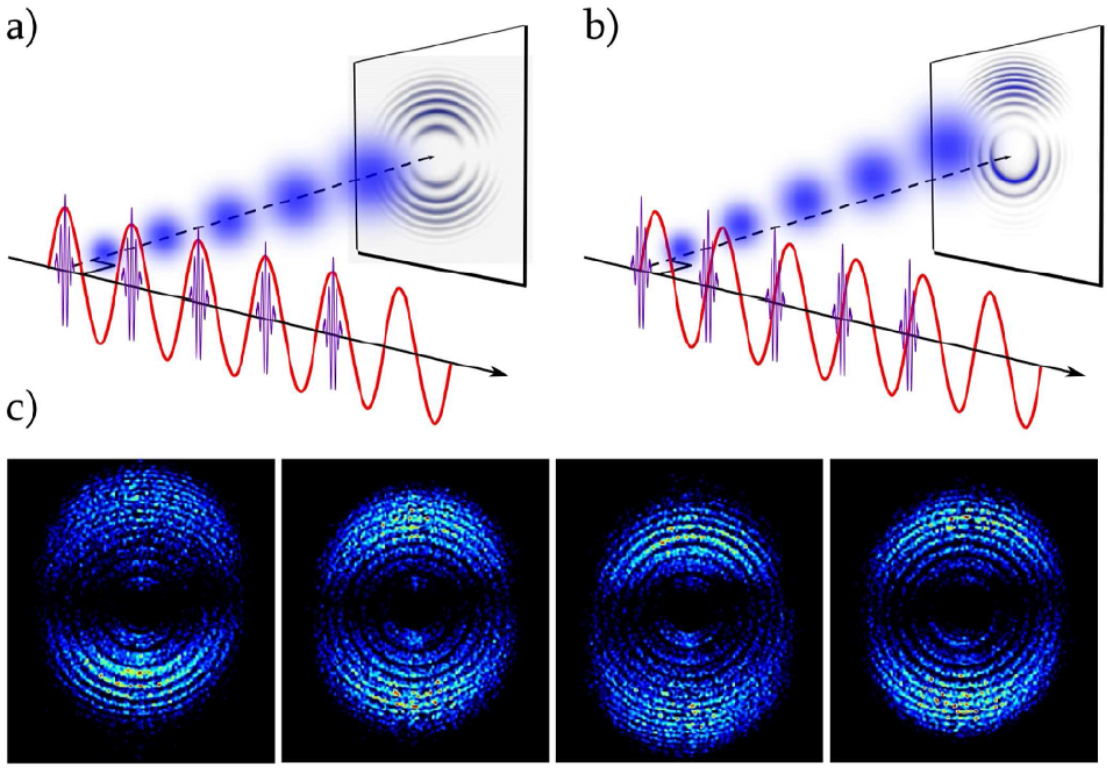

Figure 1.9: Scheme of the momentum transfer in the quantum stroboscope experiment. Photoelectrons are liberated by an APT, and are subject to the momentum transfer that depends on the APT-IR phase. In (a) when the APT meets the max or min of the IR, there is zero net momentum transfer. In (b) at the zero of IR, a large momentum transfer takes place. In (c) experimental images for Argon are shown where the delays are respectively $\tau = 0, T_0/2, T_0, 3T_0/2$. Figure adapted from [25]

for the photoelectric effect with harmonic energy Ω and ionization potential I_P. The momentum transfer is shown in Figure 1.10.

When the intensity of the IR probe is lower (10^{12}W/cm^2), $\tilde{\gamma}$ becomes larger. For larger $\tilde{\gamma}$ momentum transfer can steer the photoemission, but scattering of the electron with the parent ion core does not occur yet. When the intensity is higher (10^{13}W/cm^2), electron-parent ion scattering does take place. Both in TDSE models and experiment, control of Helium was observed for photoelectron dynamics for smaller $\tilde{\gamma}$, this is illustrated in Figure 1.10. The authors envisioned that such techniques lay the groundwork of coherent scattering for high spatial resolution, time-resolved measurements of atoms and molecules. But, these measurements also demonstrated a new area of interest in which the electron photoemission

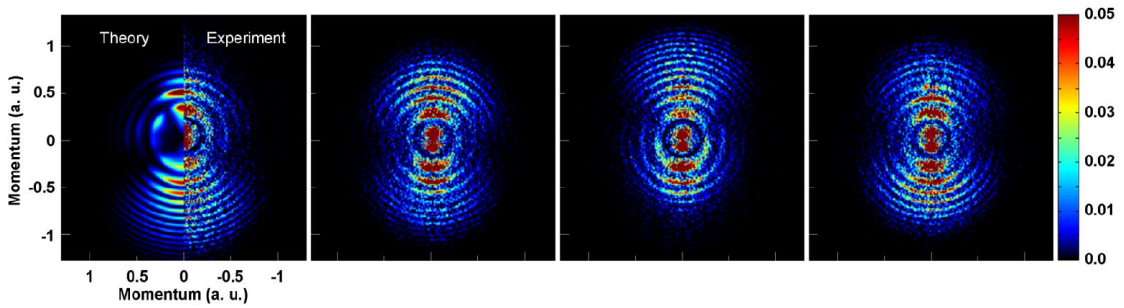

Figure 1.10: A remarkable control of the momentum transfer takes place in the Helium system. With a higher intensity of $1.2 \times 10^{13}\mathrm{W/cm}^2$, there is a larger momentum transfer, and the effects of electron-ion scattering are present. In the far left figure, half the image is overlaid with theoretical results for Helium that match the experiment closely. Figure adapted from [25]

is controlled.

A novel methodology for photoemission control and APT characterization was performed in 2012 by Laurent *et. al.* They exploited the fact that EWP quantum states have an intrinsic odd or even parity related to the angular momentum they possess, which can in turn be used to control the interferences of one and two-photon transitions. During photoionization, the angular momentum of the freed electrons changes by ± 1 for the absorption of a single photon. This causes a change in parity of the electron quantum state. Laurent controlled parity interferences (Figure 1.11) by means of a pump-probe scheme where an APT consisting of even and odd harmonics was used for the photoionization [26]. Unlike the stroboscope control above, which used a strong fundamental field, this study used a weak IR probe field. The method thus more closely resembles the RABBITT technique. The 2D photoemission was detected with a velocity imaging spectrometer to observe a modulation of the upper half and lower half photoemission distribution.

By using an APT consisting of odd and even harmonics, both one-photon channels and two-photon channels have access to the same final EWP energy state. However, one-photon paths have opposite parity to the two-photon paths. Thus, the one photon first order transitions, and two-photon second order transitions interfere due to an odd-even parity mix. It is this parity mix interference that also results in the modulation of the photoemission on the upper half and lower half of the 2D

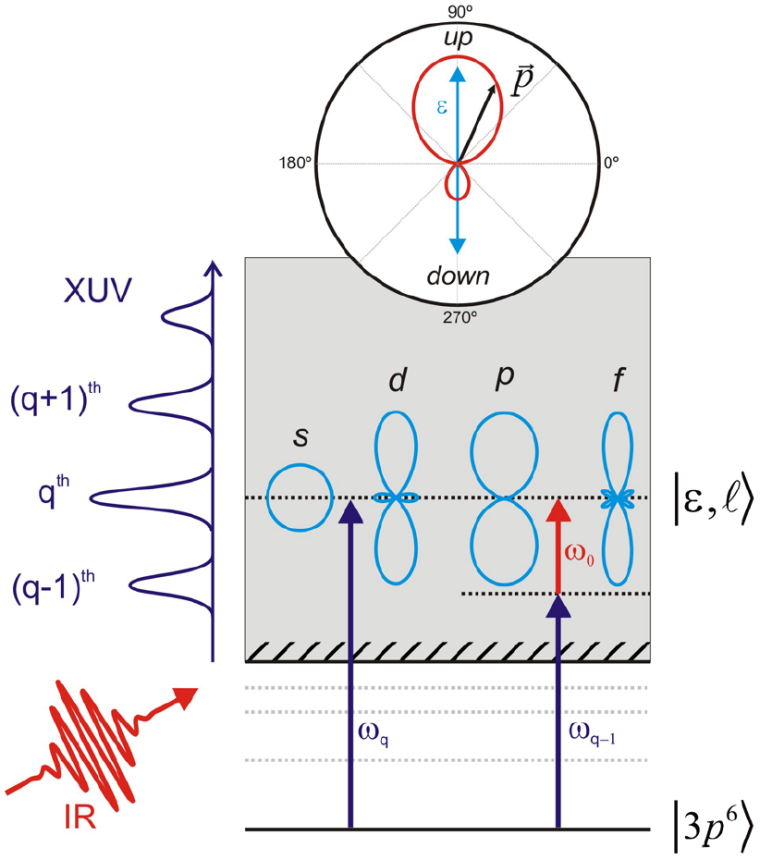

Figure 1.11: Energy diagram outlining the principle of the measurements of Laurent and coworkers. Electrons from the 3p shell of argon are ionized. Single photon ionization populate d and f continuum states, and two photon continuum-continuum transitions result in s and p population. Figure adapted from [26].

spectrum (Figure 1.12). This study showed the process of photoemission can be controlled in this scheme by changing the pump-probe delay. It also experimentally demonstrated that the same scheme can determine the phase between the odd and even harmonics in the APT.

1.4 Looking Forward

In the last twenty years since the confirmation of the first attosecond pulses [7], the techniques for attosecond pulse synthesis and characterization have continued to progress. Theory and experimental techniques have also developed in parallel with the increasing utility of attosecond pump-probe methods, allowing us to study and control exotic quantum phenomena. Steady advancements in the community

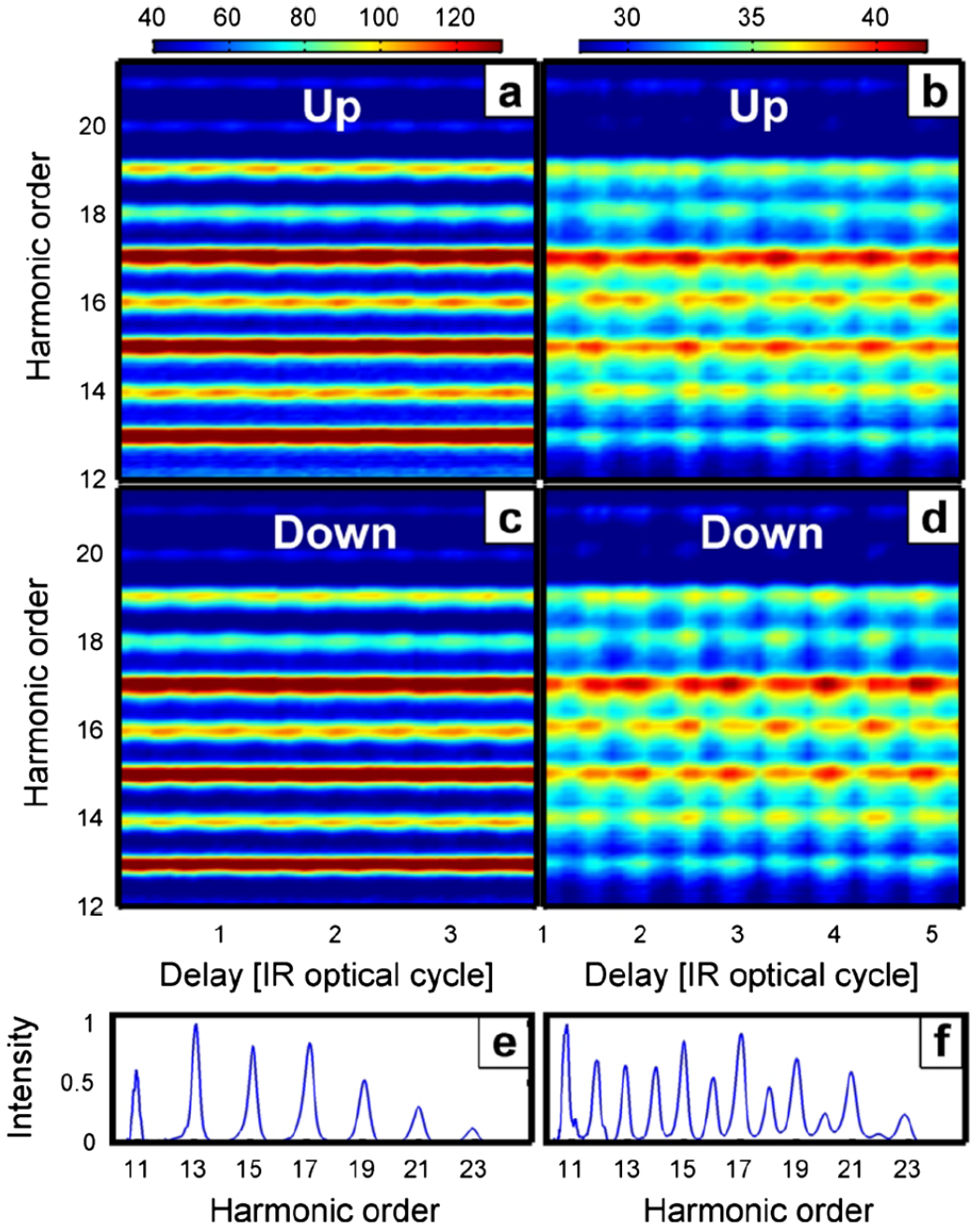

Figure 1.12: A comparison of the up and down photoemission along laser polarization axis halves from photoelectron spectra produced with an APT composed of only odd harmonics (a)(c), versus an APT of odd and even harmonics (b)(d). The photoelectron yields in the up and down Figure adapted from [26].

testify that the applications of attosecond technology are increasingly plentiful. I have no doubt whatsoever that the coming decade will be illuminated by the development of more novel methods for studying ultrafast processes and opportune discoveries of new physical phenomena. Additionally, these forward steps pave the way for pump-probe techniques with zeptosecond pulses - which will bring us closer to witnessing the most vanishing timescales imaginable.

"Have you ever contemplated, Adrian, the phenomenon of springs?' 'Coils you mean?' 'Not coils, Adrian, no. Coils not. Think springs of water. Think wells and spas and sources. Well-springs in the widest and loveliest sense."

— Stephen Fry *The Liar*

2

The Attosecond Source Beamline

Contents

2.1 Statement of Contributions

In this chapter, I present a detailed account about the design and technical development of our experimental setup. First I would like to share a brief story in the first section of how the lab and experimental setup were developed, and my role of assisting in that undertaking by Dr. Laurent. This chapter will also provide explanations about optical instrumentation, attosecond pulse generation

with HHG, and technical specs for our detection system.

By the time I was starting my first semester as a graduate student in Fall 2016, we had erected the walls of the laboratory. After the room was completed, we installed our optical table, shopped for a femtosecond laser, developed the attosecond pump-probe beamline, then finally built and installed the photoelectron detection system. I was only an assistant at that time, but I had the unique privilege to participate in building the experimental setup from start to finish. When I wasn't in class or studying for the general doctoral exams, I was working in lab. It was a once in a lifetime opportunity to gain practical skills and learn about optical systems, lasers, photodetection, and vacuum technology. This period was a foundational part of my technical training, but also taught me the logistics of establishing a new research line. By the end of the construction of the lab and experimental setup, we had stacks of hand-drawn sketches and blueprints. There was not a single step in the process that was made without thorough planning. Over subsequent years, an XUV spectrometer was designed and installed by Spenser Burrows, and an optical system for tuning our HHG was added by Brady Unzicker.

One of my earliest projects involved the design and implementation of a system to measure temperature and humidity in the laboratory. This was an essential task because there is clear correlation between temperature fluctuations and instability of the experimental setup from thermal variations in the air and optical components. The sensors communicated on I2C with an Arduino micro-controller, which I eventually interfaced with LabVIEW. During this project, I learned and adapted expert programming techniques and testing principles with critique and tutelage from Dr. Laurent and Dr. Konopka. Next, I was given responsibilities to write programs for electronics, imaging, and motion control which have since become integrated into our experimental setup and data acquisition.

Our experimental setup has undergone several modifications over the course of three years, but in this chapter I will mainly focus on descriptions for scheme of my most recent experiments (Chapter 5). We opted for an experimental scheme that prioritized tunability over stability. This required us to consider methods to stabilize

and control our interferometer. What began as a standard design based on common stabilization schemes [27, 28] ended up as a project I lead for a novel method to stabilize attosecond measurements (Chapter 3). We achieved an extraordinary level of stability for our delay precision which made the experiment of Chapter 4 and 5 possible. The modifications for the stabilization and later measurements are explained in the respective chapters that follow this one.

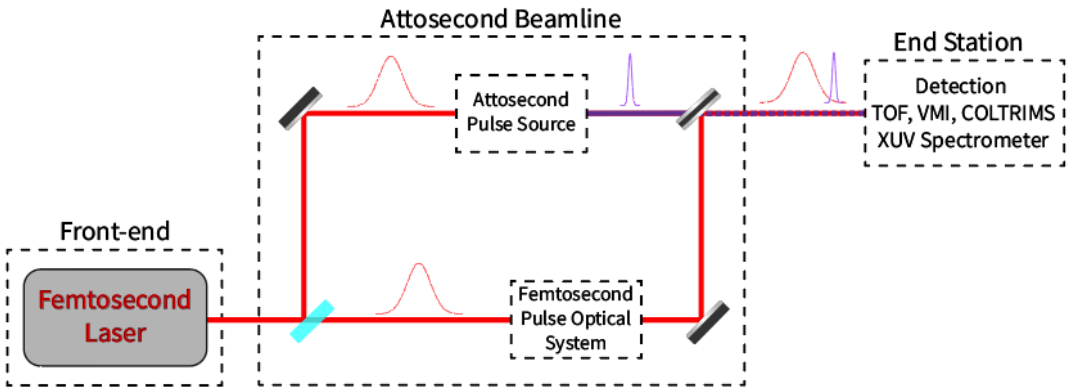

Figure 2.1: The three basic parts of an attosecond pump-probe setup based on the Mach-Zehnder scheme. At the front end, a femtosecond laser. Next is the atto-beamline, which includes a pump-probe interferometer and attosecond pulse source. At the end station is an ion and/or electron detection system such as a TOF spectrometer, VMI, or COLTRIMS.

2.2 Basic Description of Attosecond Measurement Schemes

For attosecond experiments, a typical setup has three main parts (Figure 2.1). At the front end, a femtosecond laser delivers power to the experiment. Next is an attosecond beamline, or "atto-beamline" for short, which includes a pump-probe interferometer containing an attosecond pulse source. At the end station is an ion and/or electron detection system. In this section, we will look at these parts from a general point of view before giving the description of the experimental scheme at ASAP. The two main attosecond measurement geometries are pictured in Figure 2.2. The first is the collinear geometry [29], where both beam propagation

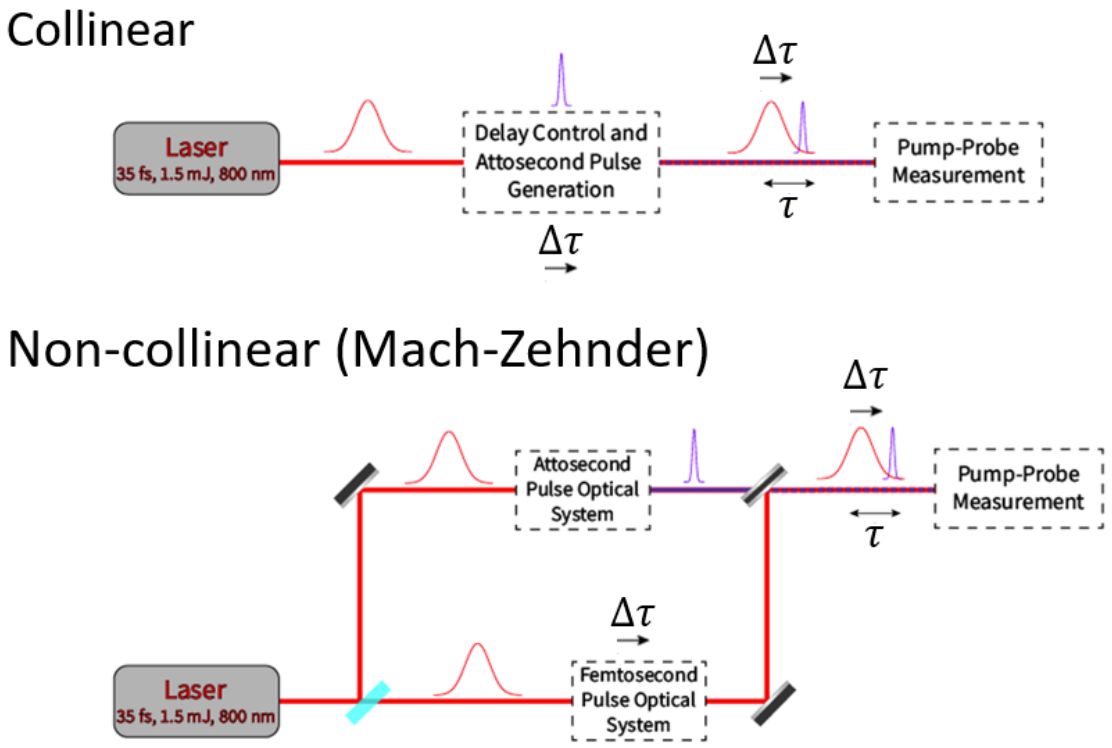

Figure 2.2: The two standard experimental geometries for attosecond pump-probe setups. The upper sketch is a collinear scheme. These typically have high stability, but are not the best suited for tunability and creativity in experiments. The lower sketch is the noncollinear, Mach-Zehnder scheme with less passive stability, but superior tunability.

and optics for both the pump and probe share the same path coaxially. This is possible by using combinations of hole-drilled optics and delay plates. The other configuration with contrasted benefits and drawbacks is based on the Mach-Zehnder layout [27]. With spatially-separated pump and probe beamlines, this noncollinear geometry offers more customization in each arm at the expense of pump-probe stability. Thermal and mechanical vibrations disturb the independent beamline optics causing a jitter in the pump-probe delay. In the Mach-Zehnder configuration, once the light is divided by a beamsplitter, the paths are spatially-separated until they reach the recombination point. We might consider a Michelson interferometer whose beamline arms are also spatially-separated. Unfortunately the arms of the Michelson encounter reflectance at normal incidence before recombination. The reflectance of even highly reflective materials quickly drops for shorter wavelengths at normal incidence angles which would absorb the HHG.

Front-end ultrashort laser systems are used to deliver power for both the HHG production and the probe beamline. Generating attosecond pulses requires a high intensity ($\sim 10^{14}\mathrm{W/cm}^2$). An ongoing pursuit of lasers with increasingly higher peak powers has been a primary objective since the invention of the first laser in 1960 [30]. Two methods for generating ultrashort laser pulses, Q-switching [31] and mode-locking [32], deliver high peak powers P_{peak} thanks to their combination of high pulse energy E_{pulse} (μJ to mJ per pulse) relative to pulse duration τ_{pulse} ($10 - 100$ fs) seen with the relationship

$$P_{peak} = \tilde{c}\frac{E_{pulse}}{\tau_{pulse}}, \tag{2.1}$$

where $\tilde{c}$ is characteristic factor for the pulse.[1] Currently, some of the shortest duration pulses come from Ti:Sapphire laser systems. The Chirped Pulse Amplification (CPA) technique supplies today's Ti:Sapphire lasers with enough power to drive HHG [10].

In the attosecond beamline, a pump-probe configuration must be implemented where a first pulse excites the system under study and a second pulse probes the excitation. This is achieved by sending the femtosecond pulses into an interferometer. A portion of the power is used to generate XUV attosecond pulses in the pump beamline, while the other portion is sent in the second arm of the interferometer as the probe where it is used or tailored to the need of the experiment (i.e. converted to its second harmonic, or wavelength fine-tuned). A number of setup geometries have been implemented with various performance tradeoffs. Usually improved tunability results in worsened stability, and *vice versa*. If a high level of tunability is required, then stabilization schemes must be designed in order to maintain a good temporal resolution in the measurement.

Finally, at the end station, a multi-particle detection system is used to image the pump-probe dynamics. These types of detection systems have been in development since the early 20th century and include time of flight (TOF) spectrometers [33], magnetic bottle spectrometers [34], COLd Target Recoil-Ion Momentum

[1] The unitless factor $\tilde{c}$ represents the envelope of the pulse, and it is equal to 0.94 for a Gaussian envelope.

Apparatus	Particles	Angular Distr.	Count Rate	Coincident Det.
TOF	ions/e^-	No	High	No
VMI	ions/e^-	Yes	High	No
COLTRIMS	ions/e^-	Yes	Low	Yes
XUV Spectr.	photons	No	High	No

Table 2.1: Characteristics of the most widely used instruments in particle detection in atomic, molecular and optical physics: TOF spectrometers, COLTRIMS apparatus, XUV spectrometers, and VMI spectrometers.

Spectroscopy (COLTRIMS) [35, 36], XUV spectrometers, and velocity map imaging (VMI) [37]. Some attributes of these systems are shown in Table 2.1. These detection schemes are described with more detail in Section 2.5, but in the beamline for my experiments, VMI is the detection scheme I used due to its appropriate attributes (4π solid angle collection, angular distribution of momentum, and high count rate).

2.3 Front-end Femtosecond Laser System

One of the first major decisions we had to make was to select our femtosecond laser (Coherent, Legend Elite Duo). One of the primary uses for the laser is supplying the power to the attosecond pulses source. Generating attosecond pulses requires high intensity $\sim 10^{14}\text{W/cm}^2$. We selected a Ti:sapphire system because it is an all-around best choice. As far as gain media go, Ti:sapphire is very robust, having a very high thermal conductivity comparable to metals. As a comparison, a laser system based on organic dye [38], has a gain medium that not only has to switched out every hundred or so hours of operation, but it is also toxic. Ti:sapphire systems also deliver pulses with some of the highest peak powers available. The laser delivers linearly polarized ultrashort laser pulses at a repitition rate of 10kHz. Each pulse has duration of 35 fs, energy of 1.5 mJ, and a central wavelength of 800 nm. The average power can be adjusted to as high as 15 W, which is enough to be divided as 60/40 or 80/20 with beamsplitters to generate harmonics and supply the probe beamline respectively. We can use the time-bandwidth product to estimate the frequency bandwidth $\Delta\nu$, or the laser pulse duration for the transform

limited pulse with $\Delta\nu \cdot \tau = k$.[2]We split the output of the laser between two arms of a Mach-Zehnder interferometer. In one arm, the power is used to drive the HHG for our APT. In the other arm, the remaining power is used as the probe in attosecond pump-probe experiments. The Ti:sapphire laser consists of several components which are shown in Figure 2.3.

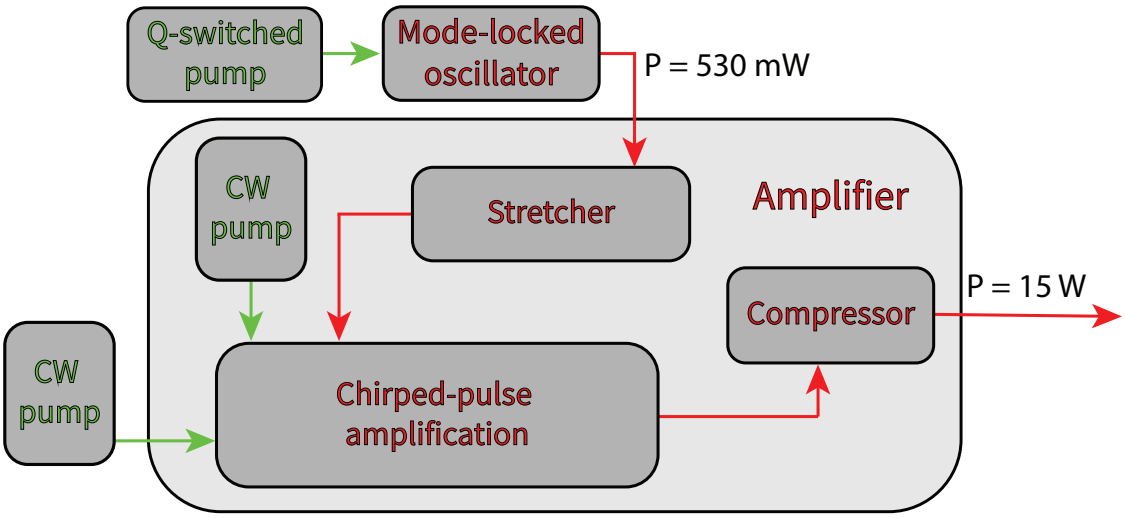

Figure 2.3: Layout of the femtosecond laser system. A 532-nm Q-switched pump laser seeds a mode-locked oscillator. Self-phase modulation broadens the gain of the oscillator, and Kerr lensing drives the amplification. A train of pulses centered at 800 nm at an average power of 530 mW is delivered to a stretcher which elongates the pulse in time. Chirped-pulse amplification is pumped by two 532-nm CW pump lasers, and increases the laser intensity. A compressor, at the end, shortens the pulse in time to 35 fs of duration with an average power of 15 W at a repetition rate of 10 kHz.

2.3.1 Mode-locked Oscillator

For nearly fifty years, starting in 1964 [32], mode-locked lasers (Figure 2.4) have demonstrated some of the shortest pulse durations available. Different varieties of mode-locking exist, but the most ubiquitous form used is Kerr-lens modelocking [39]. Because of the nature of the doping in Ti:sapphire, radiative transitions involve vibronic crystal-field configuration transitions. This gives rise to a very broad absorption range of 400 nm to 630 nm and emissions from 660 nm to 1180 nm [40]. Our oscillator is pumped by a 532-nm Q-switched diode laser (Verdi G, Coherent). The "modes" of mode-locking come from the fact that a laser cavity with a length

[2]k = 0.441 for a Gaussian pulse model

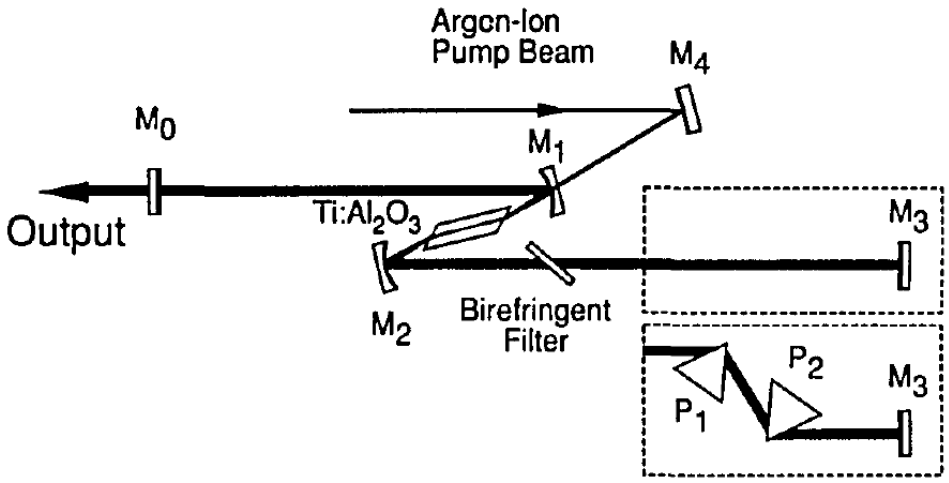

Figure 2.4: The classic schematic of a Ti:sapphire Kerr lens mode-locked laser. The pump laser enters at a dichroic mirror M1. The resonator cavity is defined by the output coupler M0 and mirror M3. The gain material is in between M1 and M2, and the prism pair P1 and P2 compensate for dispersive effects on the spectral composition of the ultrashort pulse. Figure adapted from [39].

L can support a large number of modes N which are of course spaced in frequency by $\Delta\omega = 2\pi/T_c$ where T_c is the cavity round-trip time. When the phases of the modes φ_i are fixed, once every cavity cycle period the modes constructively form a pulse of duration $\Delta\tau = T_c/N$. This light becomes intense at these points, so the Kerr effect starts. This means the index of refraction is now dependent on the light intensity as $n(t) = n_0 + I(t)n_{NL}$ where n_0 is the linear index of refraction, and n_{NL} is the nonlinear index. Most of the intensity is located toward the spatial middle of the beam, so the Kerr effect is more pronounced there. A converging lens works the way it does because the optical path increases for light in the middle of a collimated beam, and the same effect happens here. Because of a larger index near the middle from the Kerr effect, the optical path is larger resulting in the action of Kerr-lensing which drives amplification. In addition to Kerr lensing, the effect of self-phase modulation causes the instantaneous carrier frequency to change. Since the carrier phase is $\omega_0 t - kz$ where $k = \omega_0 n(t)/c$ and the instantaneous carrier frequency is the time derivative of the phase, it has a variation in time as

$$\delta\omega(t) = \frac{-\omega_0 n_{NL}}{2c}\frac{\partial}{\partial t}I(t) \tag{2.2}$$

where ω_0 is the pulse central frequency. This causes a spectral broadenening of the pulse since these extra frequencies are supported with the gain material. Blue shifts are added to the trailing end of the pulse, and redshifts are added to the front, resulting in positive chirp. These extra modes are supported in the cavity with a pair of dispersive optics such as prisms that compensate against the chirp. Because of the Kerr-lensing, high intensity is automatically selected. Our femtosecond laser system uses a passively mode-locked Ti:Sapphire laser called the oscillator (Vitara S, Coherent). It has a wavelength bandwidth of $\geq$70 nm oscillating in the cavity at 80 MHz. It delivers linearly polarized light with an average power of about 530 mW to the Amplifier (discussed in next section).

2.3.2 Amplifier

When attempting to amplify an ultrashort laser pulse, the already high peak power can induce a nonlinear response of the gain medium which can destroy the material. The source of the problems stems from Kerr lensing. This can easily be the case for ultrashort pulses. The damage threshold of the Ti:Sapphire gain crystal is at a fluence (units J/m^2) of 10 J/cm^2 [41]. We can calculate the fluence with

$$F = \frac{E_{pulse}}{\pi(w/2)^2}, \tag{2.3}$$

where w is the waist of the laser beam when the intensity drops to $1/e$. The fluence of our laser, with $w = 11$ mm, and $E_{pulse} = 1.5$ mJ is about 15.8 J/cm^2 at maximum compression.[3]. The resolution for this dilemma came from CPA. The technique for CPA was jointly pioneered by Gerard Mourou and Donna Strickland who later shared the 2018 Nobel Prize for their discovery [42]. The scheme is as follows: the pulse is first stretched in time, having its duration increased by a large factor of around 10^3 or 10^4 so that its peak power is drastically reduced, then the pulse makes multiple passes in a regenerative amplifier [43] scheme obtaining an amplification by a factor by nearly 30, finally the pulse is recompressed to its original duration. This compression is user controlled so that the output average

[3]We believe that the pulse energy depends on the compression of the beam average power. At maximum compression we have $P_{avg} = 15$ W and $E_{pulse} = 1.5$ mJ.

Material (2 mm)	Wavelength (nm)	GVD(fs^2/mm)	τ_i(fs)	τ_f(fs)
Fused Silica	400	97.57	35	35.84
	800	36.16	35	35.12
	800	36.16	8	14.87
BK7	400	122.04	35	36.31
	800	44.65	35	35.18
	800	44.65	8	17.42
Calcite o-ray	400	111.912	35	36.11
	800	42.01	35	35.16
	800	42.01	8	16.61
Calcite e-ray	400	115.86	35	36.18
	800	43.34	35	35.17
	800	43.34	8	17.02

Table 2.2: Some material properties and their dispersion effects on ultrashort pulses for commonly used optical materials. The thickness is chosen to be 2 mm. The manner in which the group velocity dispersion (GVD) broadens pulse durations of inital duration τ_i to final duration τ_f is seen to have harsher effects on pulses with either shorter durations, or those with central wavelengths that are shorter. Pulses with shorter durations have larger bandwidths, and in general chromatic dispersion is known to be stronger for short wavelengths.

power can be adjusted. After leaving the amplifier, the IR pulse train is directed to a Mach-Zehnder interferometer of the pump-probe beamline.

2.4 Attosecond Pump-Probe Beamlines

Over the last three decades, a number of successful schemes for attosecond pump-probe setups have been conceived, each with its own unique advantages and disadvantages. In standard attosecond pump-probe measurements, an attosecond pump pulse excites a target and a femtosecond probe pulse with an adjustable delay probes the excitation. These measurements are carried out with interferometers where one arm functions as the XUV attosecond beamline, and the other as the IR or UV femtosecond beamline with variable delay. There are many considerations to make when developing pump-probe beamlines because beam power and tabletop space are limited resources. The pulse duration is also sensitive to propagation through media because of the inherent group velocity dispersion in materials. The dispersion effects of commonly optical substrates with 2 mm thickness on ultrashort

pulses is provided in Table 2.1. Often times prioritizing one characteristic of the experimental setup supports improvement in the others. For instance, we use as few optical elements as possible in the setup which reduces the power losses at reflections as well as dispersion from transmissions, while also taking up less space. We opted to build an experimental setup that achieved these goals to a high degree, while satisfying the need for tunability of harmonics in the attosecond pulses, and the possibility to probe with a pulse with central frequency ν_c of the fundamental IR laser field or its UV second harmonic. The one trait that any attosecond beamline must have is to generate and propagate the attosecond pulses under high vacuum, and to refrain from sending them through any materials whatsoever except the target at the end. Based on the effects dispersion has on short wavelength, large bandwidth pulses as seen in Table 2.1, the effects would be detrimental.

2.4.1 Mach-Zehnder Interferometer for Pump-Probe Measurements

As stated at the end of the previous section, our pump-probe scheme is in the Mach-Zehnder configuration. The interferometer can be supplied with the unaltered train of 35-fs linearly polarized IR pulses which I have used in my experiments. Alternatively, with the flip of a mirror, the pulses can be sent to a hollow fiber compressor filled with noble gas to have the pulse durations shortened to as little as 8-fs at energies of 600 μJ per pulse. Such few cycle pulses have been applied for the use of generating single attosecond pulses (SAP) [44, 45]. After leaving the Ti:Sapphire amplifier, the train of femtosecond pulses is propagated in air, but enclosed inside walls to minimize effects of air drafts in the room. The beam is directed by a sequence of optics in the enclosed path toward a beamsplitter that is the starting point of the Mach-Zehnder interferometer. The reflected part of the beam makes up the attosecond pulse beamline, and the femtosecond probe beamline is comprised of the transmitted portion. Since a substantial amount of power is needed for generating a harmonic spectrum via HHG, but a much lower intensity is used for the probe, an 80/20 or 60/40 beamsplitter is used to reflect/transmit the

power appropriately. Except for a handful of optics immediately after BS, most of the interferometer optics are housed in chambers under ultra-high vacuum conditions. This reduces the amount of dispersion and absorption of the attosecond pulse by air. The chambers were originally secured to the table so that the tapped-hole layout of the optical breadboard inside would be aligned with the table breadboard outside. Irises were also placed before and after the vacuum chamber entrance viewports so that optics could be placed correctly. These irises define the alignment of the interferometer as master reference points, and are under no circumstances moved.

A schematic view of the latest experimental setup, for Chapter 5, is shown in Figure 2.5. The transmitted probe pulse train can enter straightaway, or be frequency doubled in the optical system (OS). In the event a pump-probe scheme requires a second harmonic pulse, a beta barium borate crystal (β -BBO) [46] and ancillary optics fastened on a moveable stage create the conditions for Type I second harmonic generation (SHG). A β -BBO crystal has a birefringence where, for the ordinary and extraordinary refraction indices, $n_o(\omega) > n_e(\omega)$. When used in a Type I disposition, two photons having frequency ω_0 at polarization with respect to the ordinary axis create a $2\omega_0$ photon with polarization with respect to the extraordinary axis. The intensity of the second harmonic is

$$I(2\omega_0) \propto \omega_0^2 I^2(\omega_0) L^2 \mathrm{sinc}^2\left(\frac{\Delta k L}{2}\right) \tag{2.4}$$

which shows the expected second order proportional dependence on the squared intensity of the IR field $I(\omega_0)$, the length of the crystal L squared, and an additional wave phase term Δk in the sinc function [47]. For perfect phase matching, $\Delta k = k_{2\omega_0} - 2k_{\omega_0} = 0$. Equivalently, $n_{2\omega_0} = n_{\omega_0}$ to produce coherent light, so the crystal axis c must be rotated such that $n_e(2\omega_0, \theta) = n_o(\omega_0)$. This critical phase matching condition ensures that the phase velocity of both the IR pulse and second harmonic UV pulse have the same phase velocity. The importance for this is that, further along through the crystal, UV photons are produced in phase with the earlier ones. It has been found experimentally that the angle θ_m for 800 nm should be about 30° [48]. Two dichroic mirrors are also fastened on the stage with the BBO. The first

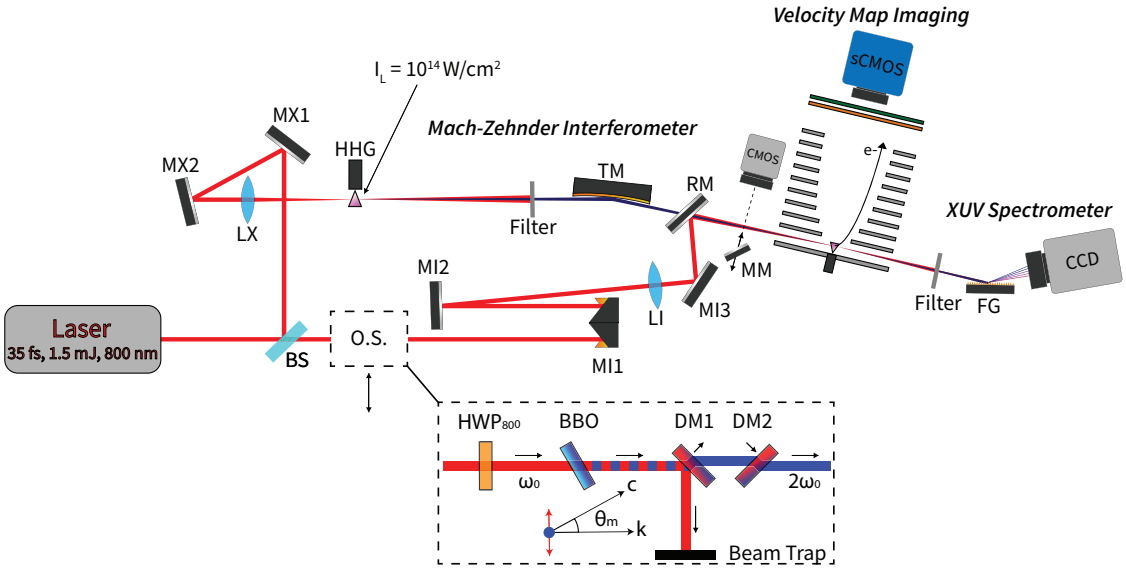

Figure 2.5: The organization of the attosecond beamline.. An IR femtosecond laser is at the beginning supplying the power to be used for the pump-probe beamlines. The Mach-Zehnder interferometer begins at the beamsplitter BS and ends at the recombination mirror RM. The lower path that includes the retroreflector MI1 mounted on a micrometer stage, as well as a piezo-mounted mirror MI2 to control delay, is the IR probe beamline. An inset shows an optical system O.S. holding a BBO with crystal axis c tilted from the propagation direction k to the phase-matching angle. This system upconverts the IR pulse to UV and has two dichroic mirrors, DM1 which filters the remaining IR, and DM2 that compensates for walkoff. The upper path is the XUV pump beamline where HHG is used to generate harmonics for the attosecond pulse. Beyond the interferometer, a VMI and XUV spectrometer are used for experiments such as photoelectron spectroscopy or transient absorption experiments respectively.

dichroic mirror, whose face is rotated at +45° to the angle of incidence removes any residual fundamental light. The other dichroic mirror rotated at -45 to the angle of incidence is used to compensate for the walk-off of the first. To minimize dispersion effects at the entrance of the vacuum chamber, a 1-mm thick UV-fused silica flange window was chosen for its lower group delay dispersion to replace the stock viewport. Once inside the chamber, the path begins with mirror MI1, and ends with the recombination mirror RM. The retroreflector mirror MI1 is mounted on a vacuum compatible micrometer translation stage (MFA-CCV6, Newport) which allows the user course adjustment when searching for temporal overlap for the pulses. Next, another mirror mounted on a piezoelectric stage allows for the steps in delay on the attosecond time scale. Prior to recombining with the attosecond beamline at

the recombination mirror RM, the IR probe passes through a 75 mm converging lens that focuses the beam into the interaction region of the VMI.

The reflected part of the beam is used for HHG. After reflection the beam travels to, and reflects off of two mirrors MX1 and MX2 whose configurations are freely adjusted to make the lengths of the pump and probe beamline paths approximately equal. Next the femtosecond pulse train is steered through a 30-cm convex lens LX which focuses the beam into a small vacuum chamber where the harmonics are generated. This chamber entry viewport is also a 1-mm thick UV-fused silica window chosen to reduce GVD at this point as well. After HHG, the attosecond pulse beam is guided to a 375-mm focal length gold coated toroidal mirror TM at a 4° grazing incidence working in a $2f$-$2f$ focal geometry. This means that, using the thin lens equation

$$\frac{1}{d_o} + \frac{1}{d_i} = \frac{1}{f} \tag{2.5}$$

where d_o is the object distance (located in the HHG chamber), d_i is the image distance (which ends up being at the interaction region), and f is the focal length. For $d_o = 2f$ the image will be located accordingly $d_i = 2f$. This focusing APT reflects off the TM, then goes through the hole drilled RM, and finally into the interaction region of the VMI chamber.

2.4.2 Attosecond Pulses Source: HHG

We generate an attosecond pulse train via high harmonic generation of a rare gas [10]. We use Argon and Neon, although other gases may be used as well as long as they posses inversion symmetry i.e. Xenon, Krypton, or Helium [49]. Equation 2.2 can be rewritten as

$$\Omega_{max} = I_p + 3.17U_p \tag{2.6}$$

where Ω_{max} is the energy of the highest harmonic order measured, and U_p is the ponderomotive energy, which as seen in Chapter 1 depends only on the intensity of the driving laser field E_L and laser frequency ω_L. Based on empirical observations

Gas	Ionization Energy (eV)	Cutoff Energy (eV)	Odd Harmonic Order
Helium	24.59	41.37	25
Neon	21.56	38.34	23
Argon	15.76	32.54	21
Krypton	14.00	30.78	19
Xenon	12.13	28.91	17

Table 2.3: The first five rare gases and their expected odd order harmonic cutoffs for a driving laser centered at 800 nm and a ponderomotive energy of 5.29 eV. This value was obtained by an estimation involving the empirically observed drop we regularly see in the harmonic plateau of the Argon spectrum located at the 21^{st} harmonic. Note that the energy of the fundamental IR photon is about 1.55 eV.

that our harmonic spectrum in Argon begins to drop sharply at the 21^{st} harmonic, we can roughly estimate that the ponderomotive energy is about 5.29 eV. In Table 2.3, some rare gases and their expected odd harmonic order cutoff based on this value for U_p are shown. The gas is delivered with a network of lines coming from gas tanks (Airgas) secured outside the lab. An ergonomic design allows the changing out of gases simply by opening the valve of the desired species. Of utmost importance is the purity of gas line as cross contamination affects the quality of the spectrum. A small vacuum pump is connected with the gas line network to purge the system, while all valves are closed, before selecting the desired gas. The HHG chamber architecture begins with the gas line from the network being connected to and having its flow rate controlled by a compact gauge by Pfeiffer Vacuum. A 2-mm diameter cylindrical glass needle is mounted at the tip. This is in turn fastened to a micrometer X-Y axis manipulator (DTS-275-155, Huntington Mechanical Labs) that sits on the top of the HHG chamber with the gas needle going through the center. When the gas is opened up, a backing pressure of tens to hundreds of mbar is allowed in by the gauge. Because the glass needle is drilled by the laser, gas escapes into the chamber. Besides this chamber having its pressure maintained by its own turbomolecular pump (Hi Pace 700, Pfeifer Vacuum) a hole-drilled copper blank that also acts as a differential gasket for the ConFlat flanges between the HHG chamber and chamber housing the TM and other optics. A valve is also in place to isolate the HHG chamber from the TM chamber when no experiments are running.

Our experiments have involved measurements that use probe pulses with odd harmonics as well as even and odd harmonics of the fundamental laser frequency, so the path between the focusing lens and HHG chamber was given enough space to construct an optical system to generate these different sets of harmonics. Brady Unzicker and Dr. Laurent designed and implemented this optical system which uses a BBO to generate the second harmonic, a half-wave plate to orient the polarization with the residual driving field, and motorized assembly of wedges to control the phase between the 400-nm second harmonic and the fundamental IR field. More information can be obtained on the functionality of this optical system and its application in their recent work [50]. Harmonic spectra display a common trait, the first few harmonics dominate the spectrum but steadily decrease in amplitude. Then a large span of the harmonics referred to as the "plateau" consists of peaks of comparable amplitudes persists for a relatively longer before abruptly falling [11, 49]. For further interest, studies have been done to observe the conversion efficiency dependence on gas species, intensity, and backing pressure [49, 51]. After generating harmonics, the spectrum is trimmed with an aluminum filter, mounted on a rotary feed through handle (VF-106, Huntington Mechanical Labs), that staunchly attenuates harmonics with energy below 17 eV (11^{th} harmonic of 800 nm). The transmission curve for a 200-nm thick Al filter (Lebow) is pictured in Figure 2.6.a and demonstrates the effects on photons with energies from 10 eV to 65 eV. Also shown is the Group Delay (GD) effects which were calculated by first obtaining the refractive index n [52] and using the relation of $t = nd/c$ where d is the filter thickness, then using an equation

$$\Delta t = \frac{d}{c}(n-1) \tag{2.7}$$

we can calculate the delay with respect to vacuum. We can use the spectra of the XUV-spectrometer, and the images of our velocity map imaging system, to measure the strength and quality of our harmonic spectrum in a complementary way. The XUV spectrometer consists of a flat field grating and CCD camera (Newton, Andor). The spectrometer has a better quantum efficiency in the soft x-ray range

(30 eV to 1000 eV), while the velocity map imaging system is best suited to detect photoelectrons created by photons up to about 39 eV. I would like to note after an exchange with Spenser Burrows that he tells me the QE graph shown in Figure 2.6.b came from a datasheet for the Andor Newton SO camera and it represents the absolute quantum efficiency (QE). The full curve is described as quantum efficiency of the sensor at 20C, as supplied by the sensor manufacturer. The relative QE refers to measuring one camera's QE against another reference camera - a standard practice for spaceflight instruments where the flight camera to a reference one on the ground.

2.5 Detection System: Velocity Map Imaging

In our lab, we have used the Velocity Map Imaging (VMI) [37] technique to characterize electron dynamics of atomic gases. Using VMI, see Figures 2.7 and 2.8, electrons ejected from the target are guided by an electrostatic field along a time of flight axis. The electric field is formed by a series of circular metal ring electrodes, supplied with voltages to create a gradient. At the end of the time of flight axis, they collide on a detector consisting of a microchannel plate, phosphor screen, and camera system. Noteworthy is the fact that photoelectrons with the same velocity vector are mapped to the same point on the 2D detector surface. Although we are capturing 2D images, the symmetry of the experiment allows us to use inversion procedures that can reconstruct the 3D velocity distribution [53–56]. We use a later generation system called the Thick-Lens VMI (TL-VMI) [57], but there are only a few differences between it and the original model, namely that it has eleven electrodes while the original has three.

VMI has been used since 1997 [37] to study the 3D momentum distributions of charged particle dynamics of atoms, molecules, and nanostructures [26, 58–60]. It is one of the more recently added members to the family of instruments used for ion/electron detection applications which include: traditional time of flight (TOF) spectrometers, magnetic bottle TOF spectrometers, and the cold target recoil ion momentum spectroscopy (COLTRIMS) apparatus [33, 34, 61]. Choosing

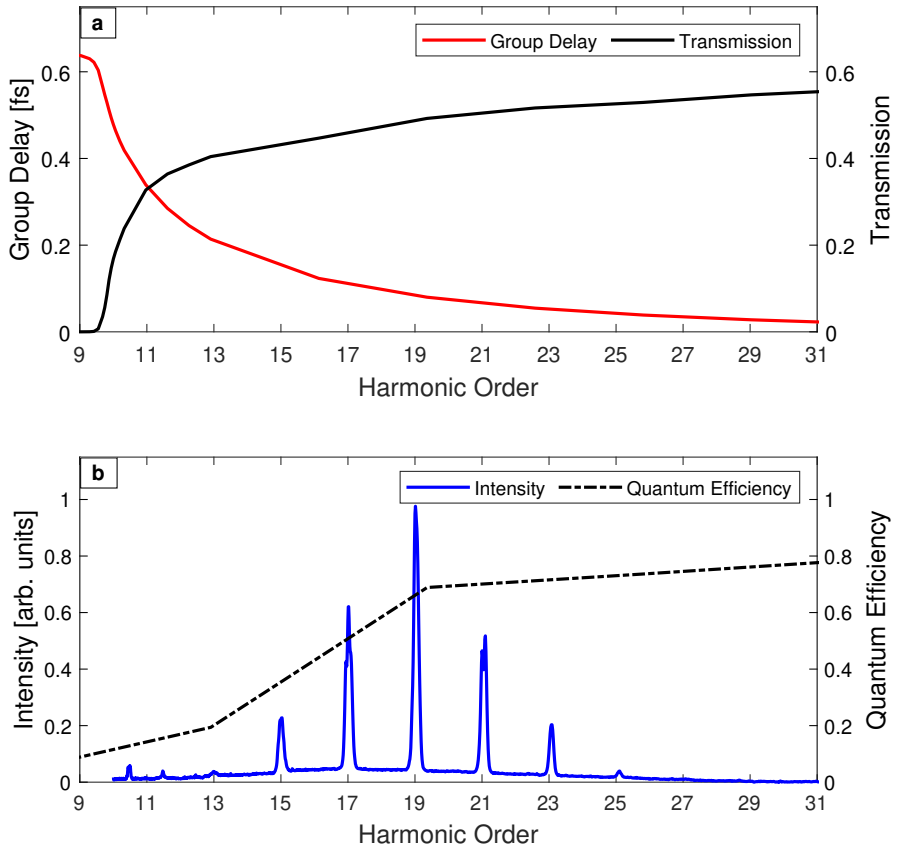

Figure 2.6: Detection of XUV harmonics from HHG. In (a) the transmission curve of aluminum as well as the group delay is pictured to show the effects of the aluminum filter on the XUV harmonics. In (b) a spectrum captured by the XUV spectrometer along with its quantum efficiency is provided. Although the harmonics that pass through the filter include H11 to H25, the quantum efficiency of the spectrometer camera is best for short wavelengths (higher energy) which prevents it from capturing H11 to H17 with better fidelity. The transmission and index of refraction data used for the GD is based off the work of [52], and the quantum efficiency was provided by Andor.

the right detection technique requires a basic understanding in the utility of each i.e. the dynamics it can resolve/focus.

In TOF spectrometers, ions or electrons are ejected from an interaction volume and guided by an electric or magnetic field for a short distance. Then the charged particles drift down a field free region of length L for the rest of the flight. With their time of flight t measured, their initial kinetic energies can be known since $t = L/v$. For this technique, particles of a given mass are said to be "focused in

energy" because particles arriving at t were ejected with the same energy.

While TOF techniques measure the arrival times to determine kinetic energy, VMI and COLTRIMS have a 4π collection angle and to measure electron and ion momentum distributions. In VMI, Figure 2.7, an electron or ion with an initial momentum from the interaction is mapped to a distinctive point on the detector. Similarly, COLTRIMS obtains a complete picture for electrons and ions coincidently by also measuring the time of flight. For these techniques, the events are said to be "focused in momentum" because charged particles with the same momenta are mapped to the same detector positions. A practical difference between VMI and COLTRIMS is that the latter requires the use of a magnetic field produced by a Helmholtz coil to constrain electron trajectories. This is because electrons, having much smaller mass than the ions, obtain momenta of the same order of magnitude [61]. A magnetic field is not necessary while looking at one particle at a time in VMI, switching the polarity and strength of the electric field are the only changes required. The choice to use the VMI technique over COLTRIMS is based on the needs for our measurements.

Our current areas of investigation include characterization techniques for attosecond pulses as well as the observation and control of electron dynamics in atoms and molecules. Obtaining and analyzing the angularly resolved images of just photoelectrons alone is sufficient for these studies. Although COLTRIMS is more than capable for these tasks, acquisition times are orders of magnitude longer than those of VMI. This is because for coincident detection of ions and electrons to be defined uniquely, only a few events can be mapped at a time. The information from coincident measurements is redundant for the needs of the listed experiments, and the long acquisition times are unnecessary, so VMI is the best choice. The following sections describe the workings of TL-VMI and how data is acquired and analyzed – made to be a reference to any researcher interested in this technique.

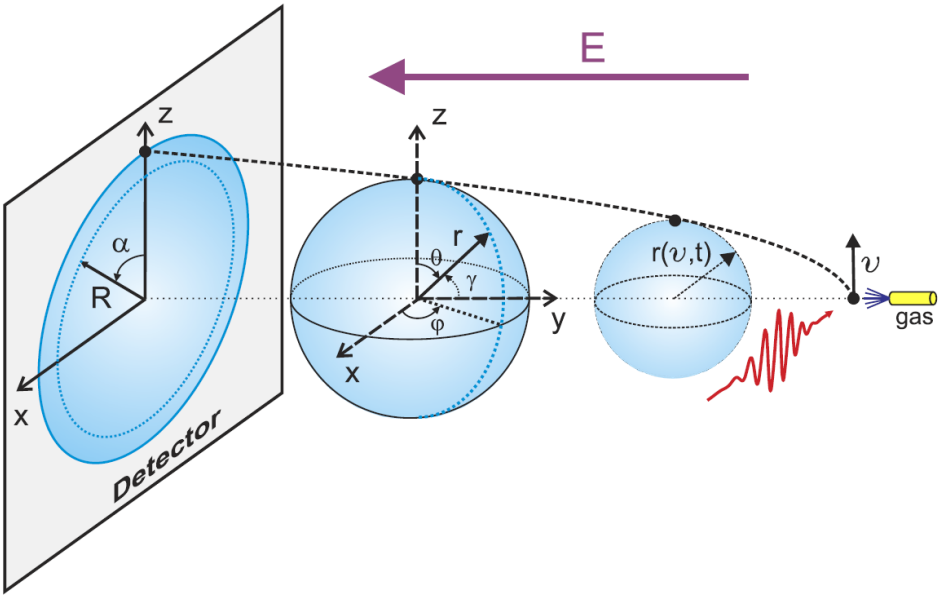

Figure 2.7: The illustrated scheme of the velocity map imaging process. An ultrashort pulse, with polarization perpendicular to the gas target, ionizes the atoms of the gas. An ejected photoelectron, having a given velocity vector, is guided by the electrostatic lens while expanding on a Newton sphere. The electron counts are recorded at a 2D detector surface. The important concept is that within the interaction region, electrons emitted with the same velocity vector are focused to the same point on the detector. Image adapted from [62].

2.5.1 Design and Principles of Operation

The TL-VMI is a design that inherited many of the same qualities of the original model while being upgraded to detect higher charged particle energies. A sketch is shown in Figure 2.8. The main motivation for this new concept was the arrival of keV light sources like x-ray attosecond pulses, and free-electron lasers that could produce keV charged particles. In comparison, setups with detection based on the standard design of VMI are only capable of measuring electrons at up to 100 eV [63, 64]. As stated before, the standard system has three electrodes - the repeller, extractor, and ground. The TL-VMI has eleven electrodes made of non-magnetic stainless steel with 1-mm thickness and outer diameters of 80-mm. The first electrode, the repeller, is held at potential V_R and has a 50-um hole where an effusive gas target flows out on axis of the TOF chamber. Next is the extractor held at V_E which is located 12 mm downstream and has an inner diameter of 40 mm. Directly between the repeller and extractor. The interaction region is defined by the crossing point of

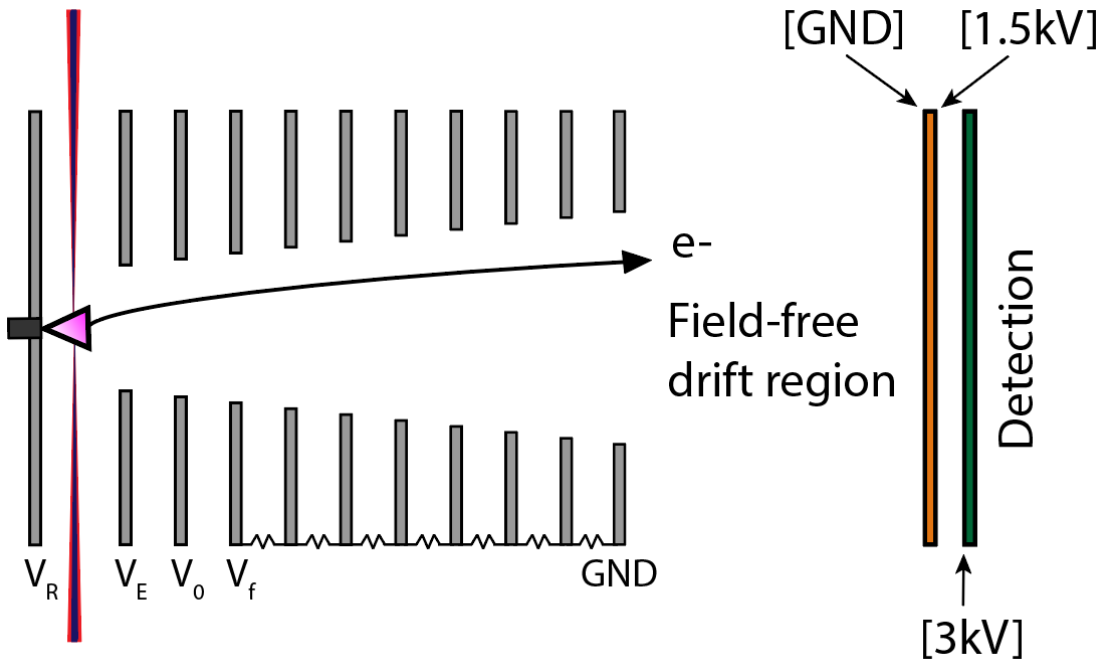

Figure 2.8: The schematic of the TL-VMI spectrometer.

the focused pump-probe beamline with the gas target. Starting from the extractor, electrodes are spaced by 6 mm and their inner diameters progressively increase by 2 mm. The first four electrodes are given their own voltage supplies. The fourth is called the focusing electrode, held at V_f. It plays an analogous role to the standard VMI extractor by controlling the resolving power. A typical practice is to decide the detection energy range, which scales with V_R, and adjust the repeller accordingly. The focal power is then optimized for this energy range with V_f. While this is done, a general rule of thumb is to set V_E and the third electrode so that there is a constant voltage drop across the first four plates. The rest of the plates from V_f to the ground are connected by resistors that divide the voltage to the other rings. An essentially field-free region extends for 55 mm from the ground to the detector. The entire TOF volume is protected from magnetic fields by a shield (MuMETAL). The shield and front face of the detector are also grounded.

Detection is achieved with a microchannel plate (MCP) and phosphor screen assembly (F2226-24P183, Hamamatsu). An MCP is a position sensitive device that consists of many narrow stacked channels that electrons can fly into. The front of

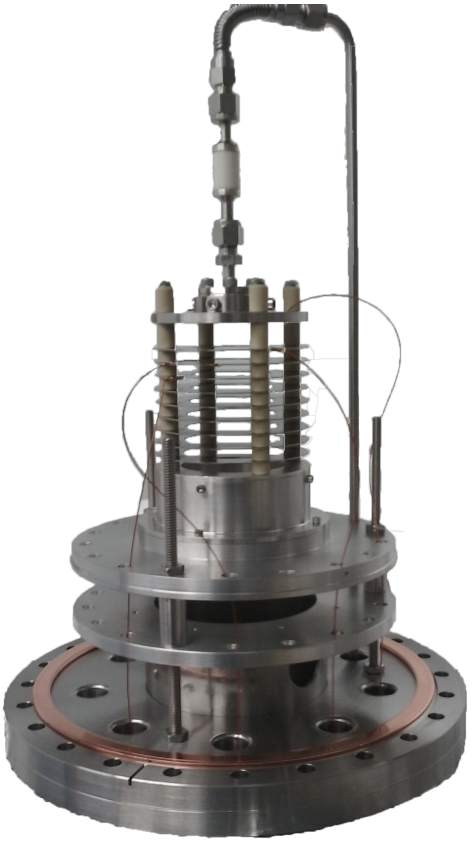

Figure 2.9: VMI system currently in use at ASAP before prior to installation in the target chamber. The line coming in through the top feeds the target gas through the repeller. It is easy to see the largest spacing between the repeller and extractor that gives room for the interaction region. The increasing inner radius of the ion lens electrodes is also apparent. The four wires supply the voltages V_R, V_E, V_x, and V_f, and the ceramic spacers (white) isolate the plates.

the MCP is held at ground while the back is placed at a positive potential of around 1.5 kV, but do not exceed 2 kV to avoid damage threshold. While ricocheting through the channel, one electron creates an avalanche of electrons that surges through obtaining gain of the order of 10^6 or higher. The phosphor screen which is next in line to receive the amplified electron signal has its front surface held at about 3 kV, but not exceeding 4 kV to avoid damage. The phosphor converts the electron signal to light through cathodoluminescence, which is detected by a scientific complementary metal-oxide semiconductor (sCMOS) camera (Edge, PCO). A camera lens assembly (NAVITAR) is placed before the camera to provide focusing adjustments of the image. Limitations exist on the detection and resolution of the

spectrometer, topics that are covered in the next section.

2.5.2 Detection and Resolution

An empirical relationship between the radius R of electron impact on the detector, its speed, v, and time of flight, t, is

$$R = Nvt \tag{2.8}$$

Where N is the magnification factor[37]. Because the attosecond pulse consists of an energy comb of harmonics, photoelectrons are ejected to further radii when ionized by photons with higher energy. The kinetic energy can then be expressed in terms of the radial position as

$$E = \frac{1}{2}m\frac{R^2}{(Nt)^2} \tag{2.9}$$

Meaning that energy is proportional to R^2. In order to measure the energy resolution, as related to the widths of the rings on the collector, we can use this equation and a derivative changing the d to a Δ. Since $\Delta E/\Delta R \propto 2R$ you can obtain $\Delta E \propto 2R\Delta R$ and dividing by E gives $\Delta E/E = 2\Delta R/R$ which allows the energy resolution to be deduced from the width of the radial peaks on the detector after events accumulate to a sufficient count. One source of the peak widths is that the laser-target interaction volume is finite. As the volume of the interaction region, estimated as a product of twice the Rayleigh range z_R times the square of the focal diameter, increases, $\Delta E/E$ decreases. Another contribution to resolution is that some emission angles with respect to the time of flight axis ie 45° and 135° will be focused to the same radial ring. This happens because, although the two velocity vectors may project the same radial distance from the axis, the time of flight will be slightly different. It is also true that the bandwidth of the XUV attosecond pulses can be used as a standard limit to resolution [65]. Regardless of whether a single attosecond pulse (SAP) or attosecond pulse train (APT) is being used, a higher limit to the resolution can be estimated by the transform limited bandwidth [65]

$$\Delta\omega = \frac{4ln2}{\tau_p}, \tag{2.10}$$

	Duration τ_p	Bandwidth ΔE
SAP	300 as	6.083 eV
SAP	600 as	3.042 eV
APT	5 fs	0.365 eV
APT	10 fs	0.182 eV
APT	15 fs	0.122 eV

Table 2.4: Bandwidth of selected SAP and APT durations which are assumed to be transform limited. The bandwidth of the SAP is the FWHM of the pulse in the frequency domain. The bandwidth of an APT is the FWHM of individual harmonics in the frequency domain. For either, the bandwidth can be used as a measure of the highest energy resolution limit.

where τ_p is the duration of the SAP or the duration of the APT. Bandwidth for a SAP is certainly easy enough to imagine, but it seems a bit like a misnomer in reference to APTs, for it defines the width of individual harmonics. A better name for this context might be the dynamic range of the given harmonic, but consistently calling $\Delta\omega$ the bandwidth will no doubt be less confusing. The energy resolution limit can then be calculated as

$$\Delta E = \hbar\Delta\omega = \frac{\hbar 4ln2}{\tau_p} \tag{2.11}$$

where a convenient value for $\hbar$ is 0.6582 eV·fs. In Table 2.4 some values for energy resolution limits for few SAP and APT durations are provided. It can be seen that longer APTs are associated with better energy resolution limits than a SAP. In contrast to what has just been shown, there will be more practical limitations based on the extent to which the electric field can be controlled.

Simulations for our model have been run [57] with SIMION (version 8, scientific instruments) comparing resolution performance of TL-VMI vs VMI for detecting electrons up to 360 eV when both systems have been optimized for performance in this energy range. Both had their best resolution at 125 eV, but the TL-VMI has a resolution at least 2.3 times better. The general way to optimize for an energy range is to scale V_R appropriately, then tune V_f to optimize the resolution for the energy in the middle of the range. Experimental evaluation yielded results of practical significance. In a scheme very similar to ours, V_R was set to -800 V and the focus voltage of $0.8V_R$ was used for photoelectrons with energies up to 25 eV.

In our experiments, electrons with up to about 20 eV can be observed routinely when odd harmonics, H11 to H23, of the fundamental laser field are generated in Argon as described in 2.4.2. A repeller voltage of -796 V with a V_f set to $0.755V_R$ is implemented, and a constant, progressive voltage drop is place across the first four electrodes. Resolution has been sufficient to conduct both pure RABITT, having only odd harmonics in the APT, and experiments with APTs consisting of both even and odd harmonics. A recent study we conducted in our lab found the duration of our APTs to be about 15 fs [62]. In the previous work discussed above [57] experimental performance under a similar setup and energy range of study, indicated that for lower energy detection, the APT bandwidth is the limit for resolution for VMI detection. Using Equation 2.11, our bandwidth sets the limits of our resolution to about 0.122 eV.

2.5.3 Data Acquisition and Analysis

During RABBITT scans, the photoelectron energy spectra are recorded as a function of delay between the APT and the IR or UV probe field. Our sCMOS camera takes images (1000 x 1000 pixels) recording the light flashes from the MCP-phosphor detecting electrons. Typical camera settings have about 5-s integration times set to collect photoelectrons from roughly 10^5 APTs per image (2 APTs for each IR pulse, repetition rate of 10 kHz).

The polarization of the ionizing photons defines a symmetric emission axis parallel to the detector surface. Thus, when photoelectrons are collected on the detector, they form a symmetric 2D angular distribution $P(x, z)$. The full 4π collection of the VMI and the symmetry of the interaction allows the reconstruction of the 3D angular distribution $I(r(v), \theta, \varphi)$ which is related to the 2D image $P(x, z)$ by the Abel Transform.

$$P(x,z) = \int_R^\infty \frac{I(r(v),\theta,\varphi)}{\sqrt{r^2 - R^2}} dr \tag{2.12}$$

The brute force method of evaluating the inverse Abel transform is computationally difficult and efforts have been made to get around the difficulties [53–56]. A new

algorithm was developed in our research group primarily accomplished by Geoffrey Harrison and Dr. Laurent, the DAVIS algorithm [62]. It was motivated by the approach of another method called the polar basis expansion (p-BASEX) [56, 66], which converts the coordinates of the image from Cartesian to polar reference system, expanding the 2D distribution with a polar basis set, and evaluating the Abel integral numerically. The DAVIS algorithm does reconstruction in an alternative way, that first models the distribution mathematically as an expansion of Legendre polynomials [67, 68] with the form of the 3D distribution

$$I(v,\theta) = F(v)\sum_{n=0}^{2N}\beta_n(v)P_n(\cos\theta) \tag{2.13}$$

The process is illustrated with the diagram in Figure 2.10. The main goal of the algorithm is to retrieve a radial function of velocity $F(v)$ and an asymmetry parameter β_n [68]. The DAVIS method is competitive to the other algorithms, in particular p-BASEX, both in speed and quality. It is faster because the algorithm works with matrices of lower dimension. It is less sensitive to noise during reconstruction because the data is effectively filtered since the raw data image is expanded with the Legendre polynomial basis set before inversion. The procedure computationally efficient, and user friendly making it a good choice for reconstruction.

2.6 Operational Conditions and Techniques

In order to bring the experimental setup to operational conditions, many steps of preparation must be performed. First we power on the laser at least 45 minutes before use so that the output average power has stabilized. Several diagnostic steps are taken at low laser power $\sim$ 600 mW. First we ensure that the laser beam is aligned through our two reference irises on the infrared probe path. This is carried out by "walking" the beam so that it is aligned by mirror and reference-iris pairs. One mirror and reference-iris is in place before the beamsplitter BS see Figure 2.3. The other pair has a mirror before BS, and the iris placed after. An eyeball measure for the quality can be done by the walking is to close the iris aperture that is

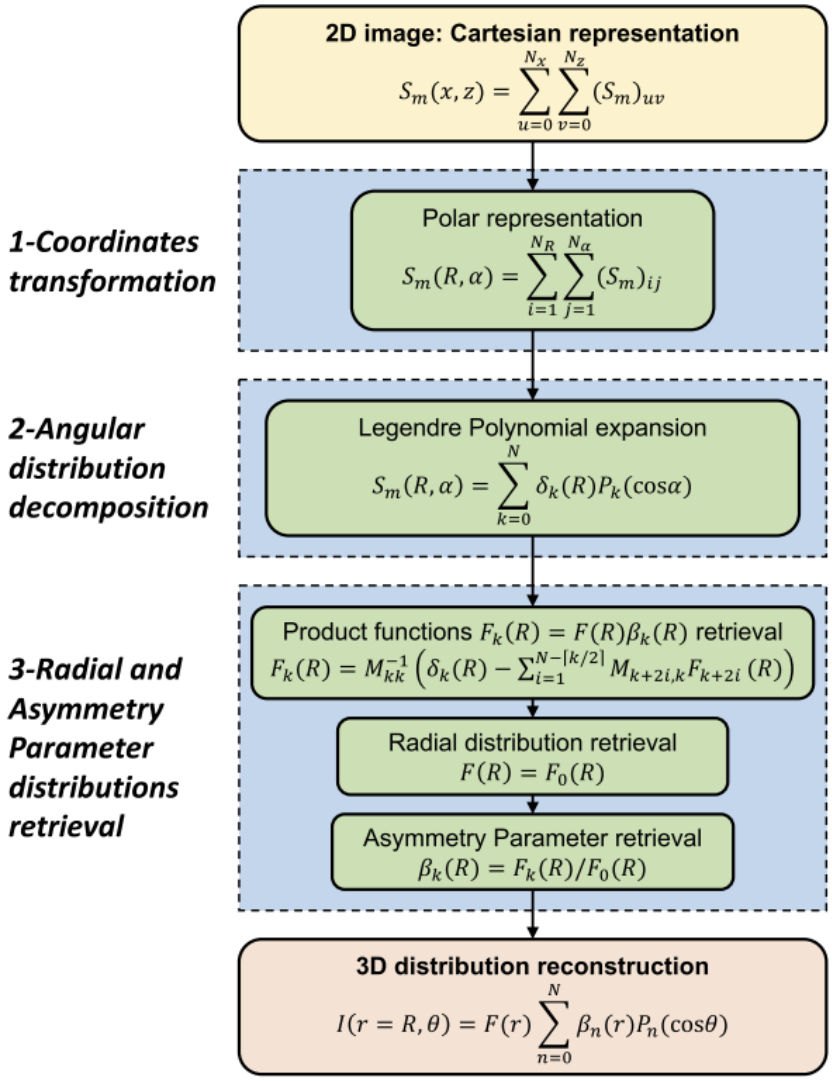

Figure 2.10: A flow chart illustrating the process of the DAVIS algorithm. The procedure consists of three steps. First, there is a Cartesian to polar coordinate transformation of the measured 2D raw image, second we expand the angular distribution with a sum of Legendre polynomials, and third, the radial and asymmetry parameter distributions are retrieved. Image adapted from [62].

currently being used and observing the Airy disk that is formed when the aperture is tightened. An Airy disk is surrounded by concentric rings of lower intensity, and if the beam is not aligned, the rings will be cut asymmetrically by the iris. Corrections are made with these reference optical element pairs until the beam is aligned at both iris apertures. Next we check to make sure that we have spatial and temporal overlap. In most cases, temporal overlap remains from day to day as long as optics aren't added or removed from the experimental setup. To obtain spatial overlap, the

movable mirror MM is inserted into the path to make use of the CMOS beam profiler (Dataray). The CMOS is placed at the same distance from the RM as the interaction volume so that the quality of the pump-probe overlap on the target can be observed. With the gas of the HHG chamber turned off the low power IR beam in the XUV pump beamline is used to mimic the placement of the APT since attosecond pulses are produced twice each optical cycle of the IR pulses. The Al filter just past the HHG chamber is removed so that the IR is not attenuated. Spatial overlap is achieved by taking the overlapped beams, finding constructive interference, and adjusting the pointing with mirror MI3 until maximum constructive interference is obtained. If temporal overlap must be found, then coarse adjustments to MI1 can be made to quickly find it. Once the femtosecond IR pulses are overlapped, the pump APT will be overlapped with the probe pulse.

With temporal and spatial overlap found, the output power is increased at the amplifier output back up to about 15 W. Gas such as argon or neon is then supplied to the HHG chamber with a backing pressure of tens to hundreds of mbar. At this point, the phase matching can be optimized for producing the best harmonic spectrum desired. The X-Y translation stage on the HHG chamber is used to adjust the position of the generating gas until the laser focus is about 3 mm before the gas capillary. Doing this prepares conditions for selecting the short trajectories of HHG [51]. An iris placed before the HHG chamber also allows the spatial profile to be trimmed as an additional parameter in the optimization. There are two simultaneous methods for checking the quality of the harmonics. The first method is that the XUV spectrometer can be used to see the harmonic spectrum directly. The second is that the VMI can be turned on and the target gas can be supplied so that the quality of the photoelectron spectrum can be observed. These two methods are complementary because while the VMI has a sensitivity to photoelectrons associated to photoelectrons emitted from the lower energy harmonics, the XUV spectrometer is more sensitive to the higher energy harmonics.

Once the harmonics are optimized, the probe characteristics can be adjusted to obtain the ideal polarization and intensity. A way to do this is to increase the

intensity of the probe until ATI is observed. A photoelectron angular distribution will appear whose top and bottom half will display a maximum vertical spread when polarization is vertical. This is opposed to having the polarization parallel to the flight axis, for which case the photoelectrons will eject directly down the center of the flight axis. With the polarization fixed, the intensity can be reduced just below the threshold required for ATI. the final step in preparation for the measurement is tuning the stabilization system.

In this chapter, the development of the experimental setup has been presented. The pros and cons of different schemes have been compared and contrasted. Also shown are the schematics, resolution capabilities, and the advantages and disadvantages of our apparatus to provide a more complete scope of the state of the art while giving thorough details of our facility. The active stabilization system is also an essential part of the experimental setup, but that is the subject of the next chapter.

"The intentions of a tool are what it does. A hammer intends to strike, a vise intends to hold fast, a lever intends to lift. They are what it is made for. But sometimes a tool may have other uses that you don't know. Sometimes in doing what you intend, you also do what the knife intends, without knowing."

— Philip Pullman *The Subtle Knife*

3

An Optically-Locked Interferometer for Attosecond Measurements

Contents

3.1 Introduction

In this chapter, I present the design and performance of the active stabilization system for our attosecond pump-probe setups based on a Mach-Zehnder interferometer configuration. The system employs a CW laser propagating coaxially with the pump and probe beams in the interferometer. The stabilization is achieved with a standalone feedback controller that adjusts the length of one of its arms to maintain a constant relative phase between the CW beams. With this system,

the time delay between the pump and probe beams is stabilized within 10 as rms over several hours. The system is easy to operate and only requires a few minutes to set up before any pump/probe measurements.

Recently, the advent of extreme-ultraviolet (EUV) light pulses in the attosecond time scale has opened up new avenues for experimentalists to probe temporal aspects of electron transitions in atoms, molecules and complex systems with unprecedented precision [1, 7, 17, 21, 22, 24, 69]. In general, the temporal characterization of a given electronic process is measured by exposing the target to both an attosecond pump pulse ($\sim$ 100 as) and a phase-locked optical IR probe field, with a variable time delay between the two. To fully exploit the temporal resolution of attosecond pulses for time-resolved study using such a pump-probe approach, the time delay between the pump and probe pulses must be controlled with an attosecond resolution as well. This requires the ability to linearly vary the delay with time steps of the order of the pulse duration (or less), and, more importantly, to maintain it to any desired value over extended periods of time.

The major difficulty to achieve such temporal resolution comes from the fact that the spatial extent of an attosecond pulse is of the order of a few tens of nanometers ($\sim$ 30 nm for a 100-as pulse). As a consequence, any nanometer- scale fluctuations of the path length difference between the paths followed by the pump and probe beams inevitably lead to a timing jitter of the order of magnitude of the pulse duration itself. Such nanometer-scale fluctuations are generally inherent in any experimental setup due to beam pointing instabilities, thermal expansion of the optical table, or vibrations of the mechanical structure of the optical system resulting from the surrounding environment (air flow, vacuum pumps, chillers, etc.). The timing jitter can be reduced down to a few attoseconds by using an experimental setup with collinear geometry where both the attosecond pump and IR probe pulses propagate along the same path up to the target [29, 70]. Unfortunately, a collinear geometry prevents the user from being able to independently modify the temporal and spatial profiles of the IR pump, or XUV probe beams. Due to the increasing number of techniques that use a temporally-shaped driving field for the attosecond pulse

generation [71, 72] and/or the necessity to tune the properties of the IR probe for a particular time-resolved experiment [73], Mach-Zehnder interferometers, where the two pulses propagate along different paths, emerge as a more popular scheme in the community even though they are generally less stable [36, 74, 75].

When mentioning the passive stability for pump-probe setups in this chapter, this is referring to how precisely and reliably the delay control performs its task without support from a closed loop stability system. When mentioning active stability, this refers to the precision maintained when additional measures are taken by installing additional instrumentation into a closed loop stability system. Such a system includes optics, electronics, and feedback control devices to supplement the passive stability. Besides having a room with optimal conditions such as temperature regulation and vibration damping optical tables, experimental geometries are of utmost importance with regard to stability limits. There are two atto-beamline geometries that are frequently used, the collinear geometry where the attosecond pump and femtosecond probe take the same path sharing special or custom optics, and the Mach-Zehnder layout which splits the laser into spatially separated paths. Figure 2.1 shows the layout of these geometries and explains the pros and cons of each.

3.2 Contemporary Methods in Active Stabilization

To improve their stability, a few active stabilization systems have been already proposed [27, 28, 75, 76]. They are generally based on a CW laser propagating in both arms of the interferometer. The stabilization is achieved with an active feedback system that adjusts the length of one arm of the interferometer to maintain a constant relative phase between the two waves. The implementation of such a relatively simple approach to attosecond pump/probe setups is not straightforward, though. Indeed, a metallic foil is generally placed in the attosecond beam path to filter out the attosecond pulses from their driving IR field, which also prevents the propagation of the CW stabilizing beam. To circumvent this issue, one practical

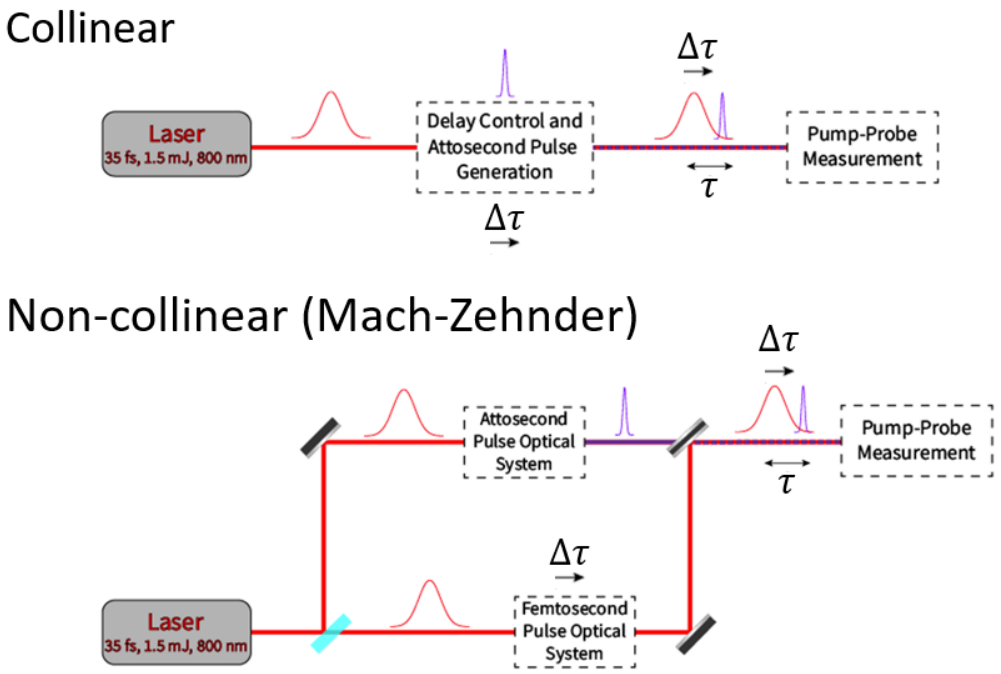

Figure 3.1: The two most commonly implemented pump-probe configurations. The collinear setup combines both the femtosecond probe, and attosecond pump beams into a single arm by sharing most of the same optical elements. It offers the most stable configuration. The non-collinear (Mach-Zehnder) setup separates the two beams into separate arms allowing the most tunability in each beamline, but it is generally less stable.

approach consists in propagating the CW laser in a spatially separate path adjacent to that followed by the attosecond and IR beams. Successful designs for setting up non-collinear schemes have been recently proposed, which have demonstrated long-term stability of pump-probe delay as low as 50 as [28, 75]. Nevertheless, despite their versatility, these non-collinear approaches only allow for a partial stabilization of the interferometer as the optics forming the separate path acquire an additional drift to that of the main path.

The coaxial propagation of the CW laser and the attosecond beam in the interferometer can be achieved by using a small-diameter metallic filter (2-3 mm) that allows a portion of the CW to pass around it [27, 76]. In such configuration, the CW beams traveling along with the attosecond and the IR beams exit the interferometer non-collinearly. This effect is due to the inherent wedge-shape of the recombination mirror. A position sensitive detector (CCD or CMOS camera) is then required to capture the interference pattern where the two beams cross.

Characteristic fringes appear for such an interference, and the spacing between them is dependent on the phase difference between the two waves. In the crossing of the waves, assume that the first is incident on a screen at normal incidence, while the second is incident at an angle β. Recounting that the phase of a plane wave is

$$\phi = \boldsymbol{k} \cdot \boldsymbol{r} - \omega t, \tag{3.1}$$

where the wave vector $\boldsymbol{k}$ is in the direction of propagation having a magnitude $k = \dfrac{2\pi}{\lambda}$, and λ is the wavelength of the light. In a simple case where the first beam propagates in the $\hat{z}$ direction, the wave vector is

$$\boldsymbol{k}_1 = \frac{2\pi}{\lambda}\hat{\boldsymbol{z}} \tag{3.2}$$

The wave coming in having an incidence at β, which we can say lies in the x-z plane must have a form that satisfies that its magnitude is equal to what was already mentioned, as well as reducing to Equation 3.2 when β is zero. The second wave thus has a form $\boldsymbol{k} = k_x\hat{\boldsymbol{x}} + k_z\hat{\boldsymbol{z}}$ where the following equation satisfies all the aforementioned conditions,

$$\boldsymbol{k}_2 = \frac{2\pi}{\lambda}\left(\sin(\beta)\hat{\boldsymbol{x}} + \cos(\beta)\hat{\boldsymbol{z}}\right) \tag{3.3}$$

If wave one has traveled an extra distance L, the phase difference $\Delta\phi$, which the intensity depends upon is then

$$\Delta\phi = \frac{2\pi}{\lambda}\left(\sin(\beta)x + \cos(\beta)z - (z + L)\right) \tag{3.4}$$

Maxima will of course occur when $\Delta\phi = n \times 2\pi$ where n is an integer. With some rearrangement, (5.4) can then show the location and spacing of the fringe maxima:

$$x_{max} = \frac{n\lambda}{\sin(\beta)} + x_0 \tag{3.5}$$

where $x_0 = (L + z - \cos(\beta))/\sin(\beta)$. The relative phase between the two beams are deduced from the shifts of the interference fringes using Fourier-transform interferometry [77]. This elegant approach is relatively easy to implement provided that interference fringes of good contrast are formed. However, the use of a position

sensitive detector puts a limit on the maximum feedback frequency achievable (typically below 30 Hz), which is defined by the exposure time of the camera plus the computational time required to extract the relative phase from the imported 2D image. In addition, the maximum achievable stability is limited by the level of accuracy in the retrieval of the relative phase, which in turn depends on the spatial resolution of the camera and/or the number and the quality of the interference fringes, for example.

3.3 Active Stabilization System

A schematic view of the active stabilization system is shown in Figure 3.2. It allows us to continuously control and stabilize the path length difference between the two arms of the interferometer to practically any desired value. It is based on a 5-mW continuous wave (CW) green laser (λ = 532nm) propagating in the Mach-Zehnder interferometer coaxially with both the attosecond pump and IR probe beams. The stabilization is achieved with an active feedback system based on proportional–integral (PI) control that adjusts the length of one interferometer's arm (the one followed by the IR beam) to maintain a constant relative phase between the two waves. A photodiode capturing the optical intensity fluctuations induced by any phase shift between the two interfering waves provides a feedback signal to a high-speed piezo controller, which corrects in return the position of the mirror MI2 to maintain the optical intensity at a constant value. The control of the relative path length between the two arms of the interferometer, on the other hand, is achieved with a phase shifter [78] that imparts a controlled relative phase between the two waves forcing the mirror MI2 to move to a desired position.

3.3.1 Implementation of PI Control

For a given system whose current state y(t) can be measured with a signal S(y(t)), disturbances of the system will be evident as errors e(t) in S(y(t)). An accessible example which is related to our situation is the measurement of a signal (say voltage) representing position x(t) of an object. If we wish to maintain a steady position

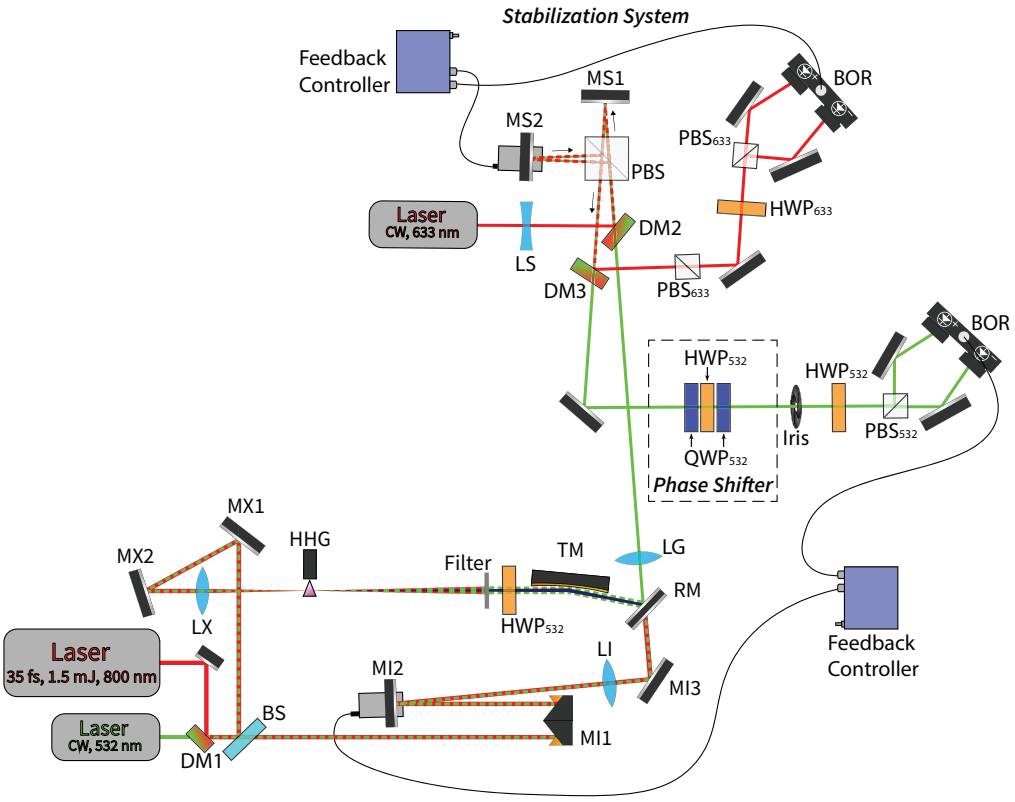

Figure 3.2: Schematic view of the optical actuator, which allows both the stabilization and the control of the Mach-Zehnder interferometer used in the attosecond beamline. It is based on a 532-nm CW laser propagating in the interferometer coaxially with both the attosecond and IR beams. The stabilization is achieved with an active feedback system that adjusts the length of one arm of the interferometer to maintain the relative phase between the two waves constant. A phase shifter, on the other hand, imparting a controlled relative phase to the waves, is used to adjust the relative path length between the two arms of the interferometer to any desired value.

y_0 (with signal $S(y_0)$), called the set point, but a disturbance forces the object to deviate to y_e then the error is defined as the distance from the current position to the set point $e(t) = y_0 - y_e$. A common way to correct for disturbances is to use a proportional–integral–derivative (PID)controller, a feedback loop mechanism continuously responds with a response described mathematically as a summation of three terms: one term proportional to error, a term proportional with a time integral with the error, and one with a derivative:

$$u(t) = k_P \cdot e(t) + k_I \cdot \int_0^t e(t')dt' + k_D \cdot \frac{d}{dt}e(t). \tag{3.6}$$

This equation can also be expressed in terms of an overall gain and time constants.

$$u(t) = k_P \left(e(t) + \frac{1}{T_I} \cdot \int_0^t e(t')dt' + T_D \cdot \frac{d}{dt} e(t) \right). \tag{3.7}$$

Although our system utilizes only proportional-integral (P-I) feedback control, the action of all three terms can be described to give a full picture. The proportional term gives the error, that is it gives a base rate at which the system responds to reduce the error. The integral term tracks the progress with time that the system is making to reduce the error to zero. If the response of the proportional term alone is not driving the error to zero as needed (perhaps the system meets some resistance) the integral term is summing this effect and uses it to ramp up the base response until it drives the error down. Either way, as the error approaches zero, the proportional term does too while the integral term balances and finally approaches zero as well. The derivative term plays an important role. It keeps track of how fast the error is changing. If the integral term cause a large transient response, the feedback may cause the system to overshoot the desired setpoint. This is undesirable in many systems. By tracking the rate of approach to the [zero] setpoint, and adding an initial reponse that causes the response to slow down, overshoot is minimized or avoided. If overshoot is not too serious of a problem, then the two essential parameters are just the P-I terms, which is what we are equipped with.

In a typical PI controller, such as the one we are using(LB1005, New Focus), two input signals are usually required. The inputs here are voltages (Figure 3.3). One signal is the output of the system (not PI controller, but the experimental setup) $V_s(t)$ and the other is the reference signal $r(t)$. The signal that the balanced optical receiver provides as an input is a cosine, so it is centered at zero. No reference $r(t)$ is used, so zero is the effective set point r_0. The PI controller can be adjusted with a few main parameters. The overall proportional gain k_P affects all three terms as seen in equation 3.8. The PI filter is saturated when the strength exceeds 330 mV, so the input is preemptively conditioned to be within +/- 300 mV. The PI corner frequency defines the -3 dB point for which all lower frequencies have the integral effect as the dominant term, and the proportional term dominates all frequencies

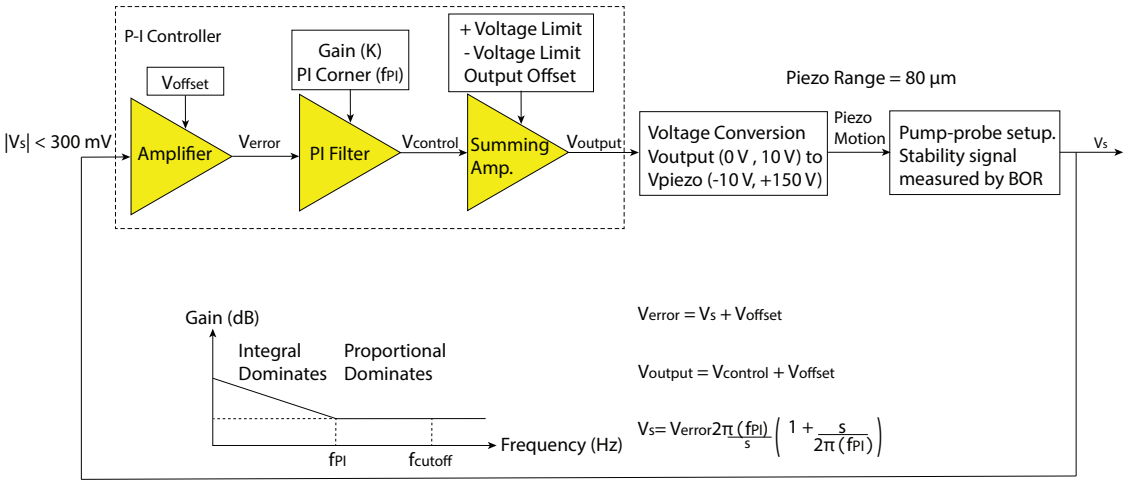

Figure 3.3: The P-I control schematic in a closed loop configuration. On the far left, the output V_s is fed back to the P-I controller. The setting V_{offset} is used to set the signal to be centered at zero. The overall gain and PI corner frequency define the filter, and the output control signal is amplified within the voltage limits. Next, this output voltage is sent to the piezo voltage amplifier which converts the output voltage into the range used by the actuator. The piezo transducer responds to correct the system, and finally the interference is measured again to measure the stability of the interferometer.

beyond. The piezoelectric amplification module(12V40, piezosystem jena) that drives the mirror stage has a resonance located at 400Hz, and since the PI corner frequency does not define a cutoff the use of a low pass filter is required to stay safely away from this point. The piezo amplifier is supplied externally by a 12-volt power supply. The output of the PI controller is a signal with limits calibrated in a dynamic range of 0.1 to 9.9 volts (the full range is 0 V to 10 V, but we don't want to force the piezo to it's furthest limits and cause it to break). The voltage in this range is converted to a voltage in the larger range of -10 V to 150 V which corresponds to the range of motion for the stage of $80\mu m$.

3.3.2 Optical System

The vertically polarized CW laser beam first combines with the femtosecond IR beam by traveling through a broadband dichroic mirror (DM1) located outside the attosecond beamline, and subsequently enters the interferometer through the beamsplitter (BS). Both the transmitted and reflected beams propagate up to the

hole-drilled recombination mirror where they exit the interferometer by traveling through the hole and by reflecting off the back of the mirror, respectively. On its way toward the recombination mirror, the outer part of the reflected beam first passes around the thin-metallic filter, while its central part is blocked, and then its polarization is rotated by 90° with a hole-drilled half-wave plate. At the recombination mirror, the reflected and transmitted beams are thus orthogonally-polarized. Due to the inherent wedge-shape of the mirror, the beams are also not perfectly coaxial at the exit of the interferometer.

The angle occurs because, even with careful manufacturing, the reflective faces are not perfectly parallel to each other resulting in a slight wedge shape. For measurements to work, it is necessary for RM to be adjusted so that the attosecond pulse train (APT) and probe pulses recombine and propagate coaxially onto the target in the VMI chamber. Because of that alignment, the angle between the CW beams appears. This deviation angle is corrected by a compact Michelson interferometer (5-cm arm length) where they are first spatially separated with a broadband polarizing beam-splitter (PBS), and then reflected back toward the beamsplitter to recombine. By using a [broadband] polarizing beamsplitter (PBS) (PBS-251, Thorlabs) instead of a non-polarized type, the orthogonally polarized CW beams are separated from each other. It is not an intended use for a PBS to act as a recombination point, this needs further explanation.

Briefly, the PBS is made by taking two prisms and applying a dielectric coating to the base of one. The prisms are then cemented together to form a cube. When the beamsplitter is mounted as instructed, p-polarized light is transmitted while s-polarized light is reflected. The transmission and reflection of the beams by polarization are better than 90% and 95.5% respectively. Since PBS is the beamsplitting element of the Michelson optics, the CW beams reflect back into the PBS to recombine. This use of the PBS works well, but it was designed with transmission and reflection ocurring with an incoming beam from the side with the dielectric coating. So any future use where higher laser power is desired should be

exercised knowing that cemented optics have lower damage thresholds than standard optics. These lower thresholds are due to absorption and scattering in the cement.

The incidence of the CW laser to the faces of the PBS and mirrors MS1 and MS2 are not normal, and the faces of the PBS and Mirrors are not parallel. Therefore the point at which the polarized waves split at the dielectric coating and the point at which they recombine are not the same. This is done on purpose because we are not using the Michelson as an intererometer, but as an optical system to correct the angle between them. With a proper alignment of the flat mirrors (MS1, MS2), the orthogonally-polarized returning beams exit the Michelson interferometer collinearly.An indication that we have achieved this is that instead of seeing the vertical fringes that appear for beams that have an angular convergence, we see circular fringe patterns that can only arise when the two waves are coaxial. There is enough displacement between the points where the light is split and recombined so that the beam can be sent into a balanced homodyne detection system composed of a half-wave plate oriented at 22.5°, a polarizing beamsplitter (PBS532), and a balanced optical receiver (BOR) for the measurement of their relative phase. It can be readily shown that the relative phase ' between the two waves is encoded into the signal S measured by the receiver as:

$$S \propto E_{XUV} E_{IR} \cos(\omega\tau). \tag{3.8}$$

where E_{XUV} and E_{IR} are the amplitudes of the waves traveling along the XUV and IR arms of the interferometer, respectively. The full mathematical description will be shown in the next section and will incorporate the effects of the above mentioned optics , the phase shifter, and the balanced optical receiver. As Equation 3.6 indicates, any fluctuation of the relative phase due to instabilities in the interferometer leads to a modulation of the signal S measured by the balanced receiver. The stabilization is thus achieved by maintaining the signal S constant (equal to 0) with a feedback loop. The receiver provides an error signal to a high-speed PI piezo controller that adjusts in return the position of the mirror MI2 in the interferometer to correct the phase shift between the two waves. For the

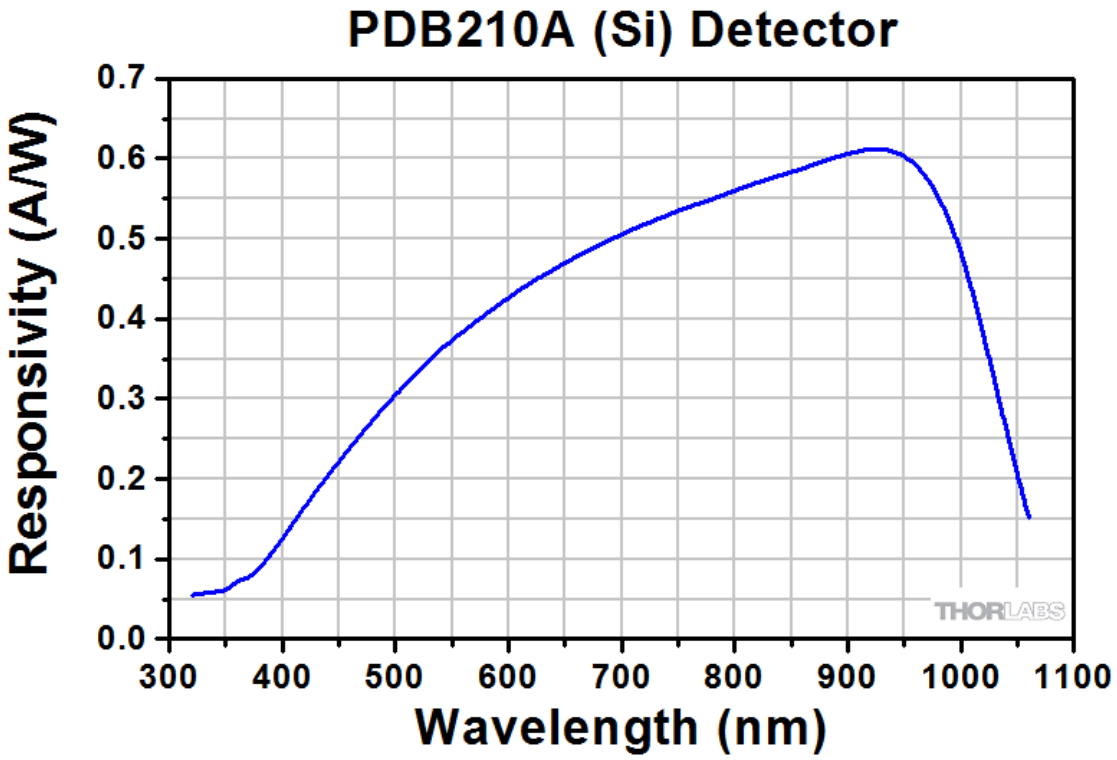

Figure 3.4: The responsivity of the BOR (PDB 210-A, Thorlabs). This measure of the photocurrent per unit of power shows an increasing efficiency for increasing wavelength. We currently use a reference laser at 532 nm. A longer wavelength reference laser could in principle offer not only a better responsivity, but more precision in the error control since the optical cycle is longer (Smoother dynamic range to measure pilot beam intensity).

sake of driving the piezo stage safely below its resonance frequency (∼400 Hz), the high-frequency components (>300 Hz) of the error signal are filtered out with a low-pass filter before feeding it to the controller. I designed, assembled and tested the RC low-pass filter before using it in the setup. I considered the -3dB point as the cutoff. A filter design for $300Hz$ using a resistor of 470Ω requires a $1.13\mu F$ capacitor in parallel. With the parts on hand I substituted a parallel use of a 1-uF and 100-nF in its place placing the cutoff approximately at 308 Hz, still safely below the resonance. The coaxial line coming from the balanced photodetector was split, where one part of the signal was sent to an oscilloscope so that $S(x(t))$ could be monitored, and the other line is connected in series to the filter which is sent to the P-I module. Because the high frequencies are filtered from $S(x(t))$, the P-I module does not measure them and there is no response to frequencies near or above the

resonance. This will be seen in the section 3.4 on the results.

To ensure that the relative phase measured by the receiver is uniquely related to the instability in the Mach-Zehnder interferometer, the Michelson interferometer is also stabilized. The stabilization system is similar to the one used in the Mach-Zehnder interferometer. It is based on a 633-nm CW laser polarized at 45° with respect to the vertical direction. The laser beam's divergence is first slightly increased with a concave lens (LS) to match the angular deviation between the two orthogonally-polarized 532-nm CW beams. The beam then combines with the 532-nm beams by reflecting off a dichroic mirror (DM2) and it is finally sent into the interferometer, where its s- and p-components propagate independently in each arm. After exiting the interferometer, the beam is separated from the 532-nm beams with a second dichroic mirror (DM3), and the relative phase between its s- and p-components is measured with a second balanced homodyne detection system and stabilized with a feedback loop in a similar way to that described above for the green CW laser.

3.3.3 Delay Control

An Evans' phase-shifter [78, 79] placed at the exit of the Michelson interferometer is used to adjust the position of the mirror MI2 and thus vary the relative time delay between the IR and attosecond pulses. It imparts a controlled relative phase between the two 532-nm waves that forces the mirror to move to a new position so that the signal S measured by the balanced receiver remains constant. It is composed of two quarter-wave plates oriented at +45° with respect to the direction of polarization of the incoming CW beams, and a rotatable half-wave plate located in between that controls the relative phase imparted to the CW beams. The effect of a waveplate can in general be described with the Jones matrix [80]

$$M(\theta) = \begin{pmatrix} \cos^2\theta + \xi\sin^2\theta & \sin\theta\cos\theta(1-\xi) \\ \sin\theta\cos\theta(1-\xi) & \sin^2\theta + \xi\cos^2\theta \end{pmatrix} \tag{3.9}$$

Where ξ is an exponential phase term that is characteristic to the optical element, and θ is an angle with respect to p-polarization (horizontal polarization). For

example, the values of ξ for a linear polarizer, a quarter waveplate, and half waveplate are 1, $e^{i\pi/2}$, and $e^{i\pi}$ respectively. Waveplates operate from the principle that the index of refraction of some materials is wavelength dependent as well as polarization dependent. Due to molecular structure in the material, polarization along one axis, the fast axis, a given wavelength will travel faster than when its polarization is oriented with the slow axis. The material thickness is cut so that fractions of a wavelength of delay can be created between the polarization components on the fast axis to the slow axis. A common use of a half-wave plate is to rotate the polarization orientation of linearly polarized light. Having the fast axis oriented at θ with respect to the initial polarization will rotate the orientation by 2θ. A quarter-wave plate is commonly used to convert linearly polarized light into circularly polarized light when the fast axis is at 45° with respect to the polarization. With special combinations of these waveplates interesting effects, like the one about to be shown, are possible. Jones matrices for a quarter-wave plate (QWP) and half-wave plate (HWP) are written as:

$$M_{QWP}(+45^\circ) = \frac{e^{i\pi/4}}{\sqrt{2}} \begin{pmatrix} 1 & -i \\ -i & 1 \end{pmatrix} \tag{3.10a}$$

$$M_{HWP}(\theta) = \begin{pmatrix} \cos 2\theta & \sin 2\theta \\ \sin 2\theta & -\cos 2\theta \end{pmatrix} \tag{3.10b}$$

The effect of the phase shifter on the incoming CW beams is mathematically expressed by the product of the Jones Matrices from Eqs. 3.8a and 3.8b as $M_{QWP}(+45^\circ) \cdot M_{HWP}(\theta) \cdot M_{QWP}(+45^\circ)$.

$$M(\theta) = \begin{pmatrix} e^{-i2\theta} & 0 \\ 0 & -e^{i2\theta} \end{pmatrix} \tag{3.11}$$

where θ is the angle between the horizontal direction and the half-wave plate's fast axis. As the matrix M indicates, the phase-shifter imparts to the orthogonally-polarized waves a relative phase equal to $4\theta + \pi$. By rotating the half-wave plate, the relative phase can thus be continuously tuned, so as the position of the mirror MI2 (2128 nm per revolution). A picture of the effects in the figure below: The effects of this phase shifter and balanced homodyne detection can be explained with the sequential effects on the waves after they have left the Michelson optics.

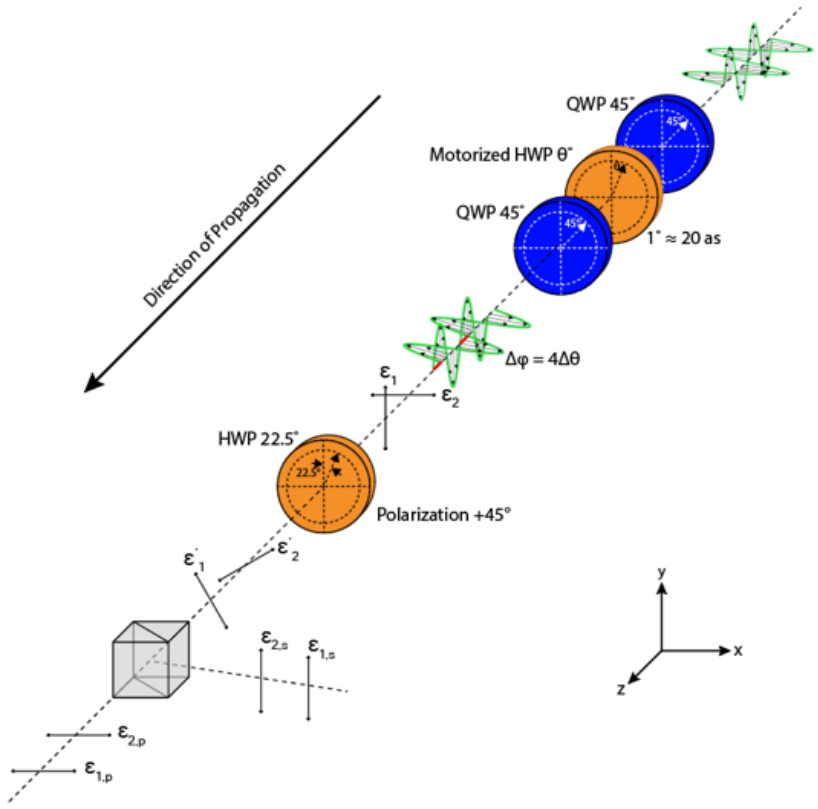

Figure 3.5: The effects of the Evans phase-shifter, and remaining optics leading up to the balanced homodyne detection, are shown on two orthogonally polarized waves of the reference beam. The waves propagate from the top right to the bottom left. A phase is added between them shown as a red line segment. The polarization picture is then used to show that HWP rotates each polarization. Finally the PBS separates the vertical and horizontal components. Mirrors then direct the two intensities to the BOR where the signal $S(x(t))$ is measured.

In the top right corner of Figure 3.2, the orthogonal waves propagate toward the phase-shifter, and can be expressed with the equations

$$\tilde{\boldsymbol{E}}_{IR} = E_{IR,0} \cdot e^{i(kz-\omega t+\omega\tau)}\hat{\boldsymbol{x}} \tag{3.12a}$$

$$\tilde{\boldsymbol{E}}_{XUV} = E_{XUV,0} \cdot e^{i(kz-\omega t)}\hat{\boldsymbol{y}} \tag{3.12b}$$

After the phase shifter, the added phase of $+/-2\theta$ to vertical/horizontal light results in

$$\tilde{\boldsymbol{E}}_{IR} = E_{IR,0} \cdot e^{i(kz-\omega t+\omega\tau-2\theta)}\hat{\boldsymbol{x}} \tag{3.13a}$$

$$\tilde{\boldsymbol{E}}_{XUV} = E_{XUV,0} \cdot e^{i(kz-\omega t+2\theta)}\hat{\boldsymbol{y}} \tag{3.13b}$$

After the phase-shifter, the light waves approach the HWP at 22.5° which rotates the polarizations, effectively giving each a vertical and horizontal component:

$$\tilde{\boldsymbol{E}}_{IR} = \frac{E_{IR,0}}{\sqrt{2}} \cdot \left(e^{i(kz-\omega t+\omega\tau-2\theta)}\hat{\boldsymbol{x}} + e^{i(kz-\omega t+\omega\tau-2\theta)}\hat{\boldsymbol{y}} \right) \tag{3.14a}$$

$$\tilde{\boldsymbol{E}}_{XUV} = \frac{E_{XUV,0}}{\sqrt{2}} \cdot \left(e^{i(kz-\omega t+2\theta)}\hat{\boldsymbol{x}} - e^{i(kz-\omega t+2\theta)}\hat{\boldsymbol{y}} \right) \tag{3.14b}$$

After this the polarization components are separated with the polarizing beamsplitter. Since they are coaxial, they interfere. The Interferences of each polarization are:

$$I_x = \frac{c\epsilon_0}{4}\left[E_{IR}^2 + E_{XUV}^2 + 2E_{XUV}E_{IR}\cos(\omega\tau - 4\theta)\right]. \tag{3.15a}$$

$$I_y = \frac{c\epsilon_0}{4}\left[E_{IR}^2 + E_{XUV}^2 - 2E_{XUV}E_{IR}\cos(\omega\tau - 4\theta)\right]. \tag{3.15b}$$

With a better picture of the polarization effects, the action of the BOR mentioned in section 3.3.1 (PDB 210-A, Thorlabs) can be better explained. It collects the two intensities individually in each one of its two photodiodes. The PDB 210-A consists of two large-area photodiodes, and an ultra-low noise, high-speed transimpedence amplifier. It generates an output voltage that is proportional to the difference of the photo currents of the photodiodes. The difference signal when both active stabilization and delay control are in use will have a form resembling Equation 3.6 with the addition of the added phase from the phase shifter:

$$S \propto E_{XUV}E_{IR}\cos(\omega\tau - 4\theta). \tag{3.16}$$

So it is easily seen that a benefit of such a balanced homodyne detection system is that DC and additional common noise that propagates in each arm even after change in polarization is cancelled out by the detection. We operate the CW laser at 5 mW, well below the damage threshold for the balanced photodetector of 20 mW. Using a rotational stage (URS50BCC) with sufficient angular precision (typical accuracy of ±10 mdeg), the time delay between the IR beam and the attosecond pulse is controlled with an accuracy down to a few attoseconds ($\sim$ 20 as per degree).

The active stabilization system is used routinely in our laboratory to control and stabilize the delay between the attosecond and the IR pulses. It is easy to operate

and only requires a few minutes to set up before any pump-probe experiments. We present below some measurements that demonstrate its capability to control the time delay between the two pulses with an attosecond temporal resolution and to maintain it to a given value over several hours.

3.3.4 Stability Measurements

A typical long-term measurement of the relative path length drift in the Mach-Zehnder interferometer without active stabilization is shown in Figure 3.6.a. The measurement was taken during day-time when the level of vibration in the laboratory is nearly at its maximum. The relative path length drift was deduced from the interference pattern produced by the 532-nm laser and captured by the CMOS camera (WinCamD XHR, DataRay) located at the exit of the interferometer. An image of the 2D pattern was recorded every second. To measure a strong signal, for as little signal to noise ratio as possible, I developed an algorithm that would used the central intensity peak of the interference pattern captured. The challenge to this is that over long periods of time, hours long, not only will the intensity fluctuate due to the jitter of the interferometer path length difference, but the position of the spatial pattern itself will drift around on the CCD surface. It was very fortunate that such drifts do not result in the intensity to completely leave the sensitive region. Thus a careful programmatic design could, in theory capture the signal.

The camera data acquisition was fully controlled with LabVIEW, which allowed us the capability to record and process the raw data all at once. To record the signal, my algorithm had to do three things reliably. First, the central intensity peak had to be recorded, so the first feature added was one that allowed the user to take a freely moving cursor on the X-Y graph and easily place it on the center of the intensity as well as a user defined radius r_u that cuts out everything but this central disc. Secondly, such long measurements invariably lead to fluctuations of the signal to noise ratio. So this was fixed by first selecting a small corner of the signal far away from the illumination and using it as a floor noise to average and subtract away from the full 2D signal. At each frame, the maximum intensity

was taken, and optionally a threshold which was defined as some percentage of the maximum intensity was used as a cutoff. This had a sharpening effect on the edges of the image when chosen carefully. The X-Y drifting was certainly the most complicated issue and requires its own dedicated explanation.

To take the signal of the central intensity peak as a function of time either stationary or with delay control, the center of the peak must be known and response will allow this portion to be followed even as the pointing direction drifts. It would not be enough to simply find the pixel position of the maximum intensity, because this position fluctuates much faster than the drift of the entire disc. This is because a small region of neighboring pixels near the middle have close to uniform intensity, even small fluctuations would cause the maximum to jump sporadically. Naturally this lead to the defining of the intensity center of mass. Because of the 2D nature of the image, a coordinate for the intensity center of mass across the x direction (columns) and along the y direction (rows) was found. The formulation for this appears as:

$$I_{cm,x} = \frac{1}{I_{total}} \sum_{i=0}^{N} I_i \cdot (x_i - x_0) \tag{3.17a}$$

$$I_{cm,y} = \frac{1}{I_{total}} \sum_{j=0}^{N} I_j \cdot (y_j - y_0) \tag{3.17b}$$

Here, I_{total} is the total intensity of the square selection having edge length of twice the user defined radius, and centered at the cursor point. I also used the constraint that $(x_i - x_0)^2 + (y_j - y_0)^2 \leq r_u^2$, where r_u is the parameter mentioned earlier in the section which defines a circular area encompassing the Airy disk. The coordinates (x_0, y_0) specify the center of the circle. The associated algorithm causes the center of this area to follow the intensity center of mass. A row element is designated with x_i, and a column is designated with y_j. The position of the intensity center of mass was found to be far less sensitive than the max intensity point described before. Once this position was found, the shift of the position was taken and added to the prior center so that if a drift occured, the center of image capture drifted just as much. The integrated intensity of the central peak was normalized by the

intensity of the full image to correct for both the laser intensity and the camera efficiency fluctuations. I would like to note that this was possible for us because the central peak of the Airy disk was far away from neighboring local maxima, and the spatial stability was good enough to prevent large drifting.

The resulting signal was then converted to the time delay between the two waves traveling in the interferometer. It can be seen that the time delay drifts considerably over the duration of the measurement. The peak-to-peak drift is about 300 as over two hours while the stability is of the order of 72 as rms. Such a temporal drift is significantly larger than the typical duration of the attosecond pulses ($\sim$ 100 as). The origins of the drift have not been clearly identified. But it is worth noting that the passive stability of our interferometer is quite comparable in magnitude to those of interferometers entirely placed under vacuum conditions [28, 75], which are known to be generally more stable. This indicates that possible air flows in the portion of our interferometer placed in atmospheric conditions may not be the main source of instability.

As a comparison, the long-term measurement of the stability of the Michelson interferometer without active stabilization is shown in Figure 3.6.b. The relative path length drift was deduced from the signal measured by the balanced homodyne detection system. As expected, the temporal drift is significantly better than that of the Mach-Zehnder interferometer. The peak-to-peak drift is of the order of 100 as over two hours while the stability is about 26 as rms. We have observed that the drift is mainly generated by temperature fluctuations in the laboratory resulting from the cooling/heating cycles of the air conditioning unit. For most of the attosecond pump-probe experiments, which are performed with a time step of the order of 100 to 200 as, such a drift would not significantly decrease the temporal resolution of the measurement. Nevertheless, to achieve the highest level of stability in the Mach-Zehnder interferometer, an active stabilization of the Michelson interferometer is necessary.

The long-term measurement of the relative path length drift of the Mach-Zehnder interferometer when both interferometers are actively stabilized is shown in Figure

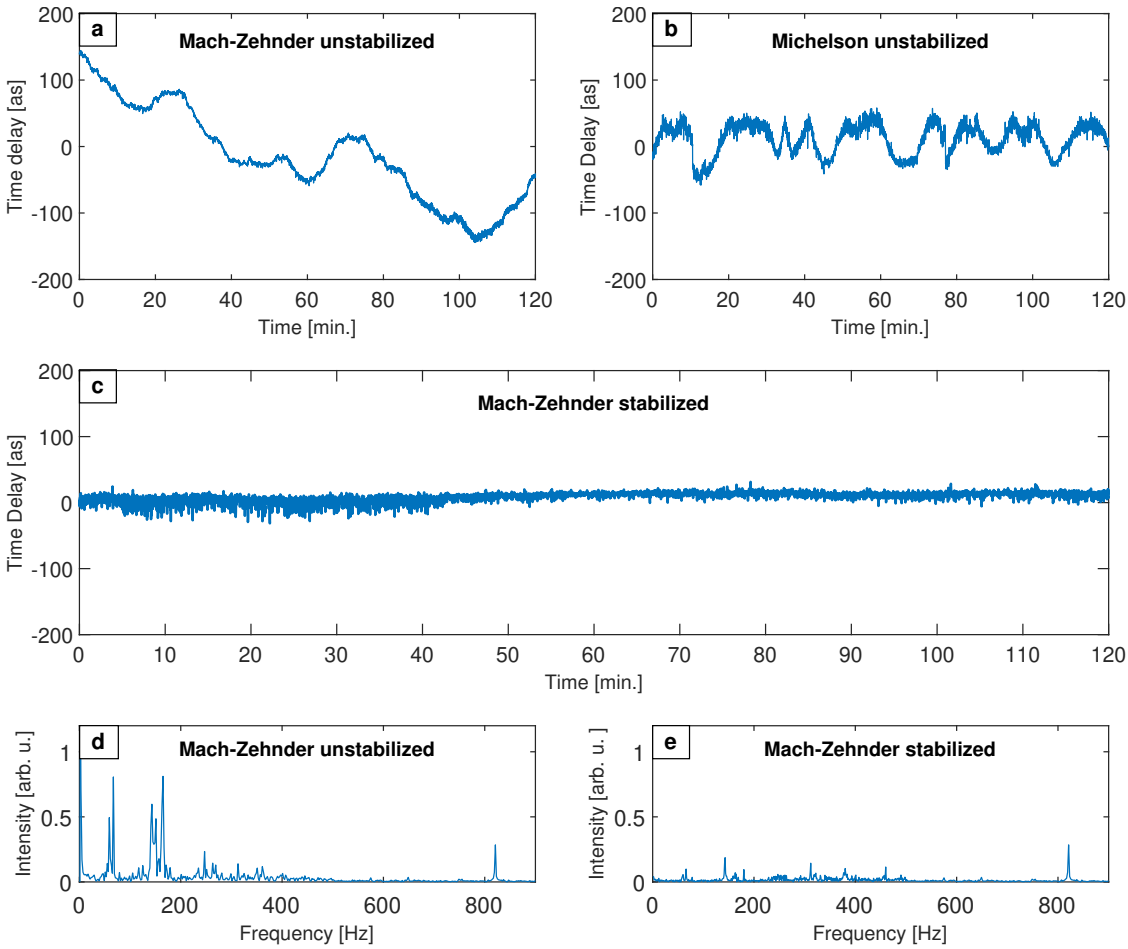

Figure 3.6: Relative path length drift in the Mach-Zehnder (a) and Michelson (b) interferometers without active stabilization and long-term stability of the Mach-Zehnder interferometer when both interferometers are actively stabilized (c). Spectral composition of the short-term stability of the interferometer without (d) and with (e) active stabilization. The arbitrary units in both (d) and (e) are normalized to the DC component in (d) so that we can compare the data in these subfigures. The constant height of the peak at 820 Hz (turbopumps, outside the PI or filter response) indicates this use of arbitrary units is appropriate.

3.6.c. A stability of 11 as rms is achieved over a period of 2 hours. Such a level of stability is somewhat higher than those measured in similar setups [27, 28, 75] and is very close to those achievable with collinear attosecond setups [29].

To identify the limiting factors for the attainable stability, a short-term measurement of the interferometer stability was performed using a photodiode in place of the CMOS camera. Figures 3.6.e and 3.6.d show the spectral composition of the short-term stability with and without active stabilization of the interferometer, respectively. The spectrum corresponding to the unstabilized interferometer reveals

several sources of vibration in our system. The region below 400 Hz is mainly dominated by vibrations in the building (0-200 Hz) and additional mechanical resonances of the experimental setup (200-400 Hz). On the other hand, the well-defined vibration peak located at 820 Hz is generated by the turbo-molecular pumps. With active stabilization, it can be seen that vibrations below 300 Hz have been almost fully canceled out, which suggests that the attainable stability is mainly limited by vibrations generated by the turbo-pumps.

3.3.5 Time Delay Control

The capability of the system to accurately control the time delay between two beams traveling in the interferometer is demonstrated in Figure 3.7. The time delay was deduced from the interference pattern produced by the 532-nm CW laser using the method described previously. Figure 3.7.a shows the signal measured with the BOR as the angle of the Evans' phase shifter is changed with angular rotations corresponding to steps in time. I already showed that a rotation in θ in the Evans phase-shifter causes a change in phase of $4\theta + \pi$. This means that the angular step size (difference) is 4θ. A full rotation of 360° would cause a change by 4 cycles. In terms of the wavelength in nanometers, for our green light reference laser a 360° rotation causes 2128 nm of travelled distance, or four times the period of the light, $7,093.\bar{3}$as. We used steps of 20 as (1°) over a range of 30 fs (1500°).

The signal displayed a sinusoidal behavior, but additionally the phase itself appeared to oscillate giving the signal a longitudinal modulation with delay. This phase oscillation artifact was periodic with what seemed to be every four cycles, which was every full rotation of the half-wave plate. Since it is already a known fact that the faces of optical elements are not parallel, but have a wedge shape, a systematic error was realized for our situation. Because our beam cannot be perfectly centered on the HWP, the wedge shape is experienced by the waves as a changing thickness with time. In performing a curve fit for our signal I added a cosine term to the phase to make room for this correction. Additionally, the envelope of the sinusoid displayed a modulating envelope. The upper and lower

envelopes of the sinusoid were found using the peaks within intervals having length of 50 samples each. The position of the middle of the envelope is found and used to position the signal middle to zero. Then, by dividing by half the envelope width, the signal is normalized between -1 and 1. The equation was given the form

$$f(\theta) = C_1 \cos\left(\frac{2\pi(\theta - C_3)}{C_2} + C_4 \cos\left(\frac{2\pi(\theta - C_6)}{C_5}\right)\right) + C_7. \tag{3.18}$$

Because the signal was a cosine that was normalized with the envelope, C_1 was equal to one and the amplitude offset term C_7 was equal to zero. The argument inside has two phase constants, C_3 and C_6. The terms for the period of the cosine C_2 and as well as the one for the longitudinal oscillation C_5 caused by the HWP were 1/4 the period of the 532-nm reference laser and the full period respectively. The signal exhibits a remarkable cosine-wave shape, which indicates that the time delay between the two waves is accurately controlled. The level of accuracy in controlling the delay is better observed in Figure 3.7.b where the time delay deduced from the modulated signal is plotted as a function of the phase shifter's angle. As can be seen in the figure, the linear relationship between the time delay and the phase shifter's angle is quite strong. The deviation from a perfect linear relationship mostly comes from the error in the time delay measurement around the maxima and minima of the modulated signal, where the error becomes comparable to the step size, and from the instability in the interferometer. As the statistical distribution of the delay steps shows in the subplot of Figure 3.7.b, the time delay is controlled to within 10 as, which corresponds to the level of stability of the interferometer. The distribution of step sizes was fitted with a Lorentzian function, and the deviation from the expected value is seen to stay neatly within the bounds of its full width at half maximum.

3.3.6 Application for Attosecond Pump-Probe Measurements

To test the level of performance of the stabilization system for attosecond pump/probe measurements, it was used to drive a RABBITT (Reconstruction of Attosecond Beating by Interference of Two-photon Transitions) experiment [7, 18], where an attosecond pulse train (APT) made of odd-order harmonics is used to ionize

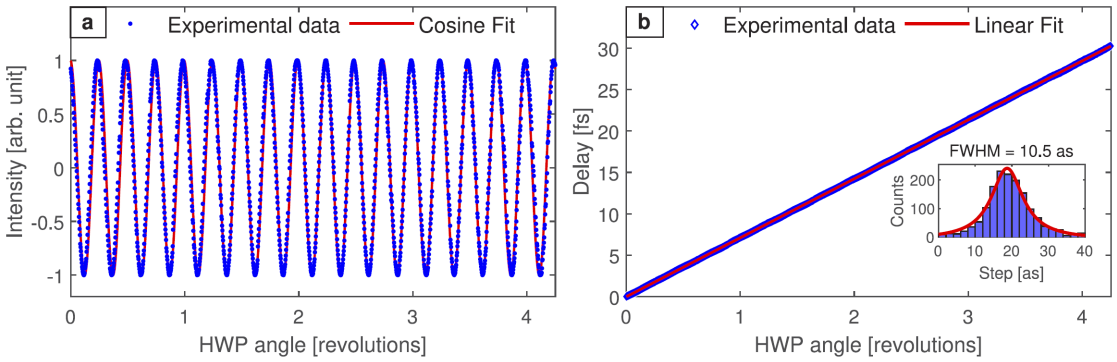

Figure 3.7: Control of the time delay between two 532-nm waves traveling in the interferometer: Interference signal captured by the photo-detector (a) and time delay between the two waves (b) as a function of the angle of the Evans' phase shifter. The subplot in (b) displays the statistical distribution of the delay steps deduced from the interference signal.

an atomic target in the presence of a weak IR field. In such an experiment, a spectrogram is formed by measuring the photoelectron spectra as a function of the time delay between the APT and the IR field. The photoelectron spectra exhibit peaks at photoelectron energies corresponding to one-photon absorption of the odd harmonics, and located in between, sideband peaks resulting from two- photon transitions (absorption of one XUV photon plus absorption or emission of one IR photon). Two different quantum paths involving two consecutive harmonics contribute to the same sideband quantum state, and thus interfere. As a consequence, the intensity of each sideband peak oscillates with the time delay between the APT and the IR field at twice the frequency of the IR field, as predicted by second-order perturbation theory [81]:

$$I_{SB} \propto \cos(2\omega_{IR}\tau + \phi_{spectral} + \phi_{atomic}). \tag{3.19}$$

where ω_{IR} is the frequency of the IR field, τ is the time delay between the APT and IR field, and $\phi_{spectral}$ and ϕ_{atomic} are the relative spectral phase between two consecutive harmonics, and the atomic phase of the photoionization process, respectively.

The experiment was performed with the setup described in section 2. Attosecond pulse trains made of odd harmonics of the fundamental 800- nm field were generated in argon via high harmonic generation. The pulse trains were then filtered to

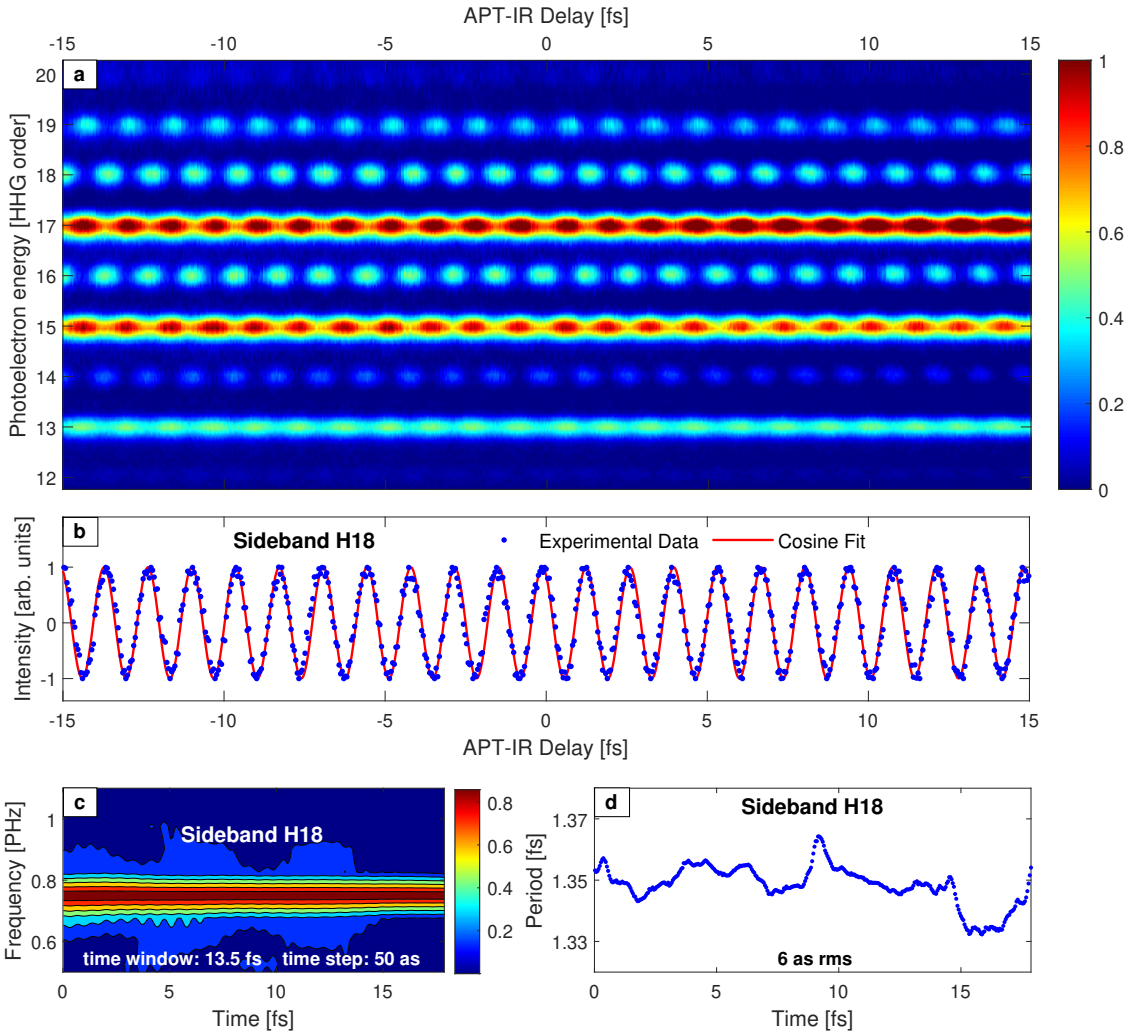

Figure 3.8: RABBITT experiment in argon with 50-as delay step. (a) Photoelectron energy spectra as a function of the time delay between the APT composed of odd harmonics and the IR field. The colorbar measures electron counts with 1 being the higher count intensity. (b) Envelope-normalized intensity of sideband H18 (formed by harmonics 17th and 19th) as a function of the time delay. (c) Short-time Fourier transform of the H18-sideband intensity modulation (13.5-fs window, 50-as time step). (d) H18-sideband period deduced from the frequency measured in (c) as a function of time.

remove harmonics below the 11th order and finally focused into an effusive gas jet of argon. The photoelectron energy spectra were measured with a velocity-map imaging system [57] and reconstructed using the DAVIS inversion procedure [62]. A typical spectrogram (measured over a period of 1.5 hours) is shown in Figure 3.8.a. The delay between the APT and IR field was scanned over 30 fs with 50-as time steps. At each delay, the photoelectron energy spectrum was recorded by collecting photoelectrons produced by roughly 10^5 pulse trains. The envelope-normalized

modulation of the peak intensity of sideband H18 as a function of the delay is plotted in Figure 3.8.b. Except for small deviations due to statistical fluctuations in the measurement, the modulation exhibits a clear cosine-wave shape, as described by Equation 3.19. The period of the oscillation is about 1.35 fs, which corresponds to half the period of the 800-nm IR field.

The short-time Fourier transform (STFT) of the H18-sideband intensity modulation is displayed in Figure 3.8.c. The STFT of $S(x(t))$ was calculated by sliding an analysis window of length 13.5 fs over the signal at steps of 50 as and computing the discrete Fourier transform of each window segment. An overlap is specified so that signal attenuation at the window edges is compensated. The signal was expected to remain close to the 1.35-fs half-period, and the STFT reveals that the periodicity of the modulation is remarkably constant over the full 30-fs delay range. This is further demonstrated in Figure 3.8.d where the fluctuation of the sideband period deduced from the STFT analysis is represented as a function of time. It can be seen that the peak-to-peak fluctuation of the period is about 30 as over the duration of the measurement (1.5 hours) while the standard deviation is about 6 as, which demonstrates the capability of the stabilization system to accurately stabilize and control the time delay between the APT and IR field. This result could in principle depend on the time window length of the STFT, but we have chosen window which is so large (1,350 as) in comparison to the delay step (50 as) that we assume an error contribution from this is negligible.

3.4 Conclusion

In this work, we have developed a stabilization system for attosecond pump-probe setups based on a Mach-Zehnder configuration. The system uses a CW laser propagating coaxially with the pump and probe beams in the interferometer. At the exit, the CW beams are recombined collinearly to produce a strong interference pattern allowing for a precise measurement of their relative phase. The stabilization of the interferometer is achieved with a standalone feedback controller that adjusts the length of one arm of the interferometer to maintain a constant relative phase

between the CW waves. The maximum stabilization rate is set by the resonance frequency of the piezoelectric stage used. With such a system, we have shown that the relative path length of our 2m-long interferometer can be stabilized within 3 nm over several hours, which corresponds to a timing jitter between the pump and probe beams as low as 10 as rms (subplot of Figure 3.7.b). The system is easy to operate and only requires a few minutes to set up before any pump-probe experiments. Due to its long-term stability, the system is well-suited for low-count experiments that require data collection over an extended period of time.

"Most phenomena we are familiar with involve such tremendous numbers of electrons that it's hard for our poor minds to follow that complexity. In such situations, we can use the theory to figure roughly what ought to happen... if we arrange in the laboratory an experiment involving just a few electrons in simple circumstances, then we can calculate what might happen very accurately, and we can measure it very accurately too."

— Richard Feynman (Lecture on QED)

4

Electron Choreography at the Attosecond Timescale

Contents

In this work, we report on coherent control of electron dynamics in atoms *via* attosecond pulse-shaping. We show that the photoelectron emission from argon gas produced by absorption of an attosecond pulse train (APT) made of odd and even harmonics can be manipulated along the direction of polarization of the light by tuning the spectral components (amplitude and phase) of the pulse. In addition,

we show that APTs produced with a two-color (400- plus 800-nm) femtosecond driving field exhibit high temporal tunabilty, which is optimized for an intensity ratio between the two colors in the range of 0.1 to 5%.

4.1 Theoretical Models for the Strong Field Approximation for HHG

The following is a theoretical development for the SFA theory which we use as the foundation to model our harmonic spectrum. The development comes from a tutorial by Le et. al. [15]. Another classic reference that can be used is Fundamentals of Attosecond Optics [13]. This treatment of SFA goes into more depth than the one in Chapter 1. A thorough physical model for SFA is developed first, followed by simplifications with the saddlepoint approximation. Such simplifications allows one to go from having to compute taxing numerical solutions to an accurate and much simpler analytical one. Atomic units are used throughout this section.

4.1.1 The Lewenstein Model

The SFA as we know it today was refined by Lewenstein and L'Huiller [11]. Keldysh [14] developed an early version of this theory much earlier for photoionization by intense laser fields, and Reiss [82] and Faisal [83] brought subsequent improvements later. What follows is a summary of the theory which is given in great detail by [15]. We use atomic units where $\hbar = m_e = e = a_0 = 1$, and a_0 is the Bohr radius. If we begin by considering the system where an atom or ion is immersed in an intense laser field, and the system is approximated by the SAE case, the Schrödinger equation is

$$i\frac{\partial}{\partial t}\left|\Psi(\boldsymbol{r},t)\right\rangle = \left(-\frac{1}{2}\nabla^2 + V(r) + \boldsymbol{r}\cdot\boldsymbol{E}(t)\right)\left|\Psi(\boldsymbol{r},t)\right\rangle, \tag{4.1}$$

where $V(r) = -1/r$ is the coulombic potential, and $\boldsymbol{E}(t)$ is the laser field. The Hamiltonian can be shown as a contribution from a Hydrogen-like system as well as one from the laser interaction.

$$H(t) = H_0 + \boldsymbol{r}\cdot\boldsymbol{E}(t). \tag{4.2}$$

The Hydrogenic Hamiltonian is

$$H_0 = -\frac{1}{2}\nabla^2 + V(r). \tag{4.3}$$

It is used to define the ground bound state with energy $-I_p$

$$H_0 \left|\psi_g\right\rangle = -I_p \left|\psi_g\right\rangle, \tag{4.4}$$

as well as excited bound states with energy E_e

$$H_0 \left|\psi_e\right\rangle = E_e \left|\psi_e\right\rangle. \tag{4.5}$$

Additionally, the continuum electron with momentum $\boldsymbol{k}$ is described with

$$H_0 \left|\boldsymbol{k}\right\rangle = \frac{k^2}{2} \left|\boldsymbol{k}\right\rangle. \tag{4.6}$$

Next, consider the Laser intensity to be high enough for the Keldysh [14] parameter to behave as $\gamma < 1$, but low enough to not deplete the ground state. Also include the assumption for which the tunnel ionization delivers the electron directly to the continuum, bypassing intermediate states and resonances. This allows the wavefunction to be shown as an expansion of ground state and its trajectory in the continuum during step 2 of the TSM

$$\left|\Psi(t)\right\rangle = e^{i(I_p t)} \left(\left|\psi_g\right\rangle + \int d^3k b(\boldsymbol{k}, t) \left|k\right\rangle\right). \tag{4.7}$$

As described in chapter 1, the dipole moment is an essential element to calculate the HHG spectrum. The time-dependent dipole moment is

$$D_i(t) = \boldsymbol{e}_i \cdot \boldsymbol{D}(t) = \boldsymbol{e}_i \cdot \left\langle \Psi(t) | \boldsymbol{r} | \Psi(t) \right\rangle. \tag{4.8}$$

After this calculation, the power spectrum obtained by the Fourier transform represents the HHG yield. In terms of the wavefunction from Equation 4.7, the dipole moment is

$$\boldsymbol{D}(t) = \int d^3k \left\langle \psi_g | \boldsymbol{r} | \boldsymbol{k} \right\rangle b(\boldsymbol{k}, t) + c.c. \tag{4.9}$$

To develop a more intuitive version of this requires the introduction of the time evolution operators. The first one for the total Hamiltonian, U(t,t'), where t is the later time and t' is the initial time, is defined by

$$|\Psi(t)\rangle = U(t,-\infty)\,|\Psi(-\infty)\rangle = U(t,-\infty)\,|\psi_g\rangle\,. \tag{4.10}$$

Another operator for the absence of the laser is

$$U_0(t,-\infty)\,|\psi_g\rangle = e^{iI_p t}\,|\psi_g\rangle\,. \tag{4.11}$$

The amplitude $\boldsymbol{b}(\boldsymbol{k},t)$ from Equation 4.9 can be rewritten in terms of the time evolution as

$$b(\boldsymbol{k},t) = e^{-iI_p t}\,\langle \boldsymbol{k}|U_0(t,-\infty)|\psi_g\rangle\,. \tag{4.12}$$

When this equation is substituted into Equation 4.9, we get

$$\begin{aligned}\boldsymbol{D}(t) &= \int d^3k e^{-iI_p t}\,\langle\psi_g|\boldsymbol{r}|\boldsymbol{k}\rangle\;\langle\boldsymbol{k}|U_0(t,-\infty)|\psi_g\rangle + c.c.\\ &= e^{-iI_p t}\,\langle\psi_g|\boldsymbol{r}U_0(t,-\infty)|\psi_g\rangle + c.c.\end{aligned} \tag{4.13}$$

S-matrix theory can be used to re-express this as

$$\begin{aligned}\boldsymbol{D}(t) &= e^{-iI_p t}\left(-i\int dt'\,\langle\psi_g|\boldsymbol{r}U(t,t')\boldsymbol{r}\cdot\boldsymbol{E}(t')U_0(t,-\infty)|\psi_g\rangle\right) + c.c.\\ &= e^{-iI_p t}\left(-i\int dt'\,\langle\psi_g|\boldsymbol{r}U(t,t')\boldsymbol{r}\cdot\boldsymbol{E}(t')e^{-iI_p t'}|\psi_g\rangle\right) + c.c\end{aligned} \tag{4.14}$$

In contrast to Equation 4.2, the Hamiltonian can also be shown to portray the electron in the laser immersed continuum with a separate contribution by the ionic potential as follows:

$$H(t) = H_F(t) + V(\boldsymbol{r}) \tag{4.15}$$

The Hamiltonian for the electron in the field is

$$H_F(t) = -\frac{1}{2}\nabla^2 + V(\boldsymbol{r})\cdot\boldsymbol{E}(t). \tag{4.16}$$

The Volkov states which are the eigenstates for H_F, in the length gauge, have been found as

$$|\chi_p(t)\rangle = |\boldsymbol{p}+\boldsymbol{A}(t)\rangle\, e^{-i\int_{-\infty}^{t} dt''\frac{1}{2}[\boldsymbol{p}+\boldsymbol{A}(t)}]^2. \tag{4.17}$$

In this equation, $|p\rangle$ and $\boldsymbol{A}(t)$ are the plane wave solution and vector potential respectively. The time evolution operator, U_F(t,t') for H_F is defined by

$$U_F(t,t') = \int d^3p \, |\chi_p(t)\rangle \, \langle \chi_p(t')| \, . \tag{4.18}$$

And if the potential $V(\boldsymbol{r})$ is considered small, the following approximation can be made for the total Hamiltonian time evolution operator

$$U(t,t') = U_F(t,t'). \tag{4.19}$$

The dipole moment can now be show to be

$$\begin{aligned} \boldsymbol{D}(t) = -i \int_{-\infty}^{t} dt' \int d^3p e^{-iI_p t} \, \langle \psi_g | \boldsymbol{r} | \boldsymbol{p} + \boldsymbol{A}(t) \rangle \\ \times \boldsymbol{E}(t') \cdot \, \langle \boldsymbol{p} + \boldsymbol{A}(t) | \boldsymbol{r} | \psi_g \rangle \, e^{iI_p t'} e^{-i \int_t^{-\infty} dt'' \frac{1}{2}[\boldsymbol{p}+\boldsymbol{A}(t)]^2} + c.c. \end{aligned} \tag{4.20}$$

A more compact form can be used in terms of dipole matrix elements

$$\boldsymbol{D}(t) = -i \int_{-\infty}^{t} dt' \int d^3p d^*(\boldsymbol{p} + \boldsymbol{A}(t)) \boldsymbol{E}(t') d(\boldsymbol{p} + \boldsymbol{A}(t')) e^{-iS(\boldsymbol{p},t,t')} + c.c. \tag{4.21}$$

where $d(\boldsymbol{p}) = \langle \boldsymbol{p} | \boldsymbol{r} | \psi_g \rangle$, and the phase term $S(\boldsymbol{p}, t, t')$ is

$$S(t) = \int_{t'}^{t} dt'' \left(\frac{1}{2} [\boldsymbol{p} + \boldsymbol{A}(t'')]^2 + I_p \right). \tag{4.22}$$

4.1.2 Saddle-point Approximation for Linear Polarization

Up to this point, numerical solutions for this theory of SFA generates very accurate results. But, in order to have a simpler, analytical solution, further work is required. The greatest simplification can be brought about by means of the saddle-point method. Although this can be generalized for arbitrary dimensions and laser polarization, what follows is a treatment for linear polarization. This in turn constrains the system to one dimension. Before applying the saddle-point method, a general demonstration for a relevant case will be shown. First, the following integral portrays those like Equations 4.20 and 4.21.

$$I = \int_{-\infty}^{\infty} d\omega E(\omega) e^{if(\omega)} \tag{4.23}$$

Here, the term $E(\omega)$ varies slowly while $e^{if(\omega)}$ is much faster. The integral is dominated by the slowly varying term near the saddle-points ω_s that come from the first derivative test,

$$f'(\omega_s) = 0. \tag{4.24}$$

Because there are, in general, a set of saddle-points, the integral is reduced to a sum of the contributions by each one. This is expressed as

$$I \approx \sum_s \sqrt{\frac{2\pi i}{f''(\omega_s)}} E(\omega_s) e^{if(\omega_s)}. \tag{4.25}$$

This eliminates one of the integrals in Equation 4.20 to greatly simplify things to

$$\begin{aligned} D_x(t) = -i \int_{-\infty}^{t} dt' \left(\frac{-2\pi i}{t - t' - i\epsilon}\right)^{3/2} d_x^*(p_s + A(t)) \\ \times d_x(p_s + A(t')) E(t') e^{-iS(p_s,t,t')} + c.c. \end{aligned} \tag{4.26}$$

Although this is a major step in reducing the complexity, there is hardly any loss in the level of accuracy. When the full numerical SFA model is used as a benchmark, the saddle-point approach is in remarkable agreement.

4.1.3 Quantum Orbits

Before, it was said that the HHG yield is obtained by taking the Fourier transform of the dipole. More specifically this is

$$P(\omega) \propto \omega^4 |D_x(\omega)|^2. \tag{4.27}$$

Where the Fourier transform is

$$D_x(\omega) = \int_{-\infty}^{\infty} D_x(t) e^{i\omega t} dt = D_x^{(+)}(\omega) + [D_x^{(+)}(-\omega)]^*, \tag{4.28}$$

where

$$\begin{aligned} D_x^{(+)}(\omega) = \int_{-\infty}^{\infty} dt \int_{-\infty}^{t} dt' \left(\frac{-2\pi i}{t - t' - i\epsilon}\right)^{3/2} d_x^*(p_s + A(t)) \\ \times d_x(p_s + A(t')) E(t') e^{-i\Theta(p_s,t,t')}, \end{aligned} \tag{4.29}$$

where ϵ is an artifact to help avoid singularity issues. In Equation 4.29 we have

$$\Theta(p_s, t, t') = S(p_s, t, t') - \omega t, \tag{4.30}$$

$$S(p_s, t, t') = \int_t^{t'} dt'' \left(\frac{1}{2}[p_s + A(t'')]^2 + I_p \right), \tag{4.31}$$

and saddle-points

$$p_s = -\frac{1}{t - t'} \int_{t'}^{t'} A(t'')dt''. \tag{4.32}$$

If the saddle-point method is applied to the above equations then we obtain

$$\frac{1}{2}[p_s + A(t')]^2 = I_p, \tag{4.33}$$

and

$$\frac{1}{2}[p_s + A(t)]^2 = \omega - I_p. \tag{4.34}$$

Equations 4.33 and 4.34 have solutions for a set of saddle-point times (t_s, t'_s). The one dimensional dipole is approximately the classical counterpart of the Fourier transform in Equation 4.28,

$$D_x(\omega) \approx D_x^{(+)}(\omega) = \sum_s D_{x,s}(\omega), \tag{4.35}$$

where $D_{x,s(\omega)}$ is the one dimensional dipole moment for a given quantum orbit.

$$\begin{aligned} D_{x,s}(\omega) = -i\sqrt{\frac{(2\pi i)^2}{\det(S'')}} \left(\frac{-2\pi i}{t_s - t'_s} \right)^{3/2} d_x^*(p_s + A(t_s)) \\ \times d_x(p_s + A(t'_s))E(t'_s)e^{-i\Theta(p_s, t_s, t'_s)} \end{aligned} \tag{4.36}$$

The matrix embedded within this equation is

$$S'' = \left(\begin{array}{cc} \dfrac{\partial^2 S(p_s, t, t')}{\partial t^2} & \dfrac{\partial^2 S(p_s, t, t')}{\partial t \partial t'} \\ \dfrac{\partial^2 S(p_s, t, t')}{\partial t' \partial t} & \dfrac{\partial^2 S(p_s, t, t')}{\partial t'^2} \end{array} \right)_{t=t_s, t'=t'_s}. \tag{4.37}$$

The compact version of the dipole equation now becomes

$$\begin{aligned} D_x(\omega) &= d_x^*(\sqrt{2(\omega - I_p)}) d_x(i\sqrt{2I_p}) \\ &\times \sum_s \frac{2\pi\varepsilon\varepsilon'}{\sqrt{\det(S'')}} \left(\frac{-2\pi i}{t_s - t'_s} \right)^{3/2} \\ &= d_x^*(\sqrt{2(\omega - I_p)}) w(\omega), \end{aligned} \tag{4.38}$$

where ε_s and ε_s' are factors that can have a value ± 1 for the sign of the electron momentum.

4.1.4 Quantum orbit theory with a monochromatic laser

Solutions to Equations 4.33 and 4.34 represent the times for the electron trajectories as explained in the TSM. Another name for this excursion is quantum orbit. This can be found for the general case of three dimensions, but if the laser is chosen to be a linearly polarized, monochromatic cosine wave, a simple analytic solution results in one dimension. The vector potential is easily obtained

$$A(t) = -\int E_0 \cos(\omega_L t')dt' = -\frac{E_0}{\omega_L}\sin(\omega_L t). \tag{4.39}$$

Immediately following, we find the saddle-point for the momentum which comes by substitution of Equation 4.39 into 4.32

$$p_s = \frac{1}{t-t'}\int_{t'}^{t} A(t'')dt'' = -\frac{E_0}{\omega_L}\left(\frac{\cos(\omega_L t) - \cos(\omega_L t')}{\omega_L t - \omega_L t'}\right). \tag{4.40}$$

After substituting Equations 4.39 and 4.40 into Equations 4.33, and 4.34, as well as using the relations $\omega_L t = \theta$ and $\omega_L t' = \theta'$ the born and recombination times can be obtained by solving both

$$\left(\frac{\cos\theta - \cos\theta'}{\theta - \theta'} + \sin\theta'\right)^2 = -\frac{I_p}{2U_p} = -\gamma^2, \tag{4.41}$$

and

$$\left(\frac{\cos\theta - \cos\theta'}{\theta - \theta'} + \sin\theta\right)^2 = \frac{\omega - I_p}{2U_p} = \frac{\tilde{\omega}}{2}, \tag{4.42}$$

where $U_p = E_0^2/4\omega_L^2$. Finally, the phase factor Θ is expressed in terms of these solutions, the ponderomotive energy, and the Keldysh parameter as

$$\begin{aligned}\Theta_s = &\frac{2U_p}{w_L}\left[\gamma^2 + \frac{1}{2} - \left(\frac{\cos\theta_s - \cos\theta_s'}{\theta_s - \theta_s'}\right)^2\right](\theta_s - \theta_s') \\ &- \left[\frac{2U_p}{w_L}\left(\sin(2\theta_s) - \sin(2\theta_s')\right) - \left(\frac{\tilde{\omega}}{2} + \gamma^2\right)\theta_s\right].\end{aligned} \tag{4.43}$$

We also considered a two-color case. We can rewrite Equations 4.39 to 4.42 by adding the second harmonic i.e. $2\omega_L$ beginning with

$$\begin{aligned}A(t) &= -\int E_0\left(\cos(\omega_L t') + r\cos(2\omega_L t' + \phi)\right)dt' \\ &= -\frac{E_0}{\omega_L}\left(\sin(\omega_L t) + \frac{r}{2}\sin(2\omega_L t + \phi)\right).\end{aligned} \tag{4.44}$$

In this equation, r is the ratio of the second harmonic field to the fundamental and ϕ is the phase between them. With this vector potential Equation 4.40 for the two-color case is

$$p_s = -\frac{E_0}{\omega_L}\left[\frac{\cos(\omega_L t) - \cos(\omega_L t')}{\omega_L t - \omega_L t'} + \frac{r}{4}\left(\frac{\cos(2\omega_L t + \phi) - \cos(2\omega_L t + \phi)}{\omega_L t - \omega_L t'}\right)\right]. \quad (4.45)$$

The saddlepoint equations become

$$\left(\frac{\cos\theta - \cos\theta'}{\theta - \theta'} + \sin\theta + \frac{r}{4}\left(\frac{\cos(2\theta + \phi) - \cos(2\theta + \phi)}{\theta - \theta'}\right) - \frac{r}{2}\sin(2\theta + \phi)\right)^2 = -\gamma^2 \quad (4.46)$$

$$\left(\frac{\cos\theta - \cos\theta'}{\theta - \theta'} + \sin\theta + \frac{r}{4}\left(\frac{\cos(2\theta + \phi) - \cos(2\theta + \phi)}{\theta - \theta'}\right) - \frac{r}{2}\sin(2\theta + \phi)\right)^2 = \frac{\tilde{\omega}}{2} \quad (4.47)$$

Now the only remaining issue is obtaining the dipole matrix element to use. If the ground state has a simple Hydrogenic behavior, the dipole matrix element is Gaussian in nature,

$$d_x(p) = \langle pe_x|x|\psi_g\rangle = i\left(\frac{1}{\pi a}\right)^{3/4}\frac{p}{a}e^{-p^2/2a}, \quad (4.48)$$

where $a = 0.8I_P$. So the dipole matrix element is related to the generation gas by its ionization potential. The Gaussian proves to be a suitable option, and allows us to obtain a solution at last.

4.2 Introduction

Coherent control of quantum phenomena in matter through its interaction with light is a fast-growing field in ultrafast science. It is driven primarily by the ultimate goal of controlling the complex dynamical properties of quantum systems at the heart of many scientific fields. Over the last four decades, femtosecond laser technology has led to remarkable advances in our ability to control the ultrafast femtosecond dynamics in a vast number of systems (from simple to complex molecular systems, clusters, nanostructures, ...) [84–87]. With the recent development of extreme

ultraviolet (XUV) light sources with attosecond duration, new capabilities emerge for controlling quantum dynamics in matter with an unprecedented level of precision down to the natural timescale of electron motion [7, 17].

Even though the first attosecond pulses were generated nearly two decades ago, their use for controlling electron dynamics in matter has been elusive so far. Attosecond control has been mostly achieved with pump/probe schemes where an attosecond-pump pulse triggers a given electronic process, and a phase-locked femtosecond-probe field is used to steer its dynamics. The system under scrutiny is thus controlled by varying the time delay between the two pulses. Such an approach has been successfully employed to manipulate benchmark systems such as the electronic charge distribution within a molecular target [88, 89] or the photoelectron emission from atoms [25, 26, 90]. Despite these impressive proofs-of-principle, attosecond control of quantum phenomena in matter is still in its infancy, though, mainly because attosecond pulse shaping techniques are still developing. Even though several schemes have already been reported to tailor the spectrum [91–100], the polarization [101–106], or the angular momentum [107] of these pulses, shaping their spectral phases for attosecond control, on the other hand, still remains a challenging endeavor for the attosecond community. Indeed, the low intensity of the attosecond pulses currently produced *via* high-harmonic generation (HHG) together with the high absorption rate of XUV radiation by most optical materials restrict the use of usual pulse shaping techniques (like chirped mirrors, ...) to manipulate the spectral phase of the pulses after generation.

An alternative approach consists of shaping the spectral phases of attosecond pulses directly during the generation process. Within the widely accepted three-step model describing attosecond pulse generation *via* high-harmonic generation (1-ionization, 2-propagation in the laser electric field, and 3-recombination), the spectral phases of the frequency components making up the pulse are directly related to the recombination times [108], which in turn are defined by the electron wavepacket trajectories (also referred to quantum orbits) in the driving laser field. By tailoring the temporal waveform of the femtosecond driving field, the quantum

orbits and the recombination times can then be tuned giving some control over the spectral phases of the APT.

Two-color femtosecond waveforms made of a fundamental field and its second harmonic have been proved to be very efficient to manipulate quantum orbits in the HHG process. The literature is rich with experimental and theoretical studies reporting the dependence of both the spectrum and the polarization of the resulting APT on the temporal profile of such synthetized waveforms [92–97, 100, 106, 109–111]. On the other hand, the dependence of the APT's spectral phases on the temporal profile of the two-color field still remains elusive, though. In this work, we show how these phases can be manipulated by varying the intensity ratio and the relative phase between the two components of the driving field. We show that the spectral phases exhibit high tunabilty for an intensity ratio between the two colors in the range of 0.1 to 5%. As an application for such a spectral pulse shaping technique, we report on a coherent control experiment where the photoelectron emission from atoms generated by tailored attosecond pulses is manipulated along the direction of polarization of the light by tuning the spectral phases of the APT.

4.3 Achievements in Coherent Control of Photoemission

Several foundational achievements in the territory of coherent control of photoemission have occurred in recent times. Developments in both novel experimental techniques and theoretical descriptions show evidence of steady advancement as the road is paved for more exciting capabilities for dynamic quantum control. And, likewise, the explanations for the phenomena observed have become increasingly refined and simplified.

Two experiments that show ways to control of photoemission have already been expressed in chapter 1 in section 1.3.3. Briefly, in the study led by Mauritsson [25], the attosecond streaking technique is used to drive photoemission dynamics. The SAP used as the probe first ionizes electrons into the continuum. Afterwards, a strong IR field produces a shifting of the energy which can be seen clearly in the

PAD. This results from a momentum transfer from the IR field that depends on the delay between the XUV and IR. In this technique, the authors created the circumstances to return the ionized electrons to the parent and scatter with the ionic core. These measurements demonstrate a high level of spatial resolution and offer this benefit to more complex systems with possibilities that can be realized by altering the frequency composition of the strong field that steers the dynamics of the laser. Also, Laurent et. al. found a way to direct the photoemission of a system excited with an APT composed of odd and even harmonics and probed with a weak IR field. The standard RABBITT uses a similar configuration with an APT of odd harmonics only, and the PAD is symmetric about the polarization axis. However, the presence of even harmonics produces additional channels leading to the same electron continuum energies. With these additional quantum paths, the mixture of parities in the final states leads to an asymmetric angular distribution. In this study, the asymmetry of the emissions were shown to be related to the relative phases of the consecutive odd and even harmonics. These studies represent the essence of photoemission control when the process is steered by the pump-probe delay. Recent works such as that reported by Cheng and this paper begin to turn studies toward a new direction.

Recent qualitative descriptions have extended propensity rules from one-photon ionization to laser-assisted ionization measurements. Before, it was the quantum selection rules that were mainly used to help predict the qualitative physics. The selection rules for electric dipole transitions tell us the most probable outcomes that come as a result of light-matter interaction. On the other hand, propensity rules tell us that an increase of angular momentum of the system is favored in these transactions. The underlying reasons for why the selection rules work can be shown mathematically as dipole transition that depends on the wave function parities being connected. Fano showed us that there is an inclination of the system to minimize the final momentum of a photoelectron, with definition $k(r) = \sqrt{2[E - V(r)]}$, using a mathematical argument as well. He demonstrated, through a briefing in 1985, that the rapidly oscillating terms (for higher final momentum) in the

transition matrix elements make small contributions compared to the smoother terms (lower final momentum). The origin of this behavior is that, while the final energy of the system is increased, the centrifugal term of the potential increases more when the angular momentum increases. This in turn minimizes the final momentum. This tool, referred to as Fano's propensity rule, presents itself as a powerful aid in determining the physics of light-matter transitions. Until recently it has been limited to the one-photon case.

In 2019, Busto et. al. showed Fano's propensity rule can be extended to laser-assisted photoionization [90]. By doing this, the propensity rules offer a simplified viewpoint for the delay dependence of the photoelectron angular distributions that occur in RABBITT measurements. The study analyzed matrix elements for transitions where an XUV photon is absorbed having a frequency $\omega(s \mp 1)$, followed by absorption or emission of an IR photon of frequency ω. With atomic units and electric field amplitudes of the XUV and IR fields set to one, the matrix elements have the form

$$M^{(\pm)}_{\lambda Lm} = \lim_{\epsilon \to 0^+} \sum\!\!\!\!\!\!\int_p \frac{\langle \psi_q | \, z \, | \psi_p \rangle \, \langle \psi_p | \, z + \delta z \, | \psi_a \rangle}{\varepsilon_a - \varepsilon_p + \omega(s \mp 1) + i\epsilon}. \tag{4.49}$$

In the above equation, the initial state wavefunction and energy is designated with a subscript a, the intermediate state is designated with p and angular momentum λ and the final state is specified with subscript q. A sum-integral covers all possible intermediate bound and continuum states, and the ϵ is a small quantity to prevent singularity issues. The absorption/emission of a fundamental IR photon results in change of angular momentum ± 1 which is reflected in the notation as $L = \lambda \pm 1$. As seen in Figure 4.1.a, in a comparison of absorption as a ratio of increased angular momentum l to decreased l, transitions have a greater inclination toward increasing angular momentum. Additionally, in figure 4.1b it is show that in the case of angular momentum increase for absorption and emission, absorption is favored. Figure 4.1.c shows what can be understood as the time reversal case of Figure 4.1.b - a decrease in angular momentum for emission is favored over absorption and a decrease of angular momentum. This study succeeded to show

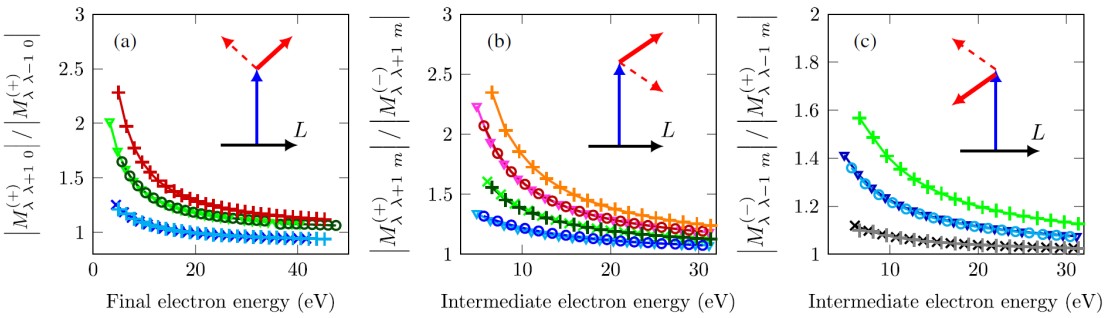

Figure 4.1: Illustrations of Fano's propensity rules. In Figure 4.1a, a comparison of absorption as a ratio of increased angular momentum l to decreased l shows increasing angular momentum is favored. In Figure 4.1.b the case of angular momentum increase for absorption and emission is displayed, indicating absorption is preferred. Figure 4.1.c shows what can be understood as the time reversal case of Figure 4.1.b. Figure adapted from [90]

in a benchmark system of the PAD of Argon that these rules can be verified for lower photoelectron kinetic energies. This study's value comes from the fact that the conclusions are valid even when multiple incoherent channels are present. Such an understanding of the angle-resolved dynamics is essential in coherent control experiments. Most existing techniques for controlling photoemission use methods involving a pump/probe type scheme like those mentioned earlier in this section which implement attosecond streaking or RABBITT. However, the recent method by Cheng et. al. does not require delay control of the probe field to steer the dynamics. In this work, it is the carrier-envelope phase (CEP) which is controlled to drive the process. A bending of the rules for the photoelectric effect is demonstrated as conditions for a time-slit interference are produced in the experiment. Two measurements are carried out that have resemblances to two-slit interference, and three-slit interference. Their XUV APTs are generated by an IR field with variable CEP. When the CEP of an IR field is $\pi/2$, this leads to an even number of pulses in the APT - the authors produce two i.e. the two-slit condition. On the other hand, when the CEP is 0, this leads to an odd number of pulses in the APT - the authors produce three i.e. the three-slit condition.

In the two-slit experiment, Helium gas is ionized by a train of three attosecond pulses dressed by a weak IR field. The EWPs interfere with each other, and

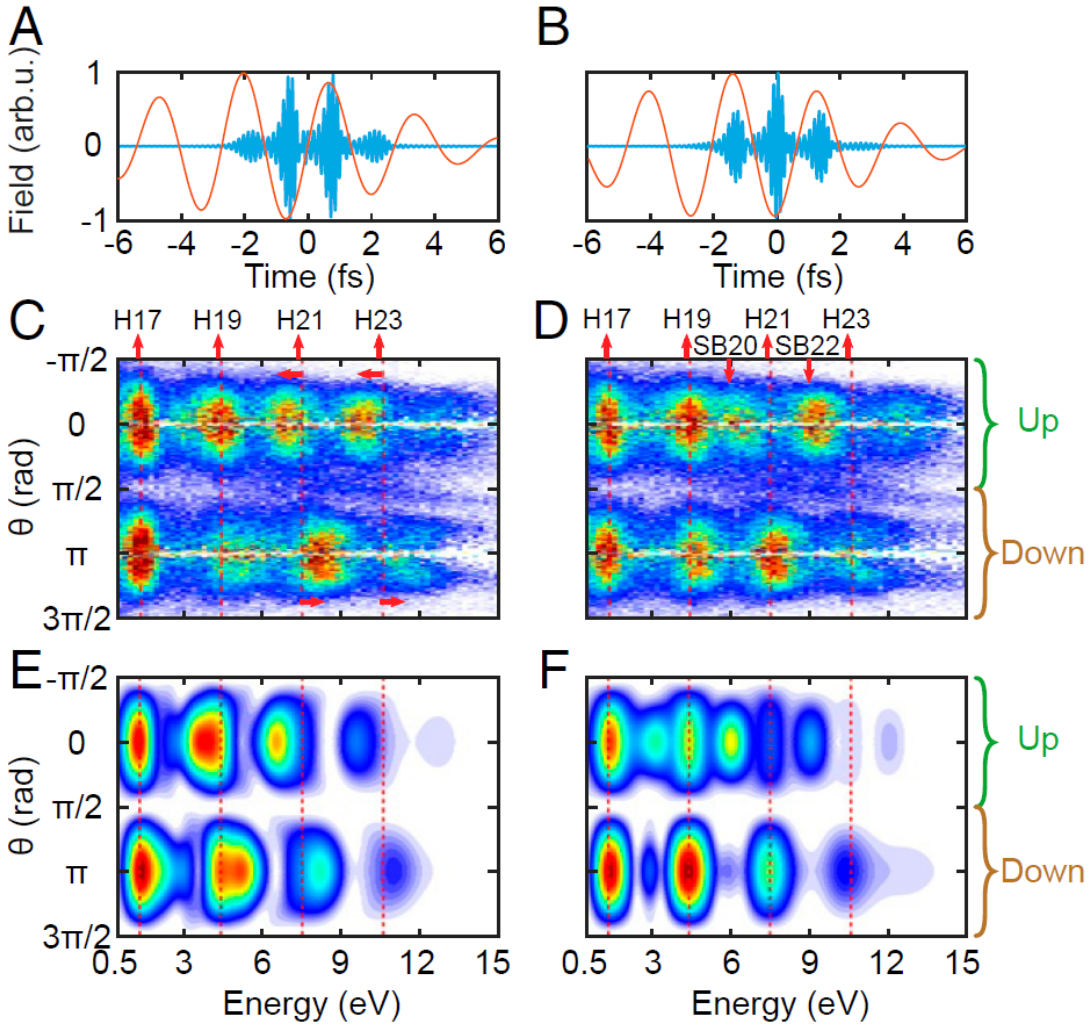

Figure 4.2: Photoemission control with the attosecond time-slit methodology. The nature of the overlapping APTs and their IR field is shown in the two-slit and three-slit compositions in Figures 4.2.a and 4.2.b respectively. Experimental results showing the shifting of the peaks in energy for the two and three-slit cases are shown in 4.2.c and 4.2.d. Finally, results of the theoretical models are shown below. Figure adapted from [112]

the presence of the IR field does not produce sidebands, but rather causes a shifting of the photoelectron peaks. In the three-slit experiment, the first and third attosecond pulses interfere with each other and peaks appear for all harmonic energies in accordance. Sidebands are present in this experiment, and the interference of the middle attosecond pulse with the other two results in an increasing or decreasing behavior of the sidebands. Such behaviour is consistent with descriptions that can explain the phenomena with an analogous time-slit picture. These new

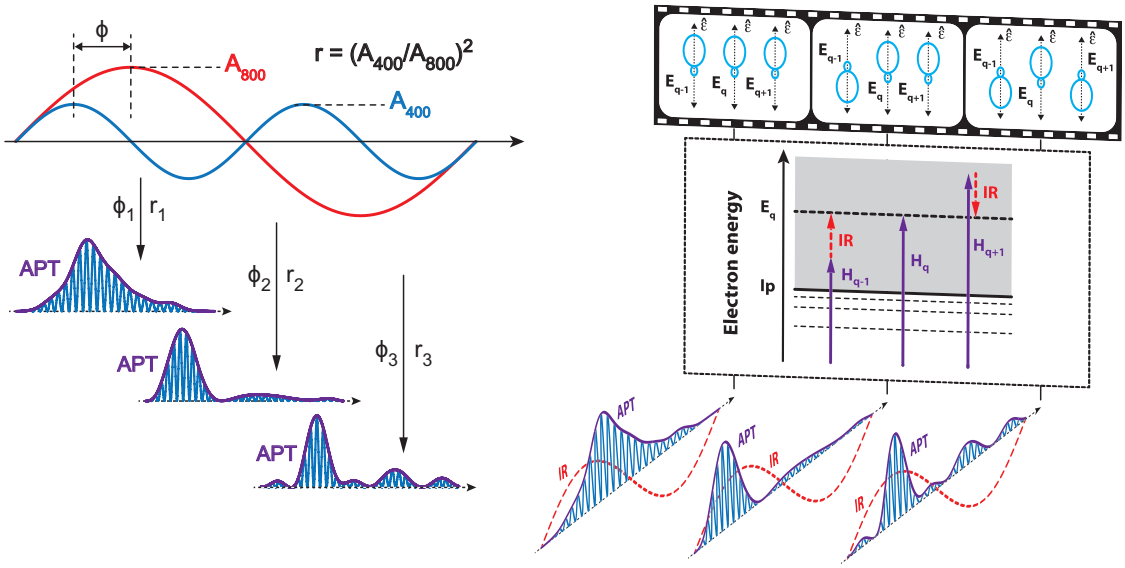

Figure 4.3: Principle of the experiment: APTs with tailored temporal profile are generated with a two-color femtosecond field (800+400nm) by varying both the intensity ratio r and the relative phase ϕ between its two components. The pulses are then used to ionize argon gas in the presence of a relatively weak IR field ($\sim 10^{11}$ W/cm^2). Three quantum paths contribute to the generation of an electron wavepacket at a given energy E_q. These interfere, leading to an energy-dependent asymmetric electron emission along the direction of polarization of the light ($\hat{\varepsilon}$) that is controlled by tuning the temporal profile of the APT. Figure adapted from [50].

experiments provide a way to handle the photoemission dynamics. Namely, this technique uses a tailored APT which one can customize by changing the CEP of the IR field in the HHG process.

4.4 Principle of the coherent control experiment

The principle of the experiment is presented in Figure 4.3. Attosecond pulse trains are generated *via* high harmonic generation with a two-color femtosecond field (800+400nm). Depending on the intensity ratio r and the relative phase ϕ between the two components of the field, attosecond pulses with tailored temporal profile are produced. The pulses are then used to ionize an atomic target in the presence of a relatively weak IR field ($\sim 10^{11}$W/cm^2). Three quantum paths contribute to the generation of an electron wavepacket at a given energy E_q in the

continuum: the direct transition by one XUV photon absorption (harmonic H_q) and two transitions involving absorption of one XUV photon (harmonics H_{q-1} and H_{q+1}), and absorption or emission of one IR photon. These three paths interfere, leading to an energy-dependent asymmetric electron emission along the direction of polarization of the light as pictured in the filmstrip sketch shown in Figure 4.3 [26, 113]. Within the framework of second-order perturbation theory, it can be shown that the asymmetric component I_a of the electron emission is related to the spectral components of the attosecond pulses as [114, 115]:

$$I_a(q,\tau) \sim I_0(q) cos\left[\omega\tau + \psi(q)\right], \tag{4.50}$$

with

$$I_0(q) = |M_q|\left[|M_{q-1}|^2 + |M_{q+1}|^2 + 2|M_{q-1}||M_{q+1}|\cos\left(\phi_q^{q-1} - \phi_{q+1}^q + \varphi_{at.}^a + \varphi_{at.}^e\right)\right]^{\frac{1}{2}}, \tag{4.51}$$

and

$$\psi(q) = \text{atan}\left(\frac{|M_{q-1}|\sin(\phi_q^{q-1} + \varphi_{at.}^a) + |M_{q+1}|\sin(\phi_{q+1}^q - \varphi_{at.}^e)}{|M_{q-1}|\cos(\phi_q^{q-1} + \varphi_{at.}^a) + |M_{q+1}|\cos(\phi_{q+1}^q - \varphi_{at.}^e)}\right). \tag{4.52}$$

The one- and two-photon matrix elements M_{q-1}, M_q and M_{q+1} are proportional to the amplitude of the harmonics H_{q-1}, H_q, and H_{q+1}, respectively, $\phi_q^{q-1} = \phi_{q-1} - \phi_q$ and $\phi_{q+1}^q = \phi_q - \phi_{q+1}$ are the relative spectral phases between consecutive harmonics, $\varphi_{at.}^a$ and $\varphi_{at.}^e$ are small (hundreds of mradians) atomic phases associated to the ionization pathways, ω is the angular frequency of the 800-nm field, and τ is the relative time delay between the APT and IR field. By tuning the spectral components of the APT, the photoelectron emission pattern can then be controlled, as indicated by Equation 4.50.

Our experiment bears a similarity with the recent study reported by Cheng *et al.*, where a sequence of three attosecond pulses combined with a relatively weak IR field is used as an efficient means for controlling the photoemission from atoms [112] through interferences between the temporally-delayed electron wavepackets. Our experiment demonstrates a reverse approach to control the emission that

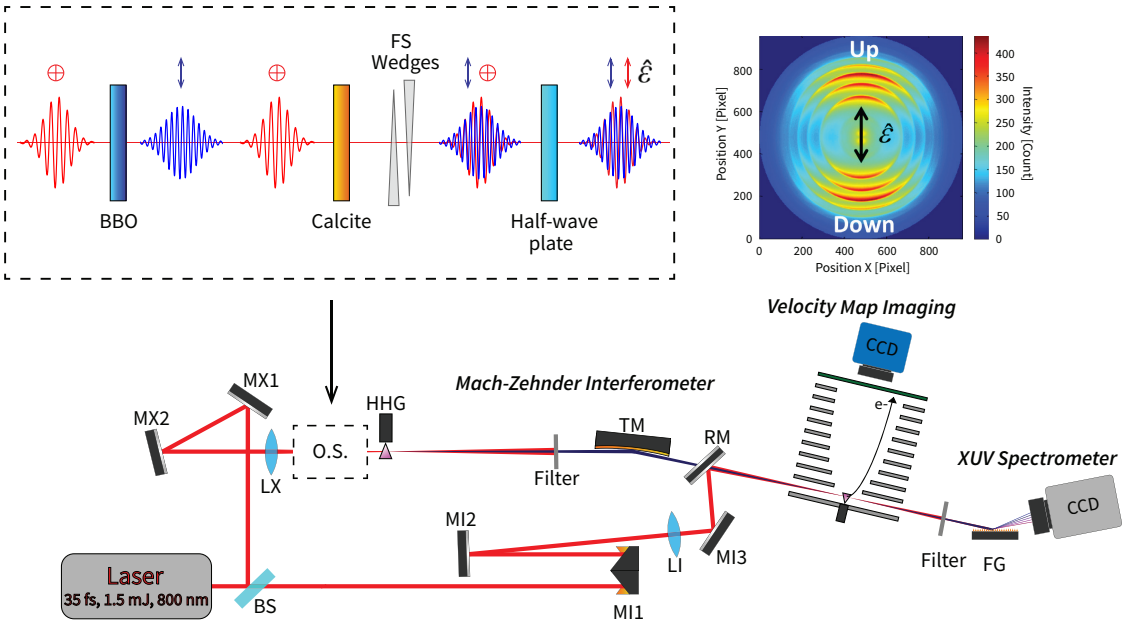

Figure 4.4: Schematic view of the experimental setup. It combines a femtosecond laser system, an attosecond XUV pump-IR probe Mach-Zehnder interferometer, a velocity-map imaging system (VMI), and an XUV spectrometer. Attosecond pulse trains are generated with a linearly-polarized two-color field (800+400nm) formed with a collinear optical system (O.S.). The attosecond pulses are then used to ionize argon gas in the presence of the IR field. Both the energy and angular distributions of the photoelectron emission are captured by the VMI system. The asymmetric component of the electron emission along the direction of polarization of the light $\hat{\varepsilon}$ is deduced from the electron yields measured on either side (up and down) of the polarization vector. BS: 80/20 beam splitter, MX1,2 and MI1,3: mirrors, LX and LI: lenses, RM: recombination mirror, TM: toroidal mirror, FG: flat-field grating.

consists in directly tuning the spectral components of the attosecond pulse in the Fourier domain.

4.5 Experimental setup

The experiment was performed at the ASAP (Auburn Source of Attosecond Pulses) laboratory. A schematic view of the experimental setup is shown in Figure 4.4. It combines a Ti:Sapphire laser delivering linearly-polarized 35-fs, 800-nm pulses at a 10kHz repetition rate, a stabilized XUV-IR Mach-Zehnder interferometer, a velocity-map imaging system, and an XUV spectrometer [116]. APTs made of both

odd and even harmonics were generated with a linearly-polarized two-color (800- and 400-nm) field *via* high harmonic generation [93, 117] in one arm of the interferometer. The two-color field was created in a collinear geometry using a β-barium-borate (BBO) crystal, a calcite plate, and a zeroth-order half-wave plate (at 800 nm) [114]. The duration of the 400-nm pulse was not measured directly, but is expected to be somewhat longer than the 800-nm pulse. The relative intensity ($r = I_{400}/I_{800}$) between the two colors was adjusted by tuning the phase matching conditions in the BBO while maintaining the total intensity relatively constant. A few-degree rotation of the BBO crystal along its axis perpendicular to the polarization of the incoming light allowed for adjusting the relative intensity in between 0.5% and 3%. The relative phase ϕ between the two colors, on the other hand, was controlled with a pair of fused-silica wedges. The absolute phase between the 400- and 800-nm fields was also not measured directly but was instead inferred from theoretical calculations as described later. The resulting linearly polarized two-color field was focused onto a 2-mm windowless gas cell filled with 10 Torr of argon. The peak intensity at the interaction region was estimated to be $\sim 2 \times 10^{14}$W/cm^2 from the cut-off energy of the high harmonics produced. APTs with an average duration of 10-20 fs were then formed by filtering out the harmonics below the 11^{th} order with an ultra-thin Al foil. A replica of the IR (without the 400 nm) was sent into the other arm of the interferometer, whose total length could be changed to vary the time delay between the APT and the IR pulses. Both beams were focused, co-axially recombined, and finally sent into a vacuum chamber containing an effusive argon gas jet. At the focal point, the IR intensity is estimated to be below 10^{11} W/cm^2. A home-built velocity map imaging system was used to capture the photoelectron emission [57]. The three-dimensional photoelectron momentum distributions were then reconstructed using the DAVIS algorithm [62].

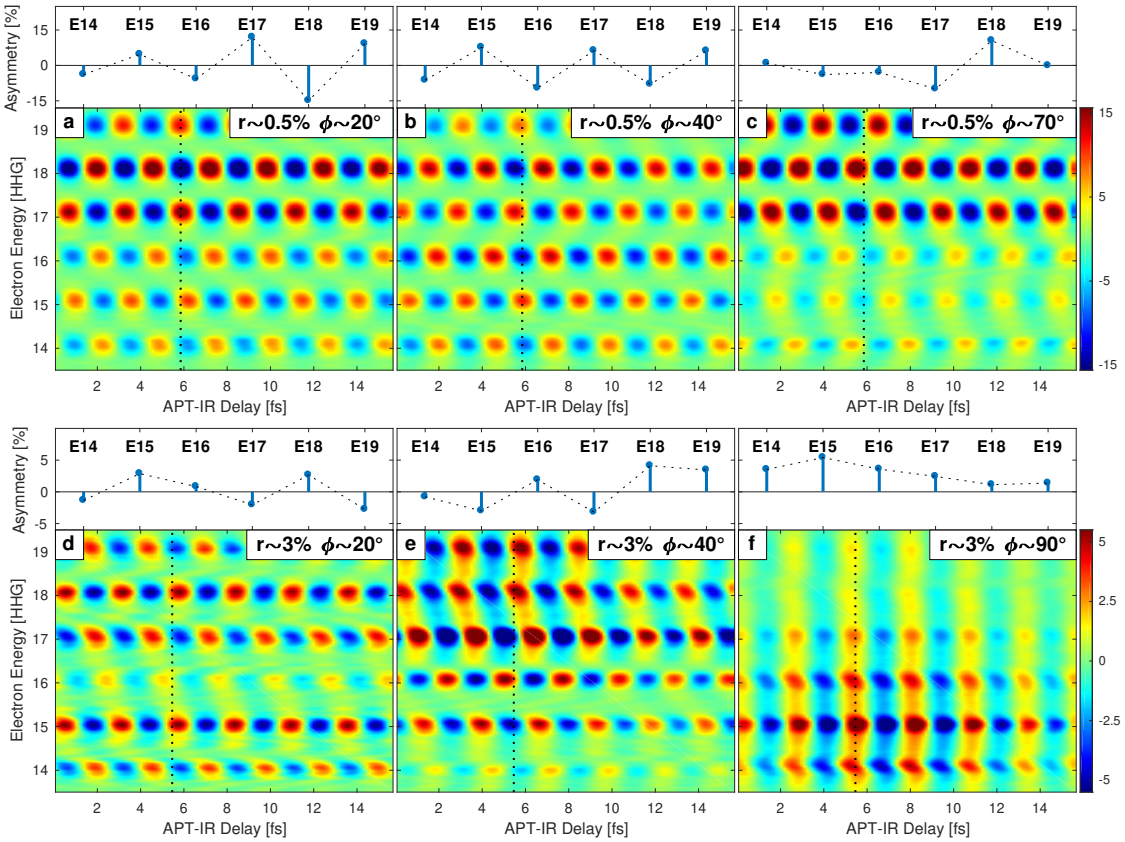

Figure 4.5: Density plot of the asymmetric component of the photoelectron emission [defined as $(Y_{up} - Y_{down})/(Y_{up} + Y_{down})$, where Y is the electron yield] as a function of the time delay between the APT and IR fields and the photoelectron energy, for different intensity ratio r and relative phase ϕ between the two colors of the HHG driving field. For illustrative purposes, the asymmetric components for electron energies corresponding to HHG orders H14 to H19 at the time delay indicated by the dashed line are shown in the top panels.

4.6 Results

4.6.1 Attosecond control of the electron emission

Figures 4.5.(a-f) show the measured asymmetric component of the photoelectron emission [defined as $(Y_{up} - Y_{down})/(Y_{up} + Y_{down})$, where Y is the electron yield] in a density plot as a function of the time delay τ between the APT and IR field and the photoelectron energy. These measurements were performed with APTs generated with two-color driving fields having distinct intensity ratio r and relative phase ϕ between the 400-nm and 800-nm components. At the electron energy associated to a given harmonic order, the asymmetric component oscillates with τ

at the frequency ω of the 800-nm IR field ($T \simeq 2.7fs$), as indicated by Equation 4.50. The phase of the oscillation, on the other hand, varies with the photoelectron energy, giving rise to unique emission patterns. It can be observed that the emission pattern strongly depends on both r and ϕ. At low intensity ratio ($r \sim 0.5\%$) and for a relative phase ϕ close to 20° (Figure 4.4.a), the asymmetric emission exhibits a checkerboard-like pattern, revealing that electrons with energy associated to odd and even HHG orders are emitted in opposite directions, respectively. The asymmetry is stronger for the most energetic electrons, though. At $\phi \sim 40°$, a more consistent checkerboard-like pattern is observed as the asymmetry is nearly constant over the whole photoelectron energy range (Figure 4.5.b). As the phase between the two components of the driving field is further increased, such a checkerboard-like pattern gradually fades. At $\phi \sim 70°$, electrons with energy associated to HHG orders H14, H15, and H16 are roughly emitted in the same direction (Figure 4.5.c). The dependence of the emission pattern on ϕ is even more pronounced at a higher intensity ratio between the two colors. Comparing Figures 4.5.d, 4.5.e, and 4.5.f, it can be seen that the emission pattern smoothly evolves from a checkerboard-like to a stripe pattern, which indicates that the photoelectrons are emitted in the same direction for a given APT-IR delay. Considered together, these measurements provide good evidence that the photoelectron emission can be manipulated by shaping the temporal profile of the two-color HHG driving field.

4.6.2 Spectral components of the attosecond pulses

To reveal the mechanisms responsible for the coherent control observed in Fig. 4.5, we have retrieved the average spectral components (amplitudes, phases) of the attosecond pulses used in the experiments. The spectra of the APTs were directly measured with both the VMI and XUV spectrometers in the absence of IR field. The relative spectral phases between consecutive harmonics, on the other hand, were determined by solving the system of coupled equations Eqs.(2) with the iPROOF procedure described in Ref. [114]. The spectral components and the reconstructed temporal profiles of the APTs used in the measurements shown in Fig. 4.5(a-f) are

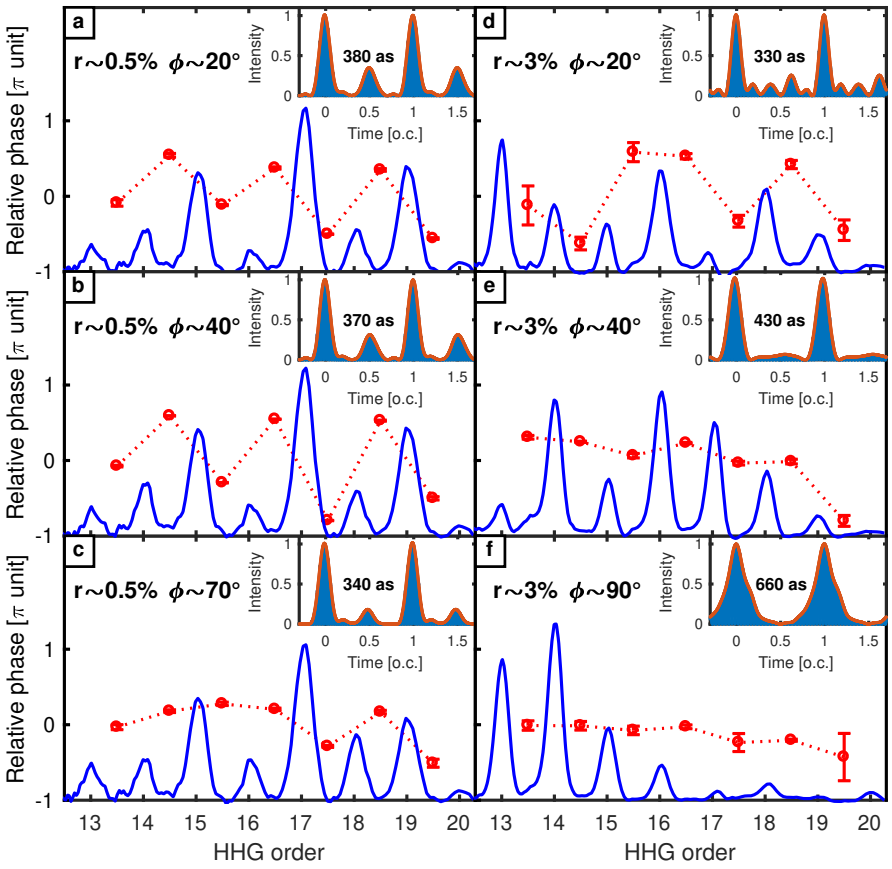

Figure 4.6: Average spectral components [spectra (blue) and relative phases between consecutive harmonics (red)], and average temporal profile (inset plots) of the attosecond pulses in the train retrieved from Fig. 4.5(a-f).

plotted in Fig. 4.6(a-f), respectively. At low intensity ratio (r∼0.5%), it can be seen that neither the shape of the spectrum nor the temporal profile of the APT vary much with the phase difference ϕ between the two colors of the driving field, which indicates that the control of the electron emission is achieved almost uniquely by tuning the spectral phases of the APT. Indeed, as shown in Figures 4.6(a-c), the relative phases between consecutive harmonics strongly depends on ϕ. For $\phi \sim 20°$ and 40°, large relative phase shifts are observed over the whole harmonic range. At $\phi \sim 70°$, the phase shifts decrease, especially for lower harmonics (13^{th} to 17^{th}) where the relative phases are nearly constant. At higher intensity ratio (r∼3%), the situation changes as both the spectrum and the relative phases (and consequently the temporal profile) of the APT strongly depends on ϕ. In that case, the emission pattern is thus determined by both the relative amplitude and

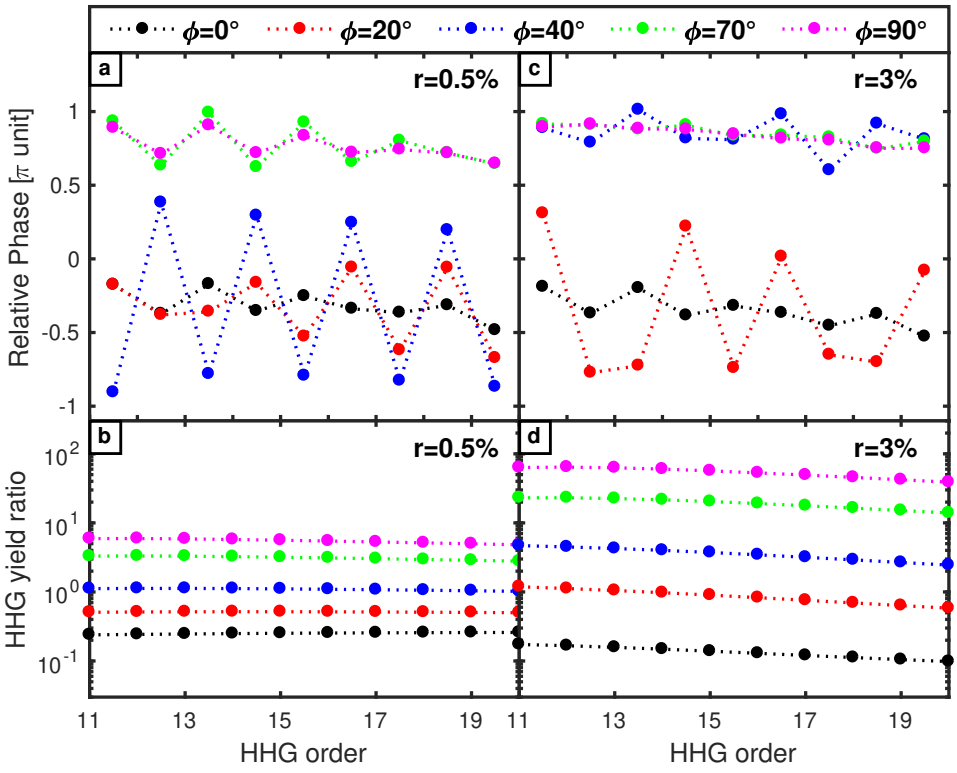

Figure 4.7: Calculated relative phase between consecutive odd and even harmonics (a,c) and ratio between the HHG rates generated by each half-cycle of the driving field (b,d). Calculations were made for $I_{800} = 2 \times 10^{14}$W/cm^2 and for various intensity ratios r and relative phases ϕ between the 400- and 800-nm components of the two-color driving field.

phase of the harmonics as predicted by Equation 4.50.

4.6.3 Relative phase between odd and even harmonics

To better understand the observed dependence of the relative phases between odd and even harmonics on the temporal shape of the two-color driving field, we performed theoretical calculations of the HHG process within the Strong Field Approximation (SFA) theory [11, 118], which has proved to be successful at qualitatively reproducing the characteristics of the XUV radiation (amplitude, phase, emission time, ...) generated with single- and multi-color fields [93, 99, 100, 108]. Calculations were made for $I_{800} = 2 \times 10^{14}$W/cm^2 and for various intensity ratios r and relative phases ϕ between the 400- and 800-nm components of the two-color driving field. Both the harmonic emission rate A_q^n and the emission time $t_{e,q}^n$ from the short trajectory were calculated for each half-cycle of the driving fields (labelled

n with n=0,1). The temporal profile $E_q(t)$ of the electric field for the harmonic radiation of order q was then reconstructed by adding both contributions coherently:

$$E_q(t) = \sum_{n=0}^{1} (-1)^n A_q^n \cos\left(\omega_q(t - t_{e,q}^n - nT/2)\right) = A_q \cos(\omega_q t + \varphi_q) \tag{4.53}$$

where A_q, φ_q, and ω_q are the amplitude, spectral phase, and angular frequency of the harmonic of order q, respectively, and T is the period of the 800-nm component of the driving field. The calculated relative phase between consecutive odd and even harmonics $\Delta\varphi = \varphi_{q+1} - \varphi_q$ for different ratios r and relative phases ϕ between the two components of the HHG driving field are plotted in Figures 4.7(a,c) as a function of the harmonic order. Our calculations qualitatively reproduce the relatively large phase shifts observed experimentally as well as their dependence with r and ϕ. At low ratio ($r = 0.5\%$), the phase shifts are maximum for $\phi \sim 40°$, and decrease as ϕ tends to 0 or 90°. The same dependence is observed at $r = 3\%$, even though the phase shifts are overall smaller, with a maximum obtained at $\phi \sim 20°$. The origin of the phase shifts lies in the relative strength of the harmonic emission rates produced by each half-cycle of the driving field, quantified by the ratio A_q^1/A_q^0 (see Figures 4.7(b,d)). The relative phase shifts are maximum for a ratio close to one, which corresponds to the case where both half-cycles contribute equally to the harmonic generation. In that case, two attosecond pulses are emitted per optical cycle. It is worth noting that in the limit of equal emission rates ($A_q^0 \simeq A_q^1$), which could be achieved with a very weak perturbative second harmonic field, Equation 4.53 reduces to $E_q(t) \propto \sin(\omega_q[t - (t_{e,q}^0 + t_{e,q}^1)/2] - q\pi/2)$, predicting a relative phase shift between odd and even harmonics close to $\pi/2$ as it has been observed in previous studies [26, 115, 119]. On the other hand, when one half-cycle of the driving field contributes predominantly to the HHG emission process, leading to the generation of one main pulse per optical cycle, the relative phase shifts are nearly constant as shown in Fig. 4.7(c) for the cases ϕ =70° and 90°. Note that the mean value of the phase shifts indicates which half-cycle contributes the most to the emission: the average phase shift lies in the range $[-\pi,0]$ ($[0,\pi]$) when the first (second) half-cycle contributes predominantly. At even higher ratio ($r > 10\%$), we observe that the

HHG emission is predominantly produced by one half-cycle regardless of ϕ and that the relative phase between odd and even harmonics remains nearly constant [93]. Based on the results of our SFA calculations, we have found that the tunability of the APT is optimized for an intensity ratio between 0.1 and 5%.

4.7 Computational Algorithm

In this section, the algorithm used to model our HHG spectrum and quantum orbits is explained. Although the three-step recollision model is enough to estimate the general behavior and maximum harmonic cutoff of the spectrum i.e. $E_{max} = I_p + 3.17U_p$, for a truly quantitative approach, some computation is required. The primary job of the algorithm is to calculate the time-dependent electric dipole and its Fourier transform. The intuitive physical description for this dipole D(t) is that the driving laser causes the electron density in the generation gas to move, and the oscillation dynamics of the charge density generates new harmonic frequencies. A suitable model is based on the SFA with the saddlepoint method as described earlier in this chapter. You can obtain a picture for the trajectories of the ionization/recombination using a discrete-time Fourier transform approach on the SFA results - which is accomplished by using a Gabor transformation in this algorithm. Another more precise way is to use the quantum orbits approach in the time domain. Solving the quantum orbits consists of taking the action integrals, Equation 4.30 and 4.31, applying the saddlepoint method to them, and finding numerical solutions to the trajectories.

We implemented an algorithm, developed in-house for LabVIEW by Dr. Laurent, which computes the time-dependent electric dipole, returns the HHG spectrum, and numerically solves the quantum orbits problem for the long and short trajectories. The steps in the algorithm include a calculation of the saddlepoints p_s using Equation 4.40 or 4.45, calculating the dipole matrix elements $d(p_s)$ and $d^*(p_s)$ using Equation 4.48, and then the action term $S(p_s, t, t')$ as well as other constituent factors of the dipole. To obtain the spectrum requires more than just taking the FFT of $D(t)$. This is because the electric dipole is driven by a laser field with

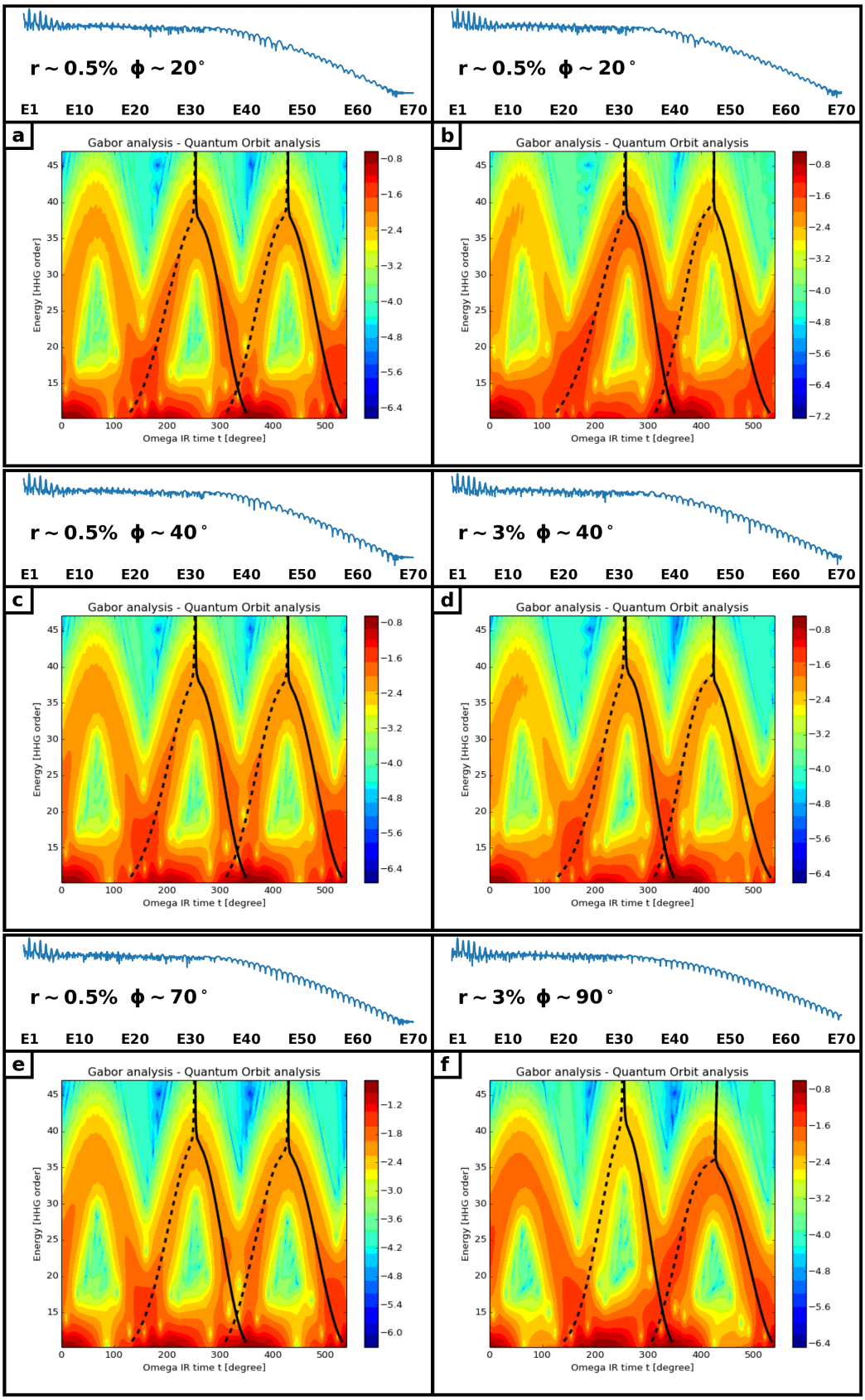

Figure 4.8: Results of the SFA and Quantum Orbits algorithm for two-color HHG. In each sub-figure, the HHG spectrum (solid blue) is displayed.

an envelope - it will not be the same in the middle as it was at the start of the pulse. By performing a type of discrete-time Fourier Transform called the Gabor transform, one can see how the spectrum changes over time even as the laser pulse does. We use a Gaussian shaped Gabor window to compute the D(t), and then performs the FFT, shifting the window in steps of the IR photon optical cycle. What comes from this is how harmonics are generated as a function of time. Solving the quantum orbits is carried out by a numerical version of solving the Equations 4.41 and 4.42 or Equations 4.46 and 4.47.

The results in the algorithm are displayed in Figure 4.8. The spectrum and Quantum Orbits for each of the six cases of Figure 4.6 are provided. We can focus on several noticeable features: the HHG spectrum cutoff, the complexion of the Gabor transform analysis, and the shapes of the Quantum Orbits overlaid on the Gabor colormap. As can be expected, when higher intensities UV component are present, the cutoff is extended to higher harmonics. Next we can see by looking at the Gabor analysis that the lower harmonics are produced throughout the phase of the driving field, but the presence of higher harmonics both vary at different recombination times, and reach a cutoff (i.e. drastic reduction past H45). In considering the Quamtum Orbits (short return times dashed, long return times solid), let us compare the correlated data back in Figure 4.6 to the present data here in Figure 4.8. Namely for given r and ϕ compare the harmonic strength and average temporal profile of the attosecond pulse trains in Figure 4.6 to the relative heights and shapes of the return times in Figure 4.8. When the strength of the UV is low, as in Figures 4.6.a, 4.6.c, and 4.6.e, the strength of the even harmonics is also very small and the temporal profile shows attosecond structure with peaks at twice the optical cycle. Looking over Figures 4.8.a, 4.8.c, and 4.8.e, the neighboring half-cycles show a consistency of relative heights of the Quantum Orbit return times as well as Gabor transform density. As expected, the presence of stronger UV intensity produces a temporal profile with peaks once per optical cycle. In a special case, consider how in Figure 4.6.f the temporal profile has the smoothest once per optical cycle structure, where every other half-cycle peak has vanished. Correspondingly in

4.8.f. the density represented by the Gabor cycle is diminished every other half-cycle as well. The quantum orbits of the vanishing pulse still appear, but can be ignored.

4.8 Conclusions

In conclusion, we have shown that the photoelectron emission produced from atoms by absorption of an APT made of odd and even harmonics in the presence of a relatively weak IR field ($\sim 10^{11}$ W/cm^2) can be coherently controlled by tailoring the temporal profile of the APT. Emission patterns where photoelectrons are emitted in the same direction or, conversely, are emitted in opposite directions depending on their energy can be obtained by tuning one or both spectral components (amplitude, phase) of the pulse. From these patterns, we have also shown that APTs generated with a two-color HHG driving field exhibit a high temporal tunability, which can be reasonably well predicted within the Strong Field Approximation (SFA) theory. Our work shows that attosecond pulse shaping for coherent control of quantum phenomena is steadily becoming a reality. We expect that this approach can be applied to control more complex quantum systems, thus offering new capabilities for the growing field of attochemistry.

"When I am judging a theory, I ask myself whether, if I were God, I would have arranged the world in such a way."

— Einstein

5

Probing Temporal Aspects of Laser-Assisted Photoionization

Contents

5.1 Introduction to Photoionization Delays

The interaction of light and matter is one of the most fundamental processes in nature. One example, photoionization, has been earnestly studied for decades with synchrotron radiation [120], and recently attosecond pulses have been employed

[24, 121–123]. During photoionization with an attosecond pulse, a bound-state electron in the target system absorbs a photon and jumps free to a continuum state. If this interaction is also dressed by an ultrashort IR or UV laser pulse, an additional photon is emitted or absorbed initiating a continuum-continuum transition. When the delay between the attosecond pulse and dressing pulse is changed, a pump-probe measurement can be carried out to interrogate the physics in the time domain. In the past, the time for such events as ionization and photon absorption/emission were regarded as practically instantaneous. Nevertheless, with the development of attosecond time-resolved measurements, the importance of the shortest duration events has gained considerable interest. Attosecond pump-probe experiments are currently the most precise techniques for measuring in the temporal domain of electronic events.

In recent years, attosecond science has experimentally verified that delays in photoemission attributed to ionization are in the range of tens to hundreds of attoseconds. Developing ways to reliably measure the photoionization delays remains a challenging area that is still maturing, though. In attosecond measurements, photoionization of the target followed by absorption or emission of a probe photon produces an electron wave packet (EWP) which imbibes a phase contribution from each transition. Figure 5.1 is a simple depiction of each step. One phase (delay) taken by the electron comes from the photoionization. This phase represents the group delay of the EWP as it scatters through the potential of its parent atom. This has been named the Wigner delay[23, 124–126], and the zero of this time starts with the arrival of the ionizing radiation. Another delay occurs due to the continuum-continuum transition which is caused by emission/absorption of the dressing laser photon. This delay is dependent on the kinetic energy of the EWP after photoionization, and the wavelength of the probe photon. Although exact calculations for these delays is theoretically burdensome to calculate, the Wigner delay has a simple form for hydrogenic systems, and the continuum-continuum delay can be easily approximated [24, 127, 128]. The Wigner delay and continuum-continuum delay together make up the atomic phase of the EWP. The total

phase of the EWP also contains a copy of the spectral phase of the from the attosecond pulse. Thus we can say that the EWP photoemission is like a replica of the attosecond pulse that also holds information from the photoemission. We distinguish photoionization as a process that results in photoemission which contains a distribution of EWP final states.

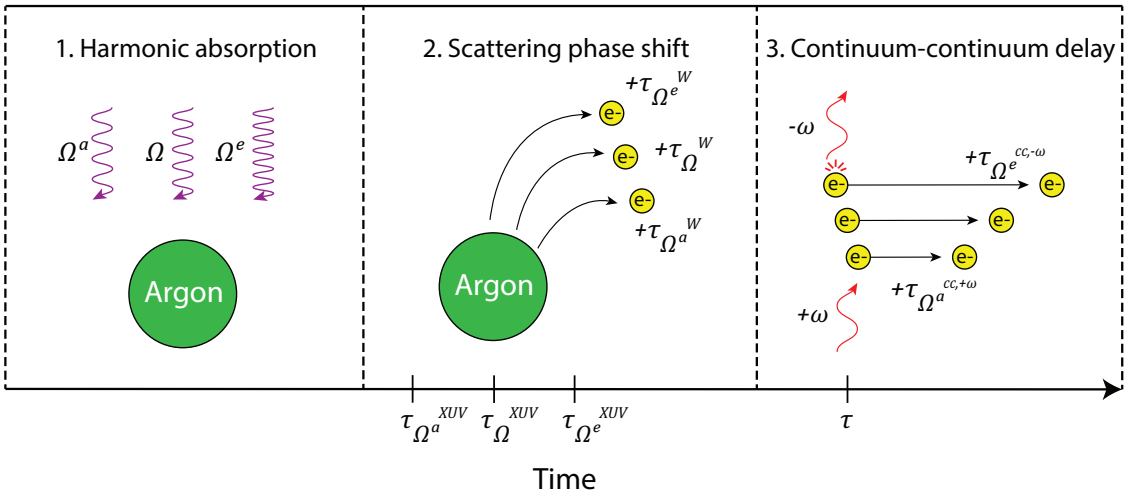

Figure 5.1: The photoemission process. In the first frame, ionizing harmonic photons are absorbed beginning at the arrival of the attosecond pulse. Next, as the electrons escape via a bound-continuum transition, they collect a scattering phase-shift (which includes the Wigner delay) as they escape the ionic core. Finally, the dressing field contributes a phase due to absorption or emission called the continuum-continuum delay.

In this chapter, a novel experimental procedure is presented whose purpose is to isolate the differential delay between the continuum-continuum absorption and emission for a given EWP kinetic energy. We develop a theoretical description and follow with a study on the transitions of outer shell (3p) electrons of an argon target gas. For the theoretical process, We will first show from first principles a foundational description of the interactions of atoms with electromagnetic radiation in Section 5.2. This will include the dipole selection rules that help predict the transitions that occur, and the perturbation theory for the relevant one and two-photon transitions. In Section 5.3 several successful measurements that isolated the atomic delay are introduced. Next in Section 5.4, the two-photon two-color experiments we conduct observing RABBITT sidebands and First Order/Second

Order Interferences will be described in detail. The experimental techniques rely on established attosecond pump-probe methods. In Section 5.5 the analysis conducted on the data will be covered. Then finally, we draw our conclusions in 5.6.

5.2 Interaction of Atoms with Electromagnetic Radiation

A quantum mechanical description can tell us about the accessible states of an atom when it absorbs or emits a photon. The quantum selection rules show us the allowed and forbidden transitions, and propensity rules can intuitively tell us which allowed transitions are dominant[90, 129]. When we use perturbation theory to describe light-matter interactions we can link the theoretical description to experiment. The studies we conduct involve one and two-photon transitions, and transition matrix elements from perturbation theory provide a simple way to piece together the description of the physics. What follows is a fairly standard explanation of these concepts. An accessible derivation for the selection rules and transition matrix elements can be found in Bransden's and Joachain's book [130]. As we progress toward the context of attosecond physics with laser-assisted ionization, we make reference to and unify the theoretical notations and conventions of [121, 127].

5.2.1 One and Two-Photon Interactions

We can begin our description with the time dependent Schrödinger equation. We assume our system is a hydrogenic one, and employ the single-active electron (SAE) approximation

$$j\hbar\frac{\partial}{\partial t}\Psi(\boldsymbol{r},t) = H(t)\Psi(\boldsymbol{r},t) \tag{5.1}$$

where we use j to represent the imaginary unit defined by $j = \sqrt{-1}$, $\Psi(\boldsymbol{r},t)$ is the time-dependent wavefunction, and $H(t)$ is the Hamiltonian. For the hydrogenic atom in the presence of an electric field, the Hamiltonian $H(t)$ contains a unperturbed part $H_0(t)$, as well as one for the interaction with electromagnetic radiation $H_{int}(t)$. The

radiation interaction is in terms of the field's vector potential $\boldsymbol{A}$ and momentum $\boldsymbol{p}$. It satisfies the Coulomb gauge in the form

$$H(t) = \left(-\frac{j\hbar^2}{2m}\nabla^2 - \frac{Ze^2}{4\pi\epsilon_0 r}\right) + \left(\frac{e}{m}\boldsymbol{A}\cdot\boldsymbol{p} + \frac{e^2}{2m}\boldsymbol{A}^2\right) \tag{5.2}$$

where $\hbar$ is Planck's constant, ϵ_0 is the permittivity of free space, m and e are electron mass and charge, and Z is the nuclear charge of the atom ($Z = +1$ for neutral system). In the perturbative regime, the $\boldsymbol{A}^2$ term is neglected, and the interaction term coming from the second set of parentheses can be written with knowledge of the quantum mechanical momentum operator, $\boldsymbol{p} = -j\hbar\frac{e}{m}\nabla$

$$H_{int}(t) = -j\hbar\frac{e}{m}\boldsymbol{A}\cdot\nabla. \tag{5.3}$$

For a linearly polarized monochromatic plane wave, the vector potential can be expressed in the form

$$\boldsymbol{A} = A_0\exp(j\boldsymbol{k}\cdot\boldsymbol{r})\hat{\boldsymbol{\epsilon}} \tag{5.4}$$

where $\hat{\boldsymbol{\epsilon}}$ is the light polarization. Obtaining the perturbative transitions for such a system requires the evaluation of matrix elements of the form

$$M_{if} = \langle f|H_{int}|i\rangle\,, \tag{5.5}$$

where we have begun to use bra-ket notation. When in the presence of electromagnetic radiation, there is a probability for atoms to absorb a photon and make a transition to a quantized bound state or free continuum state. Transition probabilities are quantified using the transition matrix elements which have encoded within them spectral phase information of the light responsible for the transition as well as phases of the atomic physics. Our matrix element can be rewritten with the expressions obtained from Equations 5.3 - 5.5.

$$M_{if} = \hat{\boldsymbol{\epsilon}}\cdot\,\langle f|\exp(j\boldsymbol{k}\cdot\boldsymbol{r})\nabla|i\rangle \tag{5.6}$$

In the case where the wavelength of the radiation is large in comparison to the spatial dimensions of the wave function, remembering $k \propto 1/\lambda$, the dipole approximation can be made where $\exp(j\boldsymbol{k}\cdot\boldsymbol{r}) \approx 1$, therefore the matrix element becomes

$$M_{if} = \hat{\boldsymbol{\epsilon}}\cdot\,\langle f|\nabla|i\rangle\,. \tag{5.7}$$

The momentum operator is defined with the nabla operator ∇, and has in it's definition the velocity $\dot{\boldsymbol{r}}$. The velocity is equal to the quantum mechanical commutator $(j\hbar)^{-1}[\boldsymbol{r}, H_0]$ where we have specified H_0 since we are in a perturbative regime. With these substitutions, the dipole approximation for M_{if} becomes

$$M_{if} = \frac{(\varepsilon_f - \varepsilon_i)m}{\hbar^2} \hat{\boldsymbol{\epsilon}} \cdot \langle f|\boldsymbol{r}|i\rangle \,. \tag{5.8}$$

One can see the transition frequency between the two states $\omega_{if} = (\epsilon_f - \epsilon_i)/\hbar$. Quite often in the literature the dipole operator $\boldsymbol{D}$ appears. This gives us a more intuitive form that clearly displays the nature of the transition.

$$M_{if} = \hat{\boldsymbol{\epsilon}} \cdot \langle f|\boldsymbol{D}|i\rangle \,. \tag{5.9}$$

When the conditions are present for two-photon transitions, intermediate states, sometimes called virtual states, are accessed. In a second order transition, where we have dropped the constants tacked on the front of Equations 5.9, the two-photon matrix element appears as

$$M_{if} = \langle f|D_2(\varepsilon - H_0)^{-1} D_1|i\rangle \,. \tag{5.10}$$

The resolvent operator (the energy and Hamiltonian sandwiched between the Dipole operators) can be expanded using the property of the identity matrix [131]

$$\hat{R} = \sum\!\!\!\!\!\!\int_{\kappa} \frac{|\kappa\rangle \langle\kappa|}{(\varepsilon - \varepsilon_\kappa)}, \tag{5.11}$$

where the energy ε_κ is that of the virtual intermediate state with momentum κ. With this notation, the subscript κ denotes the various possible intermediate transitions between the initial and final states. Equation 5.10 can be rewritten as

$$M_{if} \propto \sum\!\!\!\!\!\!\int_{\kappa} \frac{\langle f|\, D_2\, |\kappa\rangle \langle\kappa|\, D_1\, |i\rangle}{\varepsilon - \varepsilon_\kappa} \tag{5.12}$$

The conspicuous looking operator $\sum\!\!\!\!\!\!\int$ in Equation 5.12 indicates the sum over all accessible states, not just the quantized states (sum), but all those in the continuum (integral).

5.2.2 The Dipole Selection Rules

Not all atomic transitions are accessible. The quantum selection rules tell us which of them are allowed, and which are forbidden. Applying these rules provides foresight in knowing which states we can expect to observe. The selection rules can be mathematically demonstrated to depend on the odd and even symmetries of the atomic wavefunctions. Looking back at Equation 5.8 one will see that the dipole operator contains the expectation of the position. We consider the restriction to linear polarization of the light. A common convention for linearly polarized light is polarization in the z-direction i.e. $\hat{\boldsymbol{\epsilon}} = \hat{\boldsymbol{z}}$. We can convert z to spherical polar coordinates.

$$z = \left(\frac{4\pi}{3}\right)^{1/2} r \times Y_{1,0}(\theta, \phi) \tag{5.13}$$

This can be substituted into the integral Equation 5.8. It can also be separated by its radial and angular components

$$\begin{aligned} \hat{\boldsymbol{z}} \cdot \langle f|\boldsymbol{z}|i\rangle = \left(\frac{4\pi}{3}\right)^{1/2} & \int R_{n_f,l_f}(r) R_{n_i,l_i}(r) r^3 dr \\ & \times \int Y_{l_f,m_f}(\theta,\phi) Y_{1,0}(\theta,\phi) Y_{l_i,m_i}(\theta,\phi) d\Omega \end{aligned} \tag{5.14}$$

where $R_{n,l}(r)$ is the radial part of the Hydrogenic wavefunction, and $Y_{l,m}$ is the spherical harmonic. It is common to read about how the selection rules stem from symmetry arguments, and it is simple to follow logical and mathematical reasoning behind this statement. The most significant selection rule to remember, with regards to transitions due to linearly polarized light, is that the change in orbital angular momentum l for a one photon transition must be $\Delta l = \pm 1$. The Laporte rule states that dipole transitions connect states of opposite parity for centrosymmetric atoms and molecules. The symmetry of a hydrogenic wavefunction can be tested by applying the parity operator, defined by its action on kets in position space $\hat{P}\,|\boldsymbol{r}\rangle = |-\boldsymbol{r}\rangle$. To test the behavior of Hydrogenic wavefunctions under parity transformation, note that $\hat{P}\,[R_{n,l}(r)Y_{l,m}(\theta,\phi)] = R_{n,l}(r)Y_{l,m}(\pi-\theta,\phi+\pi)$ which can also be stated $\psi_{n,l,m}(r,\theta,\phi) \rightarrow (-1)^l \psi_{n,l,m}(r,\theta,\phi)$. So the eigenvalue of the parity operator is $+1$ for even functions, and -1 for odd functions. Therefore the

parity of the integral depends on the orbital angular momentum, and it indicates the even/odd symmetry. Consider also that the integrals of odd functions over all space are zero, and those which are even are nonzero. There are three spherical harmonics in the angular integrand of Equation 5.14, and to be even, the two representing initial and final states must have opposite symmetry so the overall product is an even function. This comes from the fact that the product of two odd or two even functions is even, and the product of an odd function with an even function is odd. Also recalling that a conservation of total angular momentum is required, and photons carry spin angular momentum of 1, this is the required change in the orbital angular momentum.

Another rule for the case we're in pertains to the angular momentum magnetic number. Observe that $\Delta m = 0$. Let us recall that Spherical Harmonics can be expressed in terms of products of the Associated Legendre Polynomials and complex exponentials as

$$Y_{l,m}(\theta, \phi) = N_{l,m} P_{l,m}(\cos\theta) e^{jm\phi}. \tag{5.15}$$

If we define the angular integral I_{ang} where $I_{ang} = \int Y_{l_f,m_f}(\theta,\phi) Y_{1,0}(\theta,\phi) Y_{l_i,m_i}(\theta,\phi) d\Omega$, the integral of spherical polar coordinates can be expressed anew

$$I_{ang} = \int P_{l_f,m_f}(\cos\theta) P_{1,0}(\cos\theta) P_{l_i,m_i}(\cos\theta)\sin(\theta) d\theta \times \int e^{-jm_f\phi} e^{jm_i\phi} d\phi. \tag{5.16}$$

There is an easy observation that the integral over ϕ will be zero unless $\Delta m = 0$, which is a special case for linearly polarized light. This concludes the explanation for the selection rules mentioned, and additional cases of polarization are found in [130]. In Figure 5.2, an application of these principles to the system under our study is shown. If we consider the possibility of two-photon transitions beginning from the Argon 3p shell, there are several angular momentum channels that can take place. For the p shell, $l_i = 1$ and $m_i = 0, \pm 1$. With the first transition $\Delta l = \pm 1$ and $\Delta m = 0$. This constrains intermediate states to be accessible for angular momentum $\lambda = 0$(s) or $\lambda = 2$(d). With the absorption or emission of another photon, the rules are applied once more.

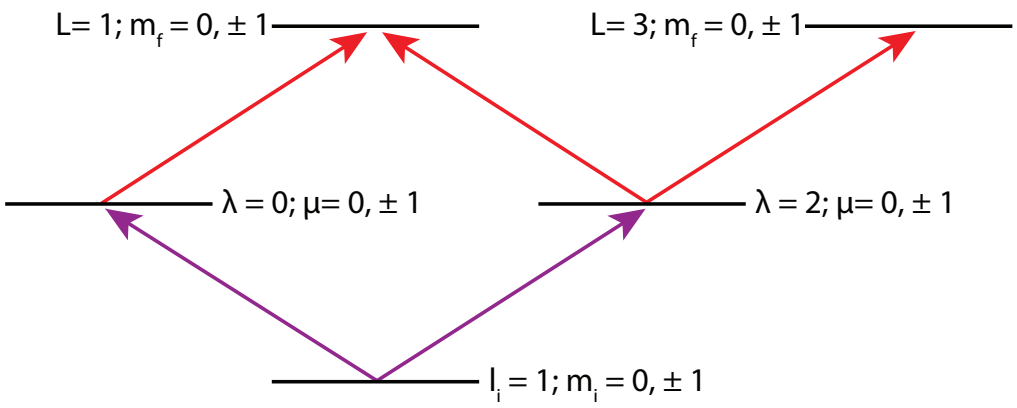

Figure 5.2: Application of the selection rules to p shell electrons with several angular momentum channels. A first transition takes place (absorption of a harmonic photon, purple) $\Delta l = \pm 1$ and $\Delta m = 0$ so that intermediate states with angular momentum $\lambda = 0$(s) or $\lambda = 2$(d) are accessible. With the absorption or emission of a probe photon (red) the rules are applied again.

5.2.3 Formalism of Two-Photon Two-Color Attosecond Measurements

In most attosecond pump-probe experiments, only one and two-photon transitions take place. Recalling to section 5.2.1, the transitions are represented by matrix elements like that of Equation 5.12. To more easily wield the matrix elements, we consider them in their complex variable form [81]. The complex magnitude-phase representation of a matrix element from initial state $|i\rangle$ to a final state $|f\rangle$

$$M_{if} = |M_{if}|e^{j\theta_{if}} \tag{5.17a}$$

$$\theta_{if} = \arg[M_{if}] \tag{5.17b}$$

where $|M_{if}|$ is the amplitude of the transition, and θ_{if} is the associated phase. A degeneracy of quantum paths starting at the same initial state, and ending at the same final state, will interfere with each other. To represent this, you have to take the sum of these coherent paths and square [131]. More generally, with an angular distribution of the photoemission, one observes

$$P = \sum_i \left| \sum_f M_{if} Y_{l_f,m_f}(\Theta,\Phi) e^{j\delta_{l_f}} \right|^2 . \tag{5.18}$$

The variables of the final state spherical harmonics $Y_{l_f,m_f}(\Theta,\Phi)$ are that of the measurement detection angles Θ and Φ. Also, the radial phase shifts δ_{l_f} are taken into account for states of different angular momentum. In the next section, a demonstration of how to wield the matrix elements of the form of Equation 5.17 is shown.

5.2.4 Transition Matrix Element Formulation.

In this section, a theoretical description of the interferences in our measurements is presented in terms of a transition matrix element formalism. The interferences arise from multiple channels that start from initial state with quantum numbers (n_i, l_i, m_i) and populate a final EWP energy state with momentum and energy (k, ε). We make use of the work by Dahlström [127] and the notation of Laurent [114] which makes the work of Toma and Muller [131], as seen in Equation 5.19, more transparent. We mainly consider the case of linearly polarized $(\hat{z})$ light with photoemission along the polarization axis. The matrix elements for one-photon direct (d) and two-photon continuum-continuum cc transitions are written with atomic units as [121]

$$M_d(k\hat{z},\varepsilon,\tau) = -jE_\Omega \langle k|z|i\rangle \tag{5.19}$$

and,

$$M_{cc}^{a/e}(k\hat{z},\varepsilon,\tau) = -jE_\omega E_{\Omega^{a/e}} \lim_{\epsilon\to 0^+} \sum_\kappa \!\!\!\!\!\!\int \frac{\langle k|z|\kappa\rangle \ \langle \kappa|z|i\rangle}{\varepsilon_i + \Omega^{a/e} - \varepsilon_\kappa + j\epsilon} \tag{5.20}$$

where $|i\rangle$ is the initial bound state, $|\kappa\rangle$ is the intermediate EWP continuum state reached by absorption of the XUV photon Ω, $|k\rangle$ is the final continuum state, and E_ω and E_Ω are the field representations of the probe pulse photon and attosecond pulse XUV photon respectively. We can separate the angular part and the radial part of the wavefunctions as

$$\langle \vec{r}|i\rangle = Y_{l_i,m_i}(\hat{r}) R_{n_i,l_i}(r) \tag{5.21}$$

$$\langle \vec{r}|k\rangle \propto \sum_{L,M} i^L e^{-i\eta_L(k)} Y^*_{L,M}(\hat{k}) Y_{L,M}(\hat{k}) R_{k,L}(r) \tag{5.22}$$

An explicit formulation of the matrix elements in Equations 1.19 and 1.20 come from Equations 47 and 48 of [127]. We keep the case of linear polarization with $m_i = 0$.

$$\begin{aligned} M_d(k\hat{z},\varepsilon,\tau) =& \frac{(8\pi)^{3/2}}{\sqrt{2}} E_\Omega \sum_L (-j)^L \sqrt{2L+1} e^{j\eta_L(k)} \\ & \times \langle Y_{L,0}|Y_{1,0}|Y_{l_i,0}\rangle \, T^{(1)}_{L,l_i}(k) \\ =& |M_d| e^{j\theta_d} \end{aligned} \tag{5.23}$$

and,

$$\begin{aligned} M^{a/e}_{cc}(k\hat{z},\varepsilon,\tau) =& \frac{(8\pi)^{3/2}}{\sqrt{2}} E_\omega E_{\Omega^{a/e}} \sum_L (-j)^L \sqrt{2L+1} e^{j\eta_L(k)} \\ & \times \sum_\lambda \langle Y_{L,0}|Y_{1,0}|Y_{\lambda,0}\rangle \, \langle Y_{\lambda,0}|Y_{1,0}|Y_{l_i,0}\rangle \\ & \times T^{(2)}_{L,\lambda,l_i}(k;\kappa) \\ =& |M^{a/e}_{cc}| e^{j\theta^{a/e}_{cc}} \end{aligned} \tag{5.24}$$

Where the radial part of the one and two-photon transitions are respectively

$$T^{(1)}_{L,l_i}(k) = \langle R_{k,L}|r|R_{n_i,l_i}\rangle \tag{5.25}$$

and,

$$T^{(2)}_{L,\lambda,l_i}(k;\kappa) = \langle R_{k,L}|r|\rho_{\kappa,\lambda}\rangle \, . \tag{5.26}$$

As seen with the appearance of $\rho_{\kappa,\lambda}(r)$, a large theoretical leap has been taken between Equations 5.20, 5.24, and 5.26 which is disclosed in Equations 6 and 7 of [127]. Instead of performing a more complicated integral, the radial amplitude $T^{(2)}_{L,\lambda,l_i}(k;\kappa)$ is obtained with the first order perturbed wavefunction $\rho_{\kappa,\lambda}(r)$ satisfies $[H_\lambda - \epsilon_\kappa]\rho_{\kappa,\lambda}(r) = -rR_{n_i,l_i}(r)$. We use the asymptotic approximation which reduces the radial parts of the wavefunctions to simple analytical forms as

$$\begin{aligned} \lim_{r\to\infty} R_{k,L}(r) &= \frac{N_k}{r}\sin(kr + \Phi_{k,L}(r)) \\ &= \frac{N_k}{2jr}\left(\mathrm{e}^{j(kr+\Phi_{\kappa,\lambda}(r))} - \mathrm{e}^{-j(kr+\Phi_{\kappa,\lambda}(r))}\right) \end{aligned} \tag{5.27}$$

$$\lim_{r\to\infty} \rho_{\kappa,\lambda}(r) \approx -\frac{\pi N_\kappa}{r}\mathrm{e}^{j(kr+\Phi_{\kappa,\lambda}(r))} \tag{5.28}$$

In Equation 5.27 we have the asymptotic radial part for the continuum EWP, and Equation 5.28 is the outgoing wavepacket in an intermediate state after absorption of the XUV harmonic photon.The equations have amplitude and phase terms which have been expressed in a compact way, $N_k = \sqrt{2/\pi k}$ and $\Phi_{k,L}(r) = Z\ln(2kr)/k + \eta_L - \pi L/2$. We identify the scattering phase-shift, to which we attribute the Wigner delay, $\eta_L = \sigma_L + \delta_L$. This is a sum of two terms - the Coulombic phase-shift σ_L and the deviation from hydrogenic behavior of the target δ_L (for hydrogenic systems $\delta_L = 0$). The integral is carried out as described from Equations 18 to 20 of [127]. The two photon matrix element (distinguished for absorption or emission with a/e) is finally written as

$$\begin{aligned} M_{cc}^{a/e}(k\hat{z},\varepsilon,\tau) \approx & -\frac{2\pi^2}{3}(8\pi)^{3/2}E_\omega E_{\Omega^{a/e}} N_k N_\kappa \\ & \times \frac{1}{|k-\kappa|^2}\exp\left[-\frac{\pi Z}{2}\left(\frac{1}{\kappa}-\frac{1}{k}\right)\right] \\ & \times \frac{(2\kappa)^{(jZ/\kappa)}}{(2k)^{(jZ/k)}}\frac{\Gamma[2+jZ(1/\kappa-1/k)]}{(\kappa-k)^{jZ(1/\kappa-1/k)}} \\ & \times \sum_{L=l_i,l_i\pm 2} Y_{L,m_i}(\hat{k}) \sum_{\lambda^{a/e}=l_i\pm 1} \left\langle Y_{L,m_i}\middle|Y_{1,0}\middle|Y_{\lambda_i^{a/e},m_i}\right\rangle \\ & \times \left\langle Y_{\lambda^{a/e},m_i}\middle|Y_{1,0}\middle|Y_{l_i,m_i}\right\rangle \left\langle R_{\kappa,\lambda^{a/e}}\middle|r\middle|R_{n_i,l_i}\right\rangle j^{-\lambda^{a/e}} e^{j\eta\lambda^{a/e}} \end{aligned} \tag{5.29}$$

This matrix element has the phase

$$\arg[M_{cc}^{a/e}] = \pi + \arg[Y_{L,m_i}(\hat{k})] + \phi_{\Omega^{a/e}}^{XUV} \pm \phi_\omega + \eta_{\lambda^{a/e}} + \phi_{\Omega^{a/e}}^{cc} - \frac{\lambda^{a/e}\pi}{2}. \tag{5.30}$$

In Equation 5.30, we account for all possible phase terms, including those of subtle artifacts (*i.e.* through Euler identities $j^{-k} = e^{-jk\pi/2}$, and $-1 = e^{j\pi}$). It is standard practice to drop the trivial phase terms from the spherical harmonics in the following development of a practical formalism. The continuum-continuum phase is readily discernible from Equation 5.29

$$\phi_{\Omega^{a/e}}^{cc} = \arg\left[\frac{(2\kappa)^{(jZ/\kappa)}}{(2k)^{(jZ/k)}}\frac{\Gamma[2+jZ(1/\kappa-1/k)]}{(\kappa-k)^{jZ(1/\kappa-1/k)}}\right]. \tag{5.31}$$

We mention now, and will recall later, that we consider an angle-integrated photoelectron spectrum in which we observe particular dominant transitions. In

the following passage, the transition matrix elements are expressed as modular components which can be used by applying rules of complex number arithmetic.

Let us consider a scheme where three quantum paths lead to the same final EWP continuum state. Figure 5.3 can be seen for reference. For the three matrix elements we have one describing a direct transition made by absorption of Ω, another for absorption of Ω^a and absorption of ω, and lastly one occurring with absorption of Ω^e and emission of ω. It is possible for the probe photons to be absorbed or emitted before Ω^a or Ω^e are absorbed, but these are insignificant contributions to the photoemission. We express the fields as

$$\tilde{E}_{\omega} = e^{j\omega\tau} \tag{5.32a}$$

$$\tilde{E}_{\Omega} = e^{j\phi_{\Omega}^{XUV}} \tag{5.32b}$$

$$\tilde{E}_{\Omega^a} = e^{j\phi_{\Omega^a}^{XUV}} \tag{5.32c}$$

$$\tilde{E}_{\Omega^e} = e^{j\phi_{\Omega^e}^{XUV}} \tag{5.32d}$$

We also have equations to represent the transition matrix elements. Equation 5.29 is greatly simplified when the matrix elements are written in the complex magnitude and phase representation

$$M_d(k\hat{z}, \varepsilon) = \tilde{E}_{\Omega}\tilde{M}_d, \tag{5.33a}$$

$$M_{cc}^a(k\hat{z}, \varepsilon, \tau) = \tilde{E}_{\omega}\tilde{E}_{\Omega^a}\tilde{M}_{cc}^a, \tag{5.33b}$$

$$M_{cc}^e(k\hat{z}, \varepsilon, \tau) = \tilde{E}_{\omega}^*\tilde{E}_{\Omega^e}\tilde{M}_{cc}^e. \tag{5.33c}$$

The phases of the matrix elements are then

$$\arg[M_d] = \phi_{\Omega}^{XUV} - \frac{L\pi}{2} + \phi_{\Omega}^{at.}, \tag{5.34a}$$

$$\arg[M_{cc}^a] = \phi_{\Omega^a}^{XUV} + \omega\tau - \frac{\lambda^a\pi}{2} + \phi_{\Omega^a}^{at.}, \tag{5.34b}$$

$$\arg[M_{cc}^e] = \phi_{\Omega^e}^{XUV} - \omega\tau - \frac{\lambda^e\pi}{2} + \phi_{\Omega^e}^{at.}, \tag{5.34c}$$

where we have the atomic phase for the direct transition $\phi_{\Omega}^{at.} = \eta_L$, the contiuum-continuum transition with absorption of the probe photon $\phi_{\Omega^a}^{at.} = \eta_{\lambda^a} + \phi_{\Omega^a}^{cc,a}$, and one with emission of the probe photon $\phi_{\Omega^e}^{at.} = \eta_{\lambda^e} + \phi_{\Omega^e}^{cc,e}$. Each atomic phase

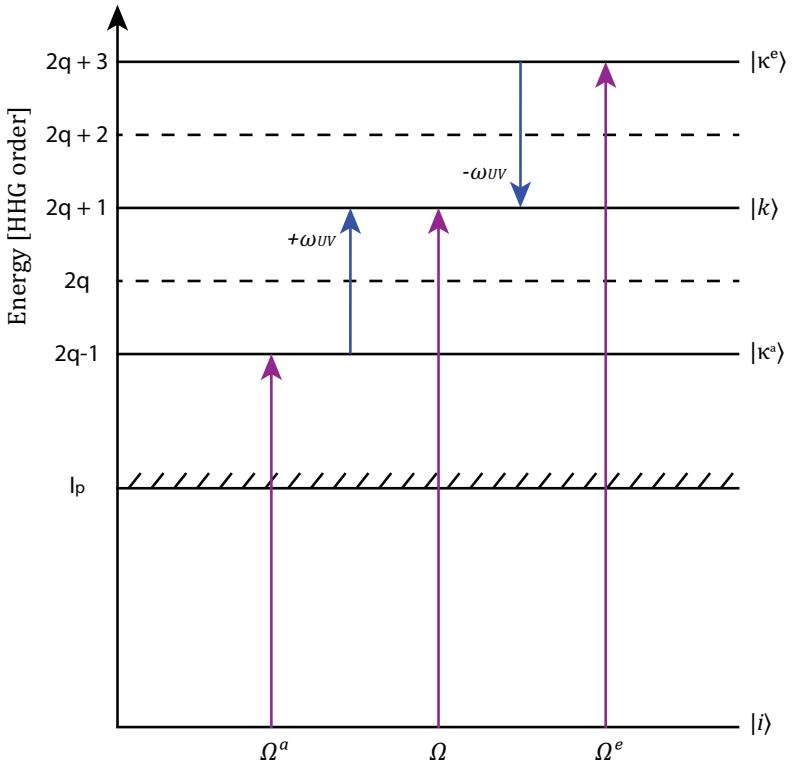

Figure 5.3: Energy diagram for experiment with an odd-harmonics APT dressed by UV pulse. We have three processes that constribute to the photoemission. There is a first, describing a direct transition made by absorption of Ω, a second with absorption of Ω^a and absorption of ω_{UV}, and lastly one occurring with absorption of Ω^e and emission of ω_{UV}.

contains the scattering phase-shift (Wigner phase), but only the atomic phase for two-photon transitions holds a continuum-continuum phase for absorption or emission of the probe photon.

For a given EWP energy, the photoemission probability is expressed as the square of the summation of the coherent paths. For simplicity, only states with $m_i = 0$ will be considered, but the argumentation will hold for other values. For three degenerate quantum paths

$$\begin{aligned} P(k\hat{z},\varepsilon,\tau) &= |M_d(k\hat{z},\varepsilon) + M^a_{cc}(k\hat{z},\varepsilon,\tau) + M^e_{cc}(k\hat{z},\varepsilon,\tau)|^2 \\ &= |M_d|^2 + |M^a_{cc}|^2 + |M^e_{cc}|^2 + (M^*_d M^a_{cc} + M^*_d M^e_{cc} + M^{e*}_{cc} M^a_{cc} + c.c.). \end{aligned} \tag{5.35}$$

This can be rewritten as the sum of three terms

$$P(k\hat{z},\varepsilon,\tau) = I_0(k\hat{z},\varepsilon) + I_\omega(k\hat{z},\varepsilon,\tau) + I_{2\omega}(k\hat{z},\varepsilon,\tau). \tag{5.36}$$

We pay special interest to the $I_\omega(k\hat{z},\varepsilon,\tau)$ term. This modulates according to

$$I_\omega(k\hat{z},\varepsilon,\tau) = 2|M_d|\left(|M^a_{cc}|\cos(\arg[M^*_d M^a_{cc}]) + |M^e_{cc}|\cos(\arg[M^*_d M^e_{cc}])\right) \tag{5.37}$$

The phases of the cosine terms on the right hand side are

$$\arg[M^*_d M^a_{cc}] = \omega\tau + (\phi^{XUV}_{\Omega^a} - \phi^{XUV}_{\Omega}) + (\eta_{\lambda^a} - \eta_L) + \phi^{cc,a}_{\Omega^a} \tag{5.38a}$$

$$\arg[M^*_d M^e_{cc}] = \omega\tau + (\phi^{XUV}_{\Omega} - \phi^{XUV}_{\Omega^e}) + (\eta_L - \eta_{\lambda^e}) - \phi^{cc,e}_{\Omega^e} \tag{5.38b}$$

Using the convention of [114], we can distinguish the relative harmonic phases and atomic phases with $\Delta\phi^{XUV}_{\Omega^a} = \phi^{XUV}_{\Omega^a} - \phi^{XUV}_{\Omega}$ and $\Delta\phi^{XUV}_{\Omega^e} = \phi^{XUV}_{\Omega} - \phi^{XUV}_{\Omega^e}$ whereas $\Delta\phi^{at.}_a = \eta_{\lambda^a} - \eta_L + \phi^{cc,a}_{\Omega^a}$ and $\Delta\phi^{at.}_e = \eta_{\lambda^e} - \eta_L + \phi^{cc,e}_{\Omega^e}$. These are for the special case of Argon with dominant $3p \to \varepsilon d$ transitions ($\lambda = 2$). This leads us to rewriting the equation for $I_\omega(k\hat{z},\varepsilon,\tau)$ as

$$\begin{aligned} I_\omega(k\hat{z},\varepsilon,\tau) =& 2|M_d||M^a_{cc}|\cos(\omega\tau + \Delta\phi^{XUV}_{\Omega^a} + \Delta\phi^{at.}_a) \\ &+ 2|M_d||M^e_{cc}|\cos(\omega\tau + \Delta\phi^{XUV}_{\Omega^e} - \Delta\phi^{at.}_e) \end{aligned} \tag{5.39}$$

or in a more compact way,

$$I_\omega(k\hat{z},\varepsilon,\tau) = A_\varepsilon\cos(\omega\tau + \Psi_\varepsilon). \tag{5.40}$$

The phase Ψ_ε comes from the equation before last is shown now as

$$\Psi_\varepsilon = \text{atan}\left(\frac{|M^a_{cc}|\sin(\Delta\phi^{XUV}_{\Omega^a} + \Delta\phi^{at.}_a) + |M^e_{cc}|\sin(\Delta\phi^{XUV}_{\Omega^e} - \Delta\phi^{at.}_e)}{|M^a_{cc}|\cos(\Delta\phi^{XUV}_{\Omega^a} + \Delta\phi^{at.}_a) + |M^e_{cc}|\cos(\Delta\phi^{XUV}_{\Omega^e} - \Delta\phi^{at.}_e)}\right). \tag{5.41}$$

In similar circumstances where two-photon transitions interfere at a sideband, there are two processes that contribute to the photoemission. This is depicted in Figure 5.4. The first transition occurs by absorption of Ω^a and absorption of ω. The second ocurrs with absorption of Ω^e and emission of ω. The photoemission probability is

$$\begin{aligned} P(k\hat{z},\varepsilon,\tau) &= |M^a_{cc}(k\hat{z},\varepsilon,\tau) + M^e_{cc}(k\hat{z},\varepsilon,\tau)|^2 \\ &= |M^a_{cc}|^2 + |M^a_{cc}|^2 + M^{e*}_{cc}M^a_{cc} + M^{a*}_{cc}M^e_{cc}. \end{aligned} \tag{5.42}$$

We then have only one oscillating term that modulates at twice the probe frequency $I_{2\omega}(k\hat{z},\varepsilon,\tau)$ with definition

$$I_{2\omega}(k\hat{z},\varepsilon,\tau) = 2|M^e_{cc}||M^a_{cc}|\cos(\arg[M^{e*}_{cc}M^a_{cc}]). \tag{5.43}$$

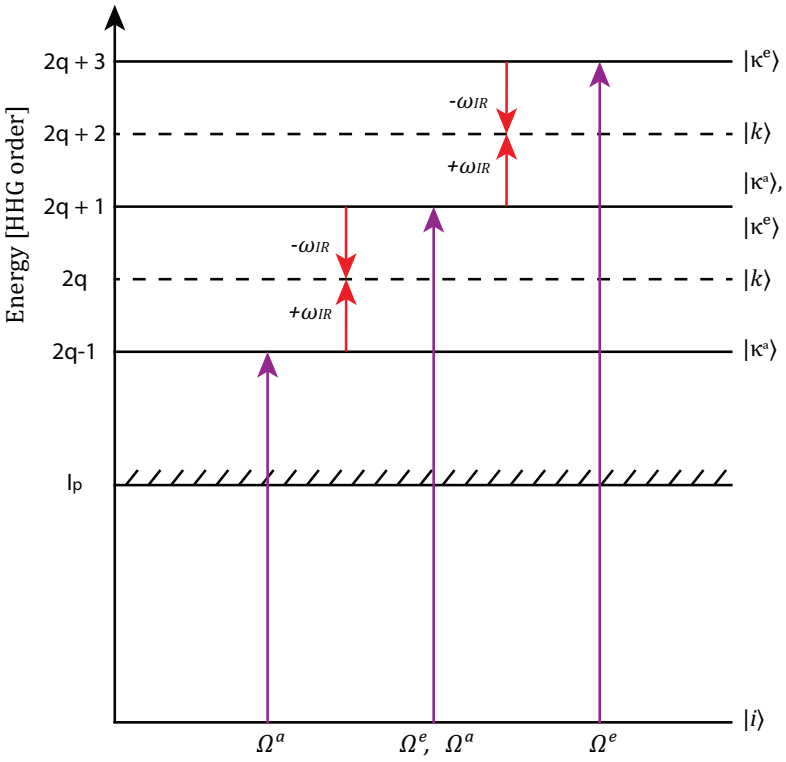

Figure 5.4: Energy diagram for experiment with an odd-harmonics APT dressed by IR pulse. There are two processes that contribute to the photoemission. There is a first, with absorption of Ω^a and absorption of ω_{IR}, and a second occurring with absorption of Ω^e and emission of ω_{IR}. We show two sidebands (dashed black) at $2q$ and $2q+2$ which will be referred to later for our scheme.

We also have an oscillation at twice the probe frequency in Equation 5.35 which is shown in detail in [26, 114, 115]. The phase for this RABBITT sideband is

$$\arg[M_{cc}^{e*} M_{cc}^{a}] = 2\omega\tau + (\phi_{\Omega^a}^{XUV} - \phi_{\Omega^e}^{XUV}) + (\eta_{\lambda^a} - \eta_{\lambda^e}) + (\phi_{\Omega^a}^{cc,a} - \phi_{\Omega^a}^{cc,e}). \tag{5.44}$$

We take an interlude at this point to see how others have measured the atomic phase delays which have been mentioned earlier. The formalism in the above section, and the measurements that are reported below, lay the foundation for us to apply the theory, and set criterion which guide our experiments and analysis.

5.3 Successful Techniques to Isolate the Atomic Phase

Three milestone studies [24, 122, 123] served a didactic role to inspire our measurements. Their experiments, which carried out by the RABBITT methodology, focused on the isolation of the atomic phase so they could extract the Wigner delay. From Equations 5.41 to 5.43, the sideband of a RABBITT spectrogram modulates as

$$I_{2\omega}(\tau) = \alpha + \beta\cos(2\omega_{IR}(\tau + \tau^{XUV} + \tau^{at.})), \tag{5.45}$$

where τ is the controlled pump-probe delay, the spectral delay of the harmonics contributing to the sideband is defined with $\tau^{XUV} = (\phi^{XUV}_{\Omega^a} - \phi^{XUV}_{\Omega^e})/2\omega_{IR}$, and the atomic phase accounts for the delay from the interaction of the harmonic photon and probe photon as $\tau^{at.} = (\eta_{\lambda^a} - \eta_{\lambda^e} + \phi^{cc,a}_{\Omega^a} - \phi^{cc,e}_{\Omega^a})/2\omega_{IR}$. The common strategy of these experiments is to cancel out the ambiguous pump-probe delay as well as the XUV spectral phase. When the atomic delay is all that's left, i.e. $\tau^{at.} = \tau^{W} + \tau^{cc}$, the Wigner delay can be extracted, since τ^{cc} can be calculated from the accurate analytical approximation of Equation 5.31. Although we work on the extraction of the continuum-continuum delay in our work, we can appropriate several of the strategies that will be presented in this section to our experiment.

We consider a first study conducted by Kathrin Klünder et.al. [24] who extracted the difference in single photon ionization between neighboring subshells, 3s and 3p for Argon. Their attosecond harmonics had high enough energy to reach into the deeper 3s shell. There was also small enough bandwidth with just four harmonics (H21 to H27), to avoid overlapping in the photoelectron spectra which were obtained simultaneously in an attosecond pump-probe technique. They made differential measurements by subtracting the phases of two neighboring sidebands. The delay from the attosecond chirp and pump-probe delay were therefore removed from the total phase. Additionally, in order to isolate the Wigner time from the atomic delay, the continuum-continuum delays were calculated. The calculations were made assuming the $3s \rightarrow \epsilon p$ channel in the lower shell, and the $3p \rightarrow \epsilon d$ channel which dominates the much weaker $3p \rightarrow \epsilon d$ in the higher shell [132]. At the three sidebands

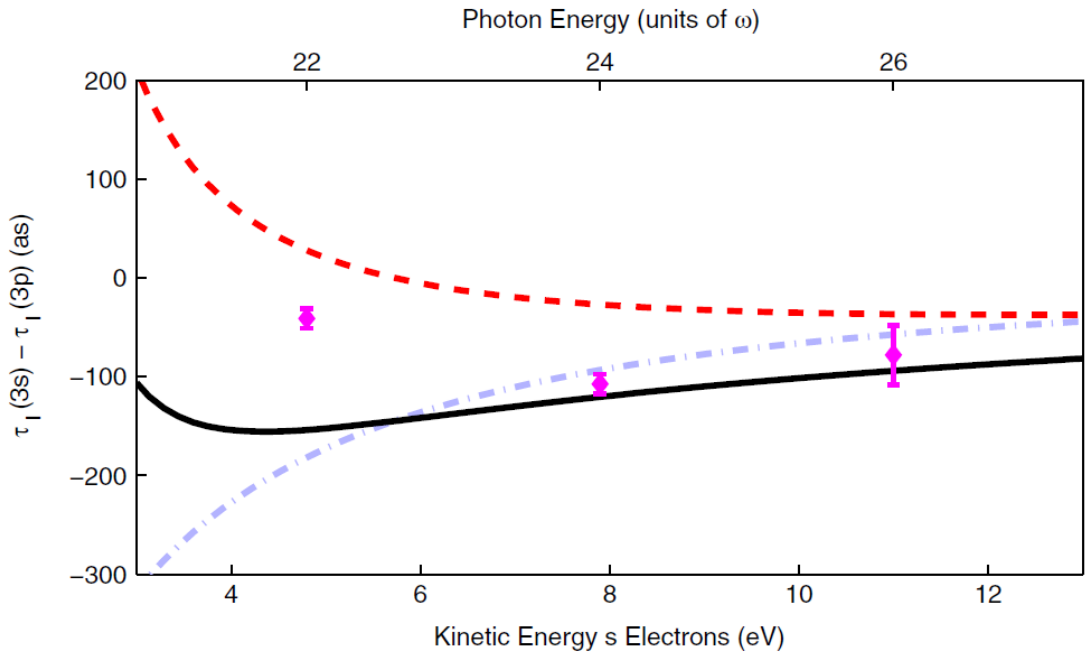

Figure 5.5: Data by Klünder for the Wigner delay differences in Argon across the 3s and 3p shells (diamonds) plotted against calculations (solid black). For comparison, the one-photon delays (red dashed) and continuum-continuum (dash-dotted blue) are plotted. Figure adapted from [24]

they found a ionization delays (includes Wigner delay and continuum-continuum delay) of -40 ± 10 as at SB22, and -110 ± 10 as at SB24 and -80 ± 30 as SB26 - behavior that is displayed in Figure 5.5 (diamonds with error bars). Using these values they could calculate the continuum-continuum delays and obtain the Wigner delays of 140 as at 34 eV, and -20 as at 37 eV and 40 eV.

Another instructive study was performed by Palatchi et.al. [122]. Several pairwise measurements were performed with Helium as a reference gas for Neon, Argon, and Krypton to isolate an "effective" Wigner delay. In angle-resolved measurements, i.e. detection with VMI or COLTRIMS geometry, multiple angular momentum channels are degenerate in the spectrum. When the data is integrated over the detection angle, these contributions are commingled so that the angular momentum dependent Wigner delay is an effective quantity over all emission angles. By subtracting the Helium spectrum, the attochirp was canceled. Furthermore, the simplicity of the Helium system allows for the calculation and subtraction of its

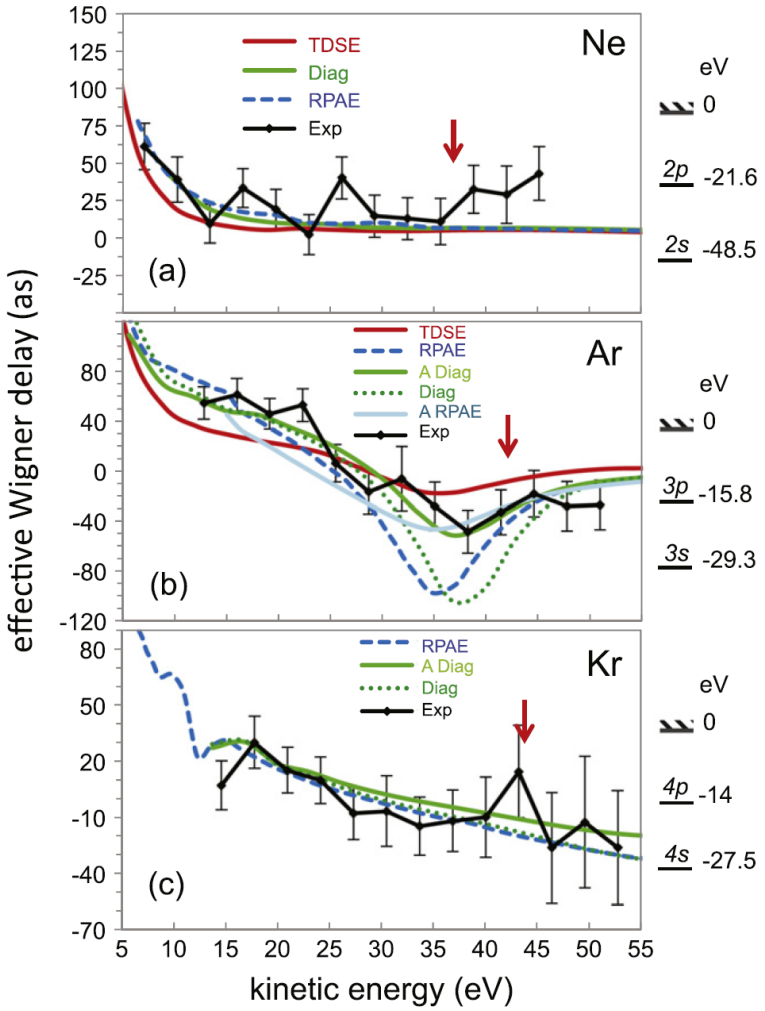

Figure 5.6: Comparison of the effective Wigner delay from experiment and theory for neon, argon and krypton versus photoelectron kinetic energy. The TDSE-SAE, Diag (diagrammatic), and RPAE calculations are from sources external to the author's paper. Calculations labelled with a 'A' in the legend are angle-integrated. Red arrows mark the starting energy region of Helium doubly excited states. Figure adapted from [122]

atomic phase leaving only the paired gas atomic phase left. Their measurements showed remarkable similarity to theoretical calculations which can be seen in Figure 5.6. In this case, the pairs of gases were measured sequentially, and the authors did not utilize active stability to reset the pump-probe delay initial conditions (although it could have been done). Because of an unknown constant phase added, the variation of delay with respect to EWP energy, rather than absolute delay, was reported.

In a third study, which bears similarity to our procedure, Guenot et. al. [123]

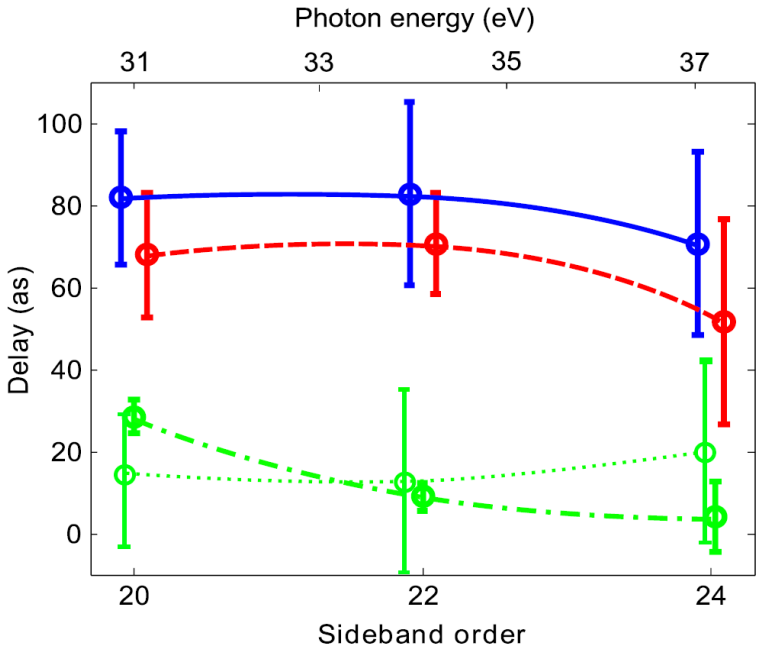

Figure 5.7: Differences of the atomic delay between Ar and He (blue solid), Ar and Ne (red dashed), and Ne and He (green dashed–dotted) as a function of photon energy. The open symbols and green dotted curve are reconstructed delay differences between Ne and He from the difference between Ar and He and Ne and He delays. The data is manually shifted energies for visibility. Figure adapted from [123]

compare the photoemission time delays across different atomic systems. Sequential measurements were performed so that, even though the exact same APT was not guaranteed (as in the simultaneous measurements like that by Klünder), the APT was nearly identical if the measurements were performed in quick succession. Additionally, by taking sequential measurements, the initial conditions of the pump-probe delay had to be reproduced with active control and stabilization. This is possible as long as one carefully counts the cycles of delay, and the beamline optics or pump-probe characteristics are not altered. As seen in Figure 5.7, the differential delays between Argon and Helium, Argon and Neon, and Neon and Helium were obtained to be about 80 as, 70 as, and 20 as respectively.

5.4 Complementary Attosecond Measurements

5.4.1 Experimental Setup

Our experiments were performed at the Auburn Source of Attosecond Pulses (ASAP) laboratory. The schematic of the experimental setup can be seen in [116] and [50] as well as in earlier chapters of this dissertation. It combines a Ti:Sapphire laser delivering linearly-polarized 35-fs, 800-nm pulses at a 10 kHz repetition rate, a stabilized XUV-IR Mach–Zehnder interferometer, VMI, and an XUV spectrometer. APTs made of both odd and even harmonics can be generated with a linearly-polarized two-color (800- and 400-nm) field via high harmonic generation in one arm of the interferometer. A beamsplitter directs part of the laser power to a collinear geometry that, when in use, generates a two-color HHG driving field using a β-barium-borate (BBO) crystal, a calcite plate, and a zeroth-order half-wave plate (at 800 nm). The duration of the 400-nm pulse was not measured directly, but is expected to be slightly longer than the 800-nm pulse. The linearly polarized one or two-color field is focused into a 2-mm gas cell filled with about 10 Torr of argon. The peak intensity at the interaction region is estimated to be $2 \times 10^{14}\mathrm{W/cm}^2$ from the cut-off energy of the high harmonics produced. APTs with an average duration of 10 to 20 fs are formed by filtering out the harmonics below the 11th order with an ultra-thin Al foil.

The other portion of the IR laser power is sent into the other arm of the interferometer, whose total length can be controlled to vary the time delay between the APT and the probe pulses. We also use an optical train for second harmonic generation to convert the IR to a UV probe field. The optics include a BBO, an IR filter to remove any residual IR field, and a half-wave plate to reorient the polarization vertically. I installed these optics on a micrometer stage to move them in and out of the beam path for efficient experiment transitions. We realized the effects of dispersion and reflection losses, which are more problematic at shorter wavelengths. We replaced the gold-coated retroreflector in the beam path with a silver one which has better reflection efficiency over a wider range of wavelengths.

Additionally, I replaced the entrance window of 4-mm thickness to 1-mm thick to reduce the Group Delay Dispersion on the pulse. Both beams were focused, co-axially recombined, and finally sent into a vacuum chamber containing an effusive argon gas jet. At the focal point, the probe intensity is estimated to be below $10^{11}\mathrm{W/cm}^2$. Our home-built VMI system was used to capture the photoelectron emission. The three-dimensional photoelectron momentum distributions were then reconstructed using the DAVIS algorithm [62].

5.4.2 Measurements

In our measurements, we implement two kinds of attosecond pump-probe methodologies. The measurements from each are complementary in that we require them both to isolate the continuum-continuum delays from the atomic phase. We use the traditional RABBITT scheme where an APT composed of odd harmonics of the fundamental IR laser is spatially and temporally overlapped with a probe of the fundamental field at an atomic target. The photoelectron spectrogram we collected for the RABBITT trace is seen in Figure 5.8. In the energy domain, peaks of photoelectrons from the one-photon absorption of odd harmonic photons are observed at an energy spacing of $2\omega_{IR}$. Additionally, sidebands are accessed when the EWPs also absorb or emit an IR photon. This results in a degenerate spectrum at the same sideband continuum state. As the pump-probe delay is changed, the interference modulates at twice the IR frequency.

We also implement a variant of the above scheme that resembles that of [133]. We still have an APT of odd harmonics of the fundamental IR laser. But we now take the UV second harmonic of the IR fundamental as the probe. The peaks from one-photon absorption of odd harmonics are still seen, but sidebands no longer appear. The trace involving this FSI is shown in Figure 5.9. When EWPs absorb or emit a UV photon the energy spans across the energy spacing of the peaks so that the one and two photon transitions all appear at the odd orders. This results in a degenerate spectrum which has components that modulate at ω_{UV} ($2\omega_{IR}$) and $2\omega_{UV}$ ($4\omega_{IR}$). We note that between these two processes, the modulation at ω_{UV}

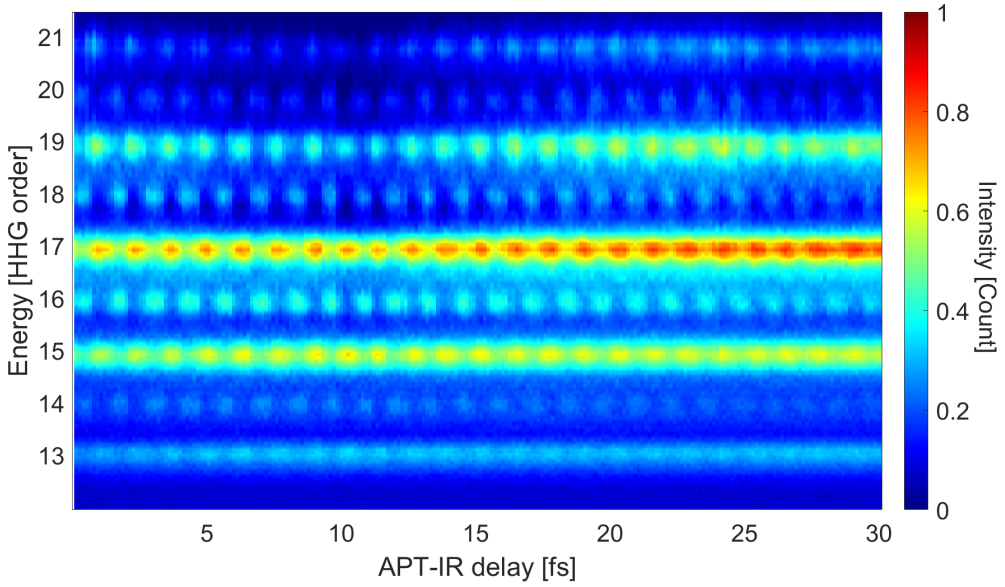

Figure 5.8: Spectrogram for the experiment with an odd-harmonics APT dressed by IR pulse. Photoelectron peaks appear at odd order from the absorption of one XUV photon. Sideband peaks due to two-photon transitions appear at even order, and modulate at twice the IR frequency. A modulation at odd order is due to the depletion of the one-photon paths, conserving the global photoemission.

dominates. This interference involves one less photon and is therefore more probable than the other with transitions that both result from two-photon interactions.

The energies of our harmonic comb are sufficient for one-photon ionization of the Argon 3p electrons. The photon energy range of our five harmonics (H13 to H21) is between 20.1 eV to 29.5 eV, which for the 3p ionization potential of 15.76 eV corresponds to EWP kinetic energies of 4.4 eV to 13.7 eV. We performed the experiments in quick succession so that the characteristics of the APT would be preserved. Only by doing so can we assume that the APT is nearly identical [122].

We made it a practice to begin with the UV-FSI experiment first, because finding the temporal overlap is more difficult in that configuration. In the RABBITT configuration, though, we use the fundamental IR to find the temporal overlap of the beamline. On the other hand, when we use the UV probe we are forced to use the BBO in the HHG arm to aid us. Because we have to rotate the BBO to switch back to a one-color driving field (for odd harmonics) we lose information on the

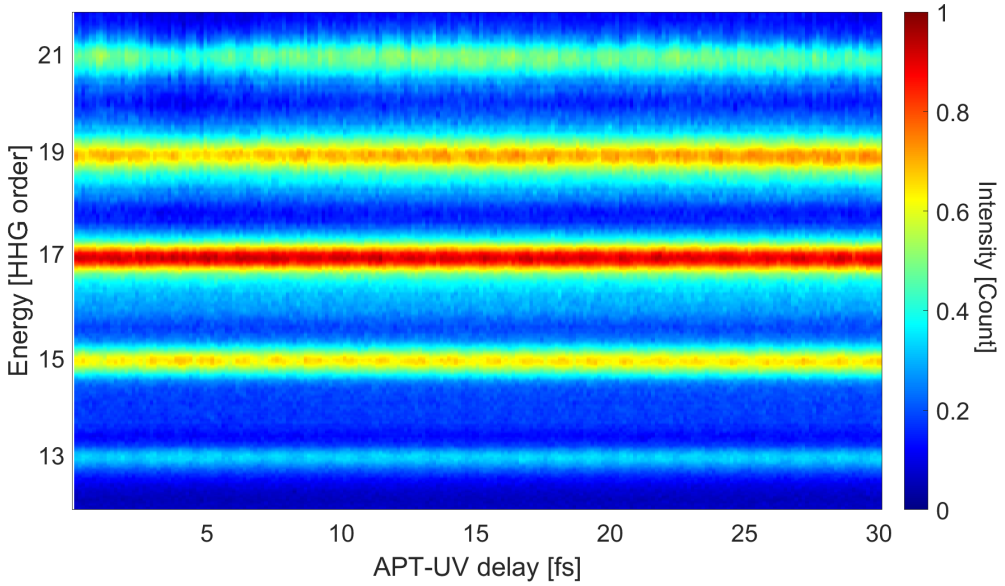

Figure 5.9: Spectrogram for the experiment with an odd-harmonics APT dressed by UV pulse. The degenerate paths of the EWPs all coincide at the odd orders.

optical path length. It is much easier to take the UV-FSI measurement, switch to RABBITT, and even if our calibration is off, scan for temporal overlap again.

5.5 Analysis

5.5.1 Transition Matrix Formalism for Measurements

The angle-resolved photoelectron spectra in attosecond measurements will generally display an anisotropy, coming from the presence of several degenerate angular momentum transition channels[26, 122, 133, 134]. When the measurement is angle-integrated, we should therefore refer to an *effective* Wigner time for all emission angles [122]. The continuum-continuum delay, on the other hand, is universal for an EWP at a given kinetic energy, and given laser wavelength. Therefore, a differential measurement disposes of the group delay of the attosecond pulse (attochirp), pump-probe delay, and effective Wigner delay. We isolate the continuum-continuum absorption versus emission delay as

$$\Delta\tau^{cc,IR} = \frac{(\phi_{\Omega}^{cc,+IR} + \phi_{\Omega}^{cc,-IR})}{2\omega_{IR}}. \tag{5.46}$$

Although we have an addition sign here, the absorption and emission delays are opposite in sign. We can interpret the above equation as the difference in magnitude of delay from absorption versus emission starting from an intermediate EWP kinetic energy. We consider our two measurements, where in one we use an APT composed of odd harmonics dressed by the fundamental (IR) laser pulse, and a second measurement with a practically identical APT dressed by the second harmonic (UV pulse) of the fundamental. In the first measurement, three neighboring harmonics $2q-1$, $2q+1$,and $2q+3$ contribute to two neighboring sidebands $2q$ and $2q+2$ as seen in Figure 5.4. In the lower sideband SB1 (order 2q), we have

$$I_{SB1}(k\hat{z},\varepsilon,\tau) = 2|M^{e}_{2q+1}||M^{a}_{2q-1}|\cos(\Phi_{SB1}) \tag{5.47a}$$

$$\Phi_{SB1} = 2\omega_{IR}\tau + \phi^{XUV}_{2q-1} - \phi^{XUV}_{2q+1} + \eta_{2q-1} - \eta_{2q+1} + \phi^{cc,+IR}_{2q-1} - \phi^{cc,-IR}_{2q+1} + \phi_0, \tag{5.47b}$$

where ϕ_0 is an ambiguous starting pump-probe phase in the IR-RABBITT with respect to the UV-FSI measurement. For the upper sideband SB2 (order 2q+2) we have amplitude and phase

$$I_{SB2}(k\hat{z},\varepsilon,\tau) = 2|M^{e}_{2q+3}||M^{a}_{2q+1}|\cos(\Phi_{SB2}), \tag{5.48a}$$

$$\Phi_{SB2} = 2\omega_{IR}\tau + \phi^{XUV}_{2q+1} - \phi^{XUV}_{2q+3} + \eta_{2q+1} - \eta_{2q+3} + \phi^{cc,+IR}_{2q+1} - \phi^{cc,-IR}_{2q+3} + \phi_0. \tag{5.48b}$$

Returning to the FSI equation where we use a UV probe, we make reference to Figure 5.3 to substitute the appropriate harmonic order into the subscripts. The FSI phase becomes

$$\Psi_{\varepsilon} = \text{atan}\left(\frac{|M^{a}_{2q-1}|\sin(\Delta\phi^{XUV}_{\Omega^a} + \Delta\phi^{at.}_{a}) + |M^{e}_{2q+3}|\sin(\Delta\phi^{XUV}_{\Omega^e} - \Delta\phi^{at.}_{e})}{|M^{a}_{2q-1}|\cos(\Delta\phi^{XUV}_{\Omega^a} + \Delta\phi^{at.}_{a}) + |M^{e}_{2q+3}|\cos(\Delta\phi^{XUV}_{\Omega^e} - \Delta\phi^{at.}_{e})}\right). \tag{5.49}$$

Then, the relative harmonic phases and atomic phases are $\Delta\phi^{XUV}_{\Omega^a} = \phi^{XUV}_{2q-1} - \phi^{XUV}_{2q+1}$ and $\Delta\phi^{XUV}_{\Omega^e} = \phi^{XUV}_{2q+1} - \phi^{XUV}_{2q+3}$ while the atomic phases are $\Delta\phi^{at.}_{a} = \eta_{2q-1} - \eta_{2q+1} + \phi^{cc,+UV}_{2q-1}$ and $\Delta\phi^{at.}_{e} = \eta_{2q+1} - \eta_{2q+3} + \phi^{cc,-UV}_{2q+3}$. We have differentiated between the IR and UV continuum-continuum phases since cc transitions are smaller for shorter wavelengths at a given EWP kinetic energy. In order to build a relation between the IR and UV continuum-continuum phases, we can use

$$\phi^{cc,\pm IR}_{\Omega} = \phi^{cc,\pm UV}_{\Omega} + \delta^{cc,\pm}_{\Omega} \tag{5.50}$$

where we can calculate each of these terms using Equation 5.31. We begin to form a system of equations once we take the difference of the sidebands, and compare this to the FSI with the substitutions $\Delta\phi^a_{FSI} = \Delta\phi^{XUV}_{\Omega^a} + \Delta\phi^{at.}_a$ and $\Delta\phi^e_{FSI} = \Delta\phi^{XUV}_{\Omega^e} - \Delta\phi^{at.}_e$. First, let us rewrite the sideband phases as

$$\Phi_{SB1} = 2\omega_{IR}\tau + \Delta\phi^a_{FSI} - \phi^{cc,-IR}_{2q+1} + \delta^{cc,+}_{2q-1} + \phi_0 \tag{5.51a}$$

$$\Phi_{SB2} = 2\omega_{IR}\tau + \Delta\phi^e_{FSI} + \phi^{cc,+IR}_{2q+1} - \delta^{cc,-}_{2q+3} + \phi_0 \tag{5.51b}$$

Then, as we take the difference of these equations, the pump-probe delay and the ambiguous phase cancels out,

$$\Phi_{SB2} - \Phi_{SB1} = (\Delta\phi^e_{FSI} - \Delta\phi^a_{FSI}) - (\delta^{2q-1}_{cc,+} + \delta^{2q+3}_{cc,-}) + (\phi^{2q+1}_{cc,+IR} + \phi^{2q+1}_{cc,-IR}). \tag{5.52}$$

And, with the FSI equation, we now have a system of two equations and two unknowns

$$\Psi_\varepsilon = \text{atan}\left(\frac{|M^a_{2q-1}|\sin(\Delta\phi^a_{FSI}) + |M^e_{2q+3}|\sin(\Delta\phi^e_{FSI})}{|M^a_{2q-1}|\cos(\Delta\phi^a_{FSI}) + |M^e_{2q+3}|\cos(\Delta\phi^e_{FSI})}\right). \tag{5.53}$$

The form of this equation can be solved by iPROOF [115]. If we calculate the terms $\Delta\phi^e_{FSI}$ and $\Delta\phi^a_{FSI}$ with the iPROOF algorithm, we can thus extract the differential continuum-continuum delay.

5.5.2 The Continuum-Continuum Delays

We can calculate the continuum-continuum delays from an analytical form, for which we refer the reader to [24, 127] for thorough derivations. Briefly, our equation for the phase due to absorption of a probe photon is

$$\phi^{cc,a}_{\Omega^a} = \arg\left[\frac{(2\kappa^a)^{(jZ/\kappa^a)}}{(2k)^{(jZ/k)}}\frac{\Gamma[2 + jZ(1/\kappa^a - 1/k)]}{(\kappa^a - k)^{jZ(1/\kappa^a - 1/k)}}\right]. \tag{5.54}$$

We use atomic units for the calculation, with important conversions including the atomic unit of energy, the hartree, with electron volts $E_h = 27.211386$ [eV] as well as the atomic unit time period in seconds $T_{at.} = 2.418884 \times 10^{-17}$ [s] (about 24.2 [as]). We define the final momentum as $k = \sqrt{2(\Omega^a + I_p + \omega)}$ and the intermediate momentum with $\kappa^a = \sqrt{2(\Omega^a + I_p)}$. Only small changes need to be made for emission, with final momentum equivalently expressed as $k = \sqrt{2(\Omega^e + I_p - \omega)}$,

and intermediate momentum is $\kappa^e = \sqrt{2(\Omega^e + I_p)}$. There is also an alternative to way to write Equation 5.54, presented by Klünder

$$\phi^{cc,a}_{\Omega^a} = \arg\left[\left(\frac{j}{\kappa^a - k}\right)^{jz} \frac{(2\kappa^a)^{j/\kappa^a}}{(2k)^{j/k}}\Gamma(2+jz)\right], \tag{5.55}$$

where $z = 1/\kappa^a - 1/k$. Note that the above equation may appear slightly different to the one reported in [24]. A typo was brought forward by [127] that is included here.

Calculations for the phase and delay are made using the asymptotic approximation, Equation 5.54, and displayed in Figure 5.10. The phase for absorption is positive while the phase for emission is negative. We draw attention to the fact that we are plotting the phase versus the final EWP kinetic energy. in general, transitions higher in energy have smaller magnitude. This is seen in the behavior of both curves - at higher EWP kinetic energy, phase approaches zero. Also this is displayed in the absorption which is a transition from a lower intermediate energy, thus taking longer in magnitude than the emission which comes from a higher intermediate energy. Furthermore, although [127] shows in their Figure 9 that phase and delay magnitude is shorter for shorter wavelengths, our calculations for the UV involve a coupling energy of ω_{UV} rather than $2\omega_{UV}$. Our two equations to calculate the delays for the IR and UV are

$$\tau^{cc,IR} = \left(\phi^{cc,-IR}_{\Omega^e} - \phi^{cc,+IR}_{\Omega^a}\right)/2\omega_{IR}, \tag{5.56a}$$

$$\tau^{cc,UV} = \left(\phi^{cc,-UV}_{\Omega^e} - \phi^{cc,+IR}_{\Omega^a}\right)/\omega_{UV}, \tag{5.56b}$$

where Equation 5.56.a is for the RABBITT (coupling energy of twice the probe frequency) and Equation 5.56.b is for the FSI (coupling energy of the probe energy). The asymptotic approximation slightly overestimates the magnitude of the phase, at low EWP energies, but converges toward exact calculations at higher energy [127]. Overall, it is a good qualitative model. When we make the calculations, we do so with atomic units.

If we recall Equation 5.46, we can see that it is more practical to calculate and plot the delays with respect to the intermediate EWP kinetic energy. We note an interesting behavior of the curves of Figure 5.11.a with comparison to

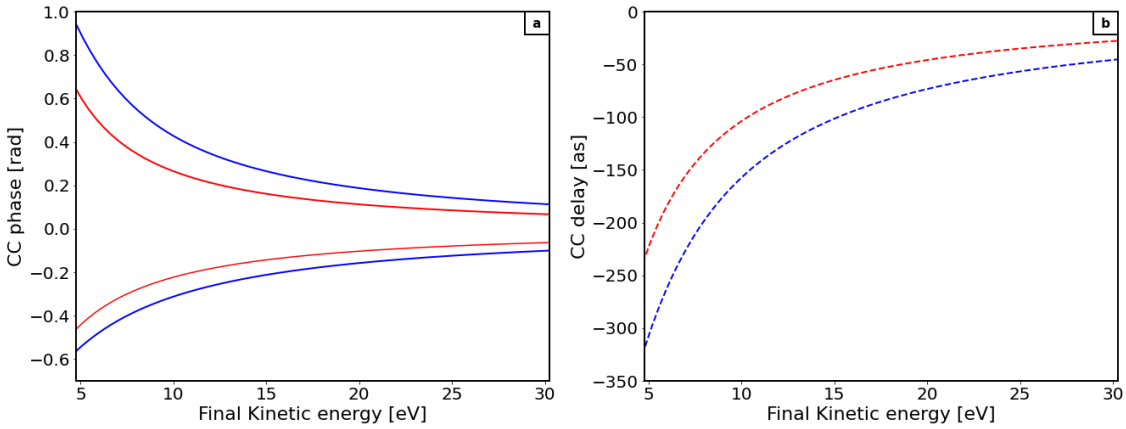

Figure 5.10: Calculations of the Continuum-continuum phases and delays at final EWP kinetic energy. The results can be compared to [127]. The positive/negative curves are for absorption/emission. The blue is for the UV and the red is for the IR. The dashed lines represent the delays of Equations 5.56.a and 5.56.b. The UV phase and delays are longer in this case because the coupling energy is ω_{UV} (for the FSI) rather than $2\omega_{UV}$ (for RABBITT).

those in 5.10.a. The absorption/emission is still positive/negative. But now, we consider delays departing from an intermediate EWP kinetic energy state to a higher EWP final energy with absorption, and a drop to a lower final energy with emission. This means that the absorption, being across a higher energy band in this instance, takes less time.

Finally, we consider the results. We refer the reader to [115] for a disclosure on the iPROOF algorithm, but with the obtained phases, we have used Equation 5.52, and 5.46 to calculate the delays of absorption and emission from a given intermediate kinetic energy. We note that iPROOF was originally designed to treat the case of an IR fundamental probe and an XUV spectrum with odd and even harmonics. We thus had to trick the algorithm by treating the UV probe as the fundamental, and the IR odd harmonics as the odd and even harmonics of the UV. Our data is presented in Figure 5.11.b at harmonic orders H15, H17, and H19. We note that the error stems from the uncertainty in the width of the five harmonic pulses in our APT (H13 - H21). These errors, as well as the FSI phases $\Delta\phi^a_{FSI}$ and

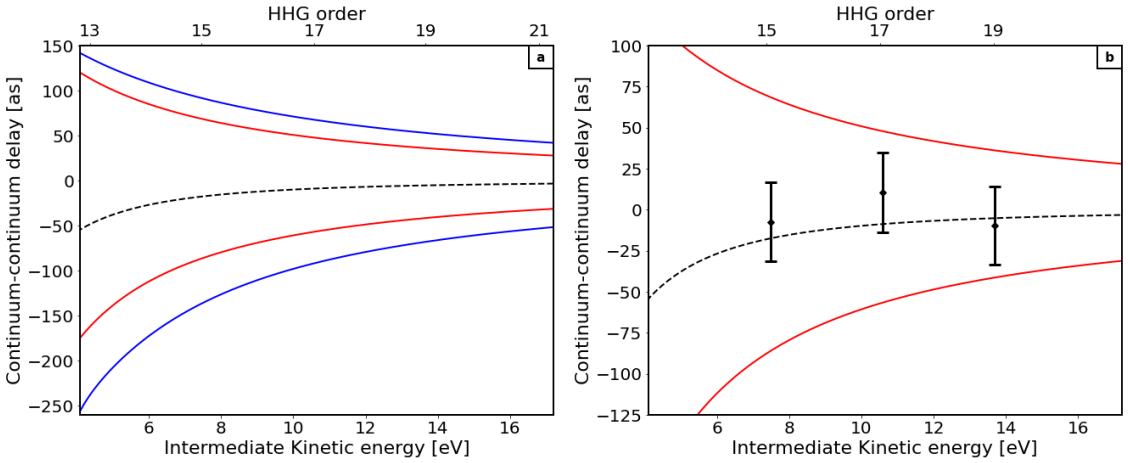

Figure 5.11: Calculations of the Continuum-continuum phases at intermediate EWP kinetic energies for our experiments. We use the same color code as in Figure 5.10, and the dashed black lines are the calculations for Equation 5.46. The black diamonds represent our data with error bars that come from uncertainties as described in the text.

$\Delta\phi^{e}_{FSI}$ are both obtained from iPROOF. We are excited that this measurement is, to our knowledge, the first experimental validation of the continuum-continuum delays.

From the asymptotic approximation, I calculate that the delay magnitude differences should be -17.5 as at H15, -8.7 as at H17, and -5.1 as at H19. Our delays obtained from the experiment are, -7.4 ± 24.1 as for H15, 10.6 ± 24.5 as for H17, and -9.7 ± 23.8 as for H19. A first source of our error comes from the dynamic stability of our active stabilization system which stabilizes and controls the delay of the interferometer. In [116] we have found this to be about 6 as. We also account for the error from the sideband modulations. We have a measurement of about 29.38 fs for the RABBITT, which is roughly 22.04 oscillations of the interference. In the Fourier domain, our interference signal is thus not a pure frequency f_0. I estimate the deviation by using the frequency $f_{dev.}$ at the half-width at half-maximum of the frequency peak. Next, I estimate the difference in absolute delay of what we assume is the actual interference frequency f_0 compared to the deviated frequency f_{dev}. From $22.035 \times (1/f_0 - 1/f_{dev.})$ I use the value of about 7.4 as. Since each of the four sidebands is the same length, I use this error for every instance a sideband appears in the calculations. Another source of error comes from the FSI terms. Because we

have modulations from both one and two-photon quantum paths overlapping, this is a more complex situation. The iPROOF algorithm performs the analysis across the width of the pulse, and the error is obtained from this set of values. Finally, in our analysis we have use theoretical values which come from the asymptotic approximation. We already know that this approximation begins to break down at lower energies, but it still provides us with good qualitative behaviour. At this point, we await results from theoretical calculations so that we can better estimate the continuum-continuum delays. We do not have a designated value for this error, but we can speculate that it may be in the form of a shift subject to the qualitative nature of the approximation used.

Surely, one of the biggest reasons our data may depart from perfect agreement is that the asymptotic approximation breaks down close to ionization threshold. Additionally, it may be possible that increased error may arise from the fact that the APT is not identical, but nearly identical in the sequential measurements. We may have a few more sources of error due to things such as spectrometer calibrations, but I am confident that the dominant forms of error are accounted for. Although we currently have no external measurements to compare our continuum-continuum results with, we can consider the results for the Wigner-like delay by Klünder as a standard of comparison. It is, after all, a related experiment of the other part of the atomic delay. Our measurement, like Klünder's, displays a qualitative agreement with the physical models.

5.6 Conclusion

In conclusion, we have measured the temporal aspects of a part of the atomic delay, the continuum-continuum delay, for the first time. We used complementary measurements to isolate it in a differential way. We anticipate that this work will deliver new insights for the attosecond community. These results may also serve as data to compare to theoretical work that is made with more exact calculations. We make the observation that it should be rewarding to repeat this experiment using Helium, for which theoretical support can be made with more precision.

6
Conclusions

Contents

What follows is a summary of the work and scholarly activities presented in this dissertation. I conclude with my personal outlook for the directions of attosecond science. It is my hope that in drawing the main thoughts together in one place, and sharing a personal perspective, that future readers will draw some inspiration.

6.1 Summary

The accomplishments and scholarly pursuits recorded in this dissertation sweep territories branching across several areas in the field of attosecond science. Part of the reason for this is that, in the startup of a new research line, opportunities to apply forward thinking were taken as each individual stage of the experimental setup was developed. For example, even though plenty of algorithm techniques exist for the inversion of PADs, in a work led by Geoffrey Harrison, the faster and higher resolution DAVIS algorithm was developed. The project I led to design and implement an active stabilization scheme was also another project that produced

and shared as a novel scientific contribution. So, the first few years of our group have been spent efficiently in that a new attosecond research line was developed while research was carried out in the process.

Chapter 1 is organized so that the reader may be imbued with the customary knowledge required in the attosecond community, while also being prepared for the studies that were undertaken in photoemission coherent control and fundamental light-matter interactions in atomic physics. In Chapter 2, a detailed description of the attosecond beamline is presented, providing as much practical information and details as possible about our experimental capabilities at the given time of these experiments. In Chapter 3, I took space to recount a novel technique for active stabilization of our pump-probe scheme that meets and exceeds some of the highest standards for precision and control possible for comparable setups. In Chapter 4, I recall a study of the control of photoemission. Finally, in Chapter 5, I present the theoretical motivation and experimental results that displays a promising outlook for a new method that can allow the extraction of fundamental atomic physics involved in light-matter interaction.

6.2 Outlook

Attosecond science has reached a stage of maturity where the community has realized that parametric studies are as important as pump-probe experiments that simply control the delay between APTs or SAPs and the probe field. We have found ways to tailor the harmonic spectrum by altering the harmonic generation with steps before, during, and after HHG. We have studied all phases of matter - gas, liquid, solid, and plasma. We have studied inorganic, organic, and biological materials. We have a variety of methods including attosecond streaking, RABBITT, Attosecond lighthouse, Attosecond time-slit, stereo ATI, etc. We have found that we can study ultrafast electronic shakeup, Auger Decay, the Fano resonance, Wigner delays, timescales of continuum-continuum transitions, and self probing in High Harmonic spectroscopy. And, quite recently, we have obtained the means both

to produce zeptosecond pulses, and even carry out attosecond-pump/attosecond-probe experiments. Our past and present have been brilliant, and our future looks bright as well.

For most of the attosecond community, the year 2020 has been a year of far reaching efforts as never before (despite the relentless COVID-19 pandemic and economic uncertainties). I believe that many eureka moments are in store for industrial applications and controlling the processes and outcomes in basic atomic physics and chemistry. It seems reasonable that future studies involving attosecond pump-attosecond probe techniques should be capable of penetrating far into the inner shell regions of the types of systems which have already been studied as well as into the 100-eV range of experiments [135–137]. Even with the current ultrafast methodologies widely in use, perhaps new ways for interrogation wait to be discovered as well. Perhaps we can also study transient processes which are not themselves induced by the attosecond pulses - one example being phase change of materials. Still, even now, the attosecond science has more than enough open frontier to explore.

If I have seen further, it is by standing on the shoulders of Giants.

— Sir Isaac Newton in a letter to Robert Hooke

References

[1] Adrian L Cavalieri, Norbert Müller, Th Uphues, Vladislav S Yakovlev, Andrius Baltuška, Balint Horvath, B Schmidt, L Blümel, R Holzwarth, Stefan Hendel, et al. "Attosecond spectroscopy in condensed matter". In: *Nature* 449.7165 (2007), pp. 1029–1032.

[2] Inga Jordan, Martin Huppert, Dominik Rattenbacher, Michael Peper, Denis Jelovina, Conaill Perry, Aaron von Conta, Axel Schild, and Hans Jakob Wörner. "Attosecond spectroscopy of liquid water". In: *Science* 369.6506 (2020), pp. 974–979.

[3] Alexander I Kuleff and Lorenz S Cederbaum. "Ultrafast correlation-driven electron dynamics". In: *Journal of Physics B: Atomic, Molecular and Optical Physics* 47.12 (2014), p. 124002.

[4] Sarah Maria Falke, Carlo Andrea Rozzi, Daniele Brida, Margherita Maiuri, Michele Amato, Ephraim Sommer, Antonietta De Sio, Angel Rubio, Giulio Cerullo, Elisa Molinari, et al. "Coherent ultrafast charge transfer in an organic photovoltaic blend". In: *Science* 344.6187 (2014), pp. 1001–1005.

[5] Jean-Claude Diels and Wolfgang Rudolph. *Ultrashort laser pulse phenomena*. Elsevier, 2006.

[6] Orazio Svelto and David C Hanna. *Principles of lasers*. Vol. 1. Springer, 2010.

[7] Pierre-Marie Paul, Elena S Toma, Pierre Breger, Genevive Mullot, Frédérika Augé, Ph Balcou, Harm Geert Muller, and Pierre Agostini. "Observation of a train of attosecond pulses from high harmonic generation". In: *Science* 292.5522 (2001), pp. 1689–1692.

[8] Zenghu Chang. "Chirp of the single attosecond pulse generated by a polarization gating". In: *Physical Review A* 71.2 (2005), p. 023813.

[9] Zenghu Chang. "Controlling attosecond pulse generation with a double optical gating". In: *Physical Review A* 76.5 (2007), p. 051403.

[10] Paul B Corkum. "Plasma perspective on strong field multiphoton ionization". In: *Physical review letters* 71.13 (1993), p. 1994.

[11] Maciej Lewenstein, Ph Balcou, M Yu Ivanov, Anne L'huillier, and Paul B Corkum. "Theory of high-harmonic generation by low-frequency laser fields". In: *Physical Review A* 49.3 (1994), p. 2117.

[12] M Ferray, Anne L'Huillier, XF Li, LA Lompre, G Mainfray, and C Manus. "Multiple-harmonic conversion of 1064 nm radiation in rare gases". In: *Journal of Physics B: Atomic, Molecular and Optical Physics* 21.3 (1988), p. L31.

[13] Zenghu Chang. *Fundamentals of attosecond optics*. CRC press, 2011.

[14] LV Keldysh et al. "Ionization in the field of a strong electromagnetic wave". In: *Sov. Phys. JETP* 20.5 (1965), pp. 1307–1314.

[15] Anh-Thu Le, Hui Wei, Cheng Jin, and CD Lin. "Strong-field approximation and its extension for high-order harmonic generation with mid-infrared lasers". In: *Journal of Physics B: Atomic, Molecular and Optical Physics* 49.5 (2016), p. 053001.

[16] J Itatani, F Quéré, Gennady L Yudin, M Yu Ivanov, Ferenc Krausz, and Paul B Corkum. "Attosecond streak camera". In: *Physical review letters* 88.17 (2002), p. 173903.

[17] M Hentschel, R Kienberger, Ch Spielmann, Georg A Reider, N Milosevic, Thomas Brabec, Paul Corkum, Ulrich Heinzmann, Markus Drescher, and Ferenc Krausz. "Attosecond metrology". In: *Nature* 414.6863 (2001), pp. 509–513.

[18] H _ G Muller. "Reconstruction of attosecond harmonic beating by interference of two-photon transitions". In: *Applied Physics B* 74.1 (2002), s17–s21.

[19] M Isinger, D Busto, S Mikaelsson, S Zhong, C Guo, P Salières, CL Arnold, A l'Huillier, and M Gisselbrecht. "Accuracy and precision of the RABBIT technique". In: *Philosophical Transactions of the Royal Society A* 377.2145 (2019), p. 20170475.

[20] Laura Cattaneo, Johanna Vos, Matteo Lucchini, L Gallmann, C Cirelli, and Ursula Keller. "Comparison of attosecond streaking and RABBITT". In: *Optics express* 24.25 (2016), pp. 29060–29076.

[21] Markus Drescher, Michael Hentschel, R Kienberger, Matthias Uiberacker, Vladislav Yakovlev, Armin Scrinzi, Th Westerwalbesloh, U Kleineberg, Ulrich Heinzmann, and Ferenc Krausz. "Time-resolved atomic inner-shell spectroscopy". In: *Nature* 419.6909 (2002), pp. 803–807.

[22] Matthias Uiberacker, Th Uphues, Martin Schultze, Aart Johannes Verhoef, Vladislav Yakovlev, Matthias F Kling, Jens Rauschenberger, Nicolai M Kabachnik, Hartmut Schröder, Matthias Lezius, et al. "Attosecond real-time observation of electron tunnelling in atoms". In: *Nature* 446.7136 (2007), pp. 627–632.

[23] Eugene P Wigner. "Lower limit for the energy derivative of the scattering phase shift". In: *Physical Review* 98.1 (1955), p. 145.

[24] Kathrin Klünder, JM Dahlström, Mathieu Gisselbrecht, Thomas Fordell, Marko Swoboda, Diego Guenot, Per Johnsson, Jérémie Caillat, Johan Mauritsson, A Maquet, et al. "Probing single-photon ionization on the attosecond time scale". In: *Physical Review Letters* 106.14 (2011), p. 143002.

[25] Johan Mauritsson, Per Johnsson, Erik Mansten, Marko Swoboda, Thierry Ruchon, Anne L'Huillier, and KJ Schafer. "Coherent electron scattering captured by an attosecond quantum stroboscope". In: *Physical Review Letters* 100.7 (2008), p. 073003.

[26] Guillaume Laurent, Wei Cao, H Li, Zhenhua Wang, Itzik Ben-Itzhak, and Charles L Cocke. "Attosecond control of orbital parity mix interferences and the relative phase of even and odd harmonics in an attosecond pulse train". In: *Physical Review Letters* 109.8 (2012), p. 083001.

[27] Michael Chini, Hiroki Mashiko, He Wang, Shouyuan Chen, Chenxia Yun, Shane Scott, Steve Gilbertson, and Zenghu Chang. "Delay control in attosecond pump-probe experiments". In: *Optics express* 17.24 (2009), pp. 21459–21464.

[28] Martin Huppert, Inga Jordan, and Hans Jakob Wörner. "Attosecond beamline with actively stabilized and spatially separated beam paths". In: *Review of Scientific Instruments* 86.12 (2015), p. 123106.

[29] A Zaır, E Mével, E Cormier, and Eric Constant. "Ultrastable collinear delay control setup for attosecond IR-XUV pump–probe experiment". In: *JOSA B* 35.5 (2018), A110–A115.

[30] Theodore H Maiman. "Stimulated optical radiation in ruby". In: *nature* 187.4736 (1960), pp. 493–494.

[31] FJ McClung and RW Hellwarth. "Giant optical pulsations from ruby". In: *Journal of Applied Physics* 33.3 (1962), pp. 828–829.

[32] LE Hargrove, Richard L Fork, and MA Pollack. "Locking of He–Ne laser modes induced by synchronous intracavity modulation". In: *Applied Physics Letters* 5.1 (1964), pp. 4–5.

[33] WC Wiley and Ii H McLaren. "Time-of-flight mass spectrometer with improved resolution". In: *Review of scientific instruments* 26.12 (1955), pp. 1150–1157.

[34] Alexander Kothe, Jan Metje, Martin Wilke, Alexandre Moguilevski, Nicholas Engel, Ruba Al-Obaidi, Clemens Richter, Ronny Golnak, Igor Yu Kiyan, and Emad F Aziz. "Time-of-flight electron spectrometer for a broad range of kinetic energies". In: *Review of Scientific Instruments* 84.2 (2013), p. 023106.

[35] Reinhard Dörner, Volker Mergel, Ottmar Jagutzki, Lutz Spielberger, Joachim Ullrich, Robert Moshammer, and Horst Schmidt-Böcking. "Cold target recoil ion momentum spectroscopy: a 'momentum microscope'to view atomic collision dynamics". In: *Physics Reports* 330.2-3 (2000), pp. 95–192.

[36] Etienne Gagnon, Arvinder S Sandhu, Ariel Paul, Kim Hagen, Achim Czasch, Till Jahnke, Predrag Ranitovic, C Lewis Cocke, Barry Walker, Margaret M Murnane, et al. "Time-resolved momentum imaging system for molecular dynamics studies using a tabletop ultrafast extreme-ultraviolet light source". In: *Review of Scientific Instruments* 79.6 (2008), p. 063102.

[37] André TJB Eppink and David H Parker. "Velocity map imaging of ions and electrons using electrostatic lenses: Application in photoelectron and photofragment ion imaging of molecular oxygen". In: *Review of Scientific Instruments* 68.9 (1997), pp. 3477–3484.

[38] GR Fleming and GS Beddard. "CW mode-locked dye lasers for ultra fast spectroscopic studies". In: *Optics & Laser Technology* 10.5 (1978), pp. 257–264.

[39] David E Spence, P Np Kean, and Wilson Sibbett. "60-fsec pulse generation from a self-mode-locked Ti: sapphire laser". In: *Optics letters* 16.1 (1991), pp. 42–44.

[40] Webb Hooker. *Laser Physics*. Vol. 1. Oxford University Press, 2010.

[41] F Canova, J-P Chambaret, G Mourou, Marc Sentis, Olivier Uteza, Philippe Delaporte, Tatiana Itina, J-Y Natoli, Mireille Commandre, and Claude Amra. "Complete characterization of damage threshold in titanium doped sapphire crystals with nanosecond, picosecond, and femtosecond laser pulses". In: *Laser-Induced Damage in Optical Materials: 2005*. Vol. 5991. International Society for Optics and Photonics. 2006, p. 599123.

[42] Donna Strickland and Gerard Mourou. "Compression of amplified chirped optical pulses". In: *Optics communications* 56.3 (1985), pp. 219–221.

[43] Klaas Wynne, Gavin D Reid, and Robin M Hochstrasser. "Regenerative amplification of 30-fs pulses in Ti: sapphire at 5 kHz". In: *Optics letters* 19.12 (1994), pp. 895–897.

[44] Giuseppe Sansone, Enrico Benedetti, Francesca Calegari, Caterina Vozzi, Lorenzo Avaldi, Roberto Flammini, Luca Poletto, P Villoresi, C Altucci, R Velotta, et al. "Isolated single-cycle attosecond pulses". In: *Science* 314.5798 (2006), pp. 443–446.

[45] Olivier Tcherbakoff, E Mével, D Descamps, J Plumridge, and E Constant. "Time-gated high-order harmonic generation". In: *Physical Review A* 68.4 (2003), p. 043804.

[46] Chuangtian Chen, Bochang Wu, Aidong Jiang, and Guiming You. "A New-Type Ultraviolet SHG Crystal——β-BaB 2 O 4". In: *Science in China Series B-Chemistry, Biological, Agricultural, Medical & Earth Sciences* 28.3 (1985), pp. 235–243.

[47] Robert W Boyd. "The nonlinear optical susceptibility". In: *Nonlinear optics* 3 (2008), pp. 1–67.

[48] Shinichi Imai, Toshitaka Yamada, Yasutomo Fujimori, and Ken Ishikawa. "Third-harmonic generation of an alexandrite laser in β-BaB2O4". In: *Applied physics letters* 54.13 (1989), pp. 1206–1208.

[49] GG Paulus, W Nicklich, Huale Xu, P Lambropoulos, and H Walther. "Plateau in above threshold ionization spectra". In: *Physical review letters* 72.18 (1994), p. 2851.

[50] B Unzicker and G Laurent. "Electron choreography". In: *New Journal of Physics* 72.18 (2020), p. 2851.

[51] XF Li, A L'Huillier, M Ferray, LA Lompré, and G Mainfray. "Multiple-harmonic generation in rare gases at high laser intensity". In: *Physical Review A* 39.11 (1989), p. 5751.

[52] Aleksandar D Rakić. "Algorithm for the determination of intrinsic optical constants of metal films: application to aluminum". In: *Applied optics* 34.22 (1995), pp. 4755–4767.

[53] SM Candel. "An algorithm for the Fourier-Bessel transform". In: *Computer physics communications* 23.4 (1981), pp. 343–353.

[54] Yoshihiro Sato, Yutaka Matsumi, Masahiro Kawasaki, Koichi Tsukiyama, and Richard Bersohn. "Ion Imaging of the Photodissociation of OCS Near 217 and 230 nm". In: *The Journal of Physical Chemistry* 99.44 (1995), pp. 16307–16314.

[55] Marc JJ Vrakking. "An iterative procedure for the inversion of two-dimensional ion/photoelectron imaging experiments". In: *Review of Scientific Instruments* 72.11 (2001), pp. 4084–4089.

[56] Vladimir Dribinski, Alexei Ossadtchi, Vladimir A Mandelshtam, and Hanna Reisler. "Reconstruction of Abel-transformable images: The Gaussian basis-set expansion Abel transform method". In: *Review of Scientific Instruments* 73.7 (2002), pp. 2634–2642.

[57] NG Kling, D Paul, A Gura, G Laurent, S De, H Li, Z Wang, B Ahn, CH Kim, TK Kim, et al. "Thick-lens velocity-map imaging spectrometer with high resolution for high-energy charged particles". In: *Journal of Instrumentation* 9.05 (2014), P05005.

[58] MF Kling, J Rauschenberger, AJ Verhoef, E Hasović, T Uphues, DB Milošević, HG Muller, and MJJ Vrakking. "Imaging of carrier-envelope phase effects in above-threshold ionization with intense few-cycle laser fields". In: *New Journal of Physics* 10.2 (2008), p. 025024.

[59] MF Kling, Ch Siedschlag, Aart J Verhoef, JI Khan, Martin Schultze, Th Uphues, Yicheng Ni, Matthias Uiberacker, M Drescher, Ferenc Krausz, et al. "Control of electron localization in molecular dissociation". In: *Science* 312.5771 (2006), pp. 246–248.

[60] Sergey Zherebtsov, Thomas Fennel, Jürgen Plenge, Egill Antonsson, Irina Znakovskaya, Adrian Wirth, Oliver Herrwerth, Frederik Süßmann, Christian Peltz, Izhar Ahmad, et al. "Controlled near-field enhanced electron acceleration from dielectric nanospheres with intense few-cycle laser fields". In: *Nature Physics* 7.8 (2011), pp. 656–662.

[61] Joachim Ullrich, Robert Moshammer, Alexander Dorn, Reinhard Dörner, L Ph H Schmidt, and H Schmidt-Böcking. "Recoil-ion and electron momentum spectroscopy: reaction-microscopes". In: *Reports on Progress in Physics* 66.9 (2003), p. 1463.

[62] GR Harrison, JC Vaughan, B Hidle, and GM Laurent. "DAVIS: A direct algorithm for velocity-map imaging system". In: *The Journal of Chemical Physics* 148.19 (2018), p. 194101.

[63] O Ghafur, W Siu, Per Johnsson, Matthias F Kling, M Drescher, and MJJ Vrakking. "A velocity map imaging detector with an integrated gas injection system". In: *Review of Scientific Instruments* 80.3 (2009), p. 033110.

[64] Frederik Süßmann, Sergey Zherebtsov, J Plenge, Nora G Johnson, Matthias Kübel, AM Sayler, V Mondes, C Graf, E Rühl, GG Paulus, et al. "Single-shot velocity-map imaging of attosecond light-field control at kilohertz rate". In: *Review of Scientific Instruments* 82.9 (2011), p. 093109.

[65] Pradrag Ranitovic, XM Tong, B Gramkow, S De, B DePaola, KP Singh, W Cao, Maia Magrakvelidze, Dipanwita Ray, I Bocharova, et al. "IR-assisted ionization of helium by attosecond extreme ultraviolet radiation". In: *New Journal of Physics* 12.1 (2010), p. 013008.

[66] Gustavo A Garcia, Laurent Nahon, and Ivan Powis. "Two-dimensional charged particle image inversion using a polar basis function expansion". In: *Review of Scientific Instruments* 75.11 (2004), pp. 4989–4996.

[67] RN Zare. *Angular Momentum: Understanding Spatial Aspects in Chemistry and Physics*. Vol. 1. Wiley, 1988.

[68] K Reid. "Photoelectron angular distributions". In: *Annual Review of Physical Chemistry* 54.397 (2003), pp. 4989–4996.

[69] Martin Schultze, Markus Fieß, Nicholas Karpowicz, Justin Gagnon, Michael Korbman, Michael Hofstetter, S Neppl, Adrian L Cavalieri, Yannis Komninos, Th Mercouris, et al. "Delay in photoemission". In: *science* 328.5986 (2010), pp. 1658–1662.

[70] FM Böttcher, B Manschwetus, H Rottke, N Zhavoronkov, Z Ansari, and W Sandner. "Interferometric long-term stabilization of a delay line: a tool for pump–probe photoelectron–photoion-coincidence spectroscopy on the attosecond time scale". In: *Applied Physics B* 91.2 (2008), pp. 287–293.

[71] GIUSEPPE Sansone, ENRICO Benedetti, JP Caumes, SALVATORE Stagira, CATERINA Vozzi, MAURO Nisoli, L Poletto, P Villoresi, V Strelkov, I Sola, et al. "Shaping of attosecond pulses by phase-stabilized polarization gating". In: *Physical Review A* 80.6 (2009), p. 063837.

[72] Ximao Feng, Steve Gilbertson, Hiroki Mashiko, He Wang, Sabih D Khan, Michael Chini, Yi Wu, Kun Zhao, and Zenghu Chang. "Generation of isolated attosecond pulses with 20 to 28 femtosecond lasers". In: *Physical review letters* 103.18 (2009), p. 183901.

[73] Torsten Leitner, Richard Taıeb, Michael Meyer, and Philippe Wernet. "Probing photoelectron angular distributions in molecules with polarization-controlled two-color above-threshold ionization". In: *Physical Review A* 91.6 (2015), p. 063411.

[74] R Locher, Matteo Lucchini, J Herrmann, M Sabbar, M Weger, A Ludwig, L Castiglioni, M Greif, M Hengsberger, L Gallmann, et al. "Versatile attosecond beamline in a two-foci configuration for simultaneous time-resolved measurements". In: *Review of Scientific Instruments* 85.1 (2014), p. 013113.

[75] Markus Fieß, Martin Schultze, Eleftherios Goulielmakis, B Dennhardt, Justin Gagnon, Michael Hofstetter, Reinhard Kienberger, and Ferenc Krausz. "Versatile apparatus for attosecond metrology and spectroscopy". In: *Review of Scientific Instruments* 81.9 (2010), p. 093103.

[76] Hiroki Mashiko, M Justine Bell, Annelise R Beck, Mark J Abel, Philip M Nagel, Colby P Steiner, Joseph Robinson, Daniel M Neumark, and Stephen R Leone. "Tunable frequency-controlled isolated attosecond pulses characterized by either 750 nm or 400 nm wavelength streak fields". In: *Optics express* 18.25 (2010), pp. 25887–25895.

[77] L Lepetit, G Chériaux, and M Joffre. "Linear techniques of phase measurement by femtosecond spectral interferometry for applications in spectroscopy". In: *JOSA B* 12.12 (1995), pp. 2467–2474.

[78] John W Evans. "The birefringent filter". In: *JOSA* 39.3 (1949), pp. 229–242.

[79] Phillip Donald Keathley. "Engineering strong-field phenomena: From attosecond pulse characterization to nanostructured electron emitters". PhD thesis. Massachusetts Institute of Technology, 2015.

[80] R Clark Jones. "A new calculus for the treatment of optical systemsv. A more general formulation, and description of another calculus". In: *JOSA* 37.2 (1947), pp. 107–110.

[81] Valérie Véniard, Richard Taıeb, and Alfred Maquet. "Phase dependence of (N+ 1)-color (N> 1) ir-uv photoionization of atoms with higher harmonics". In: *Physical Review A* 54.1 (1996), p. 721.

[82] Howard R Reiss. "Effect of an intense electromagnetic field on a weakly bound system". In: *Physical Review A* 22.5 (1980), p. 1786.

[83] Andreas Becker and Farhad HM Faisal. "Intense-field many-body S-matrix theory". In: *Journal of Physics B: Atomic, Molecular and Optical Physics* 38.3 (2005), R1.

[84] Ahmed H Zewail. *Femtochemistry: Ultrafast Dynamics of the Chemical Bond (World Scientific Series in 20th Century Chemistry)*. World Scientific, 1994.

[85] Herschel Rabitz, Regina de Vivie-Riedle, Marcus Motzkus, and Karl Kompa. "Whither the future of controlling quantum phenomena?" In: *Science* 288.5467 (2000), pp. 824–828.

[86] Andrew M Weiner. "Ultrafast optical pulse shaping: A tutorial review". In: *Optics Communications* 284.15 (2011), pp. 3669–3692.

[87] Markus Kitzler and Stefanie Gräfe. "Ultrafast Dynamics Driven by Intense Light Pulses". In: *Springer Series on Atomic, Optical, and Plasma Physics* 86 (2016).

[88] Giuseppe Sansone, F Kelkensberg, JF Pérez-Torres, Felipe Morales, Matthias F Kling, W Siu, Omair Ghafur, Per Johnsson, Marko Swoboda, Enrico Benedetti, et al. "Electron localization following attosecond molecular photoionization". In: *Nature* 465.7299 (2010), pp. 763–766.

[89] Predrag Ranitovic, Craig W Hogle, Paula Rivière, Alicia Palacios, Xiao-Ming Tong, Nobuyuki Toshima, Alberto González-Castrillo, Leigh Martin, Fernando Martın, Margaret M Murnane, et al. "Attosecond vacuum UV coherent control of molecular dynamics". In: *Proceedings of the National Academy of Sciences* 111.3 (2014), pp. 912–917.

[90] David Busto, Jimmy Vinbladh, Shiyang Zhong, Marcus Isinger, Saikat Nandi, Sylvain Maclot, Per Johnsson, Mathieu Gisselbrecht, Anne L'Huillier, Eva Lindroth, et al. "Fano's propensity rule in angle-resolved attosecond pump-probe photoionization". In: *Physical review letters* 123.13 (2019), p. 133201.

[91] Rodrigo Lopez-Martens, Katalin Varjú, Per Johnsson, Johan Mauritsson, Yann Mairesse, Pascal Salieres, Mette B Gaarde, Kenneth J Schafer, Anders Persson, Sune Svanberg, et al. "Amplitude and phase control of attosecond light pulses". In: *Physical Review Letters* 94.3 (2005), p. 033001.

[92] N Dudovich, Olga Smirnova, J Levesque, Yu Mairesse, M Yu Ivanov, DM Villeneuve, and Paul B Corkum. "Measuring and controlling the birth of attosecond XUV pulses". In: *Nature physics* 2.11 (2006), pp. 781–786.

[93] Johan Mauritsson, Per Johnsson, E Gustafsson, Anne L'Huillier, KJ Schafer, and MB Gaarde. "Attosecond pulse trains generated using two color laser fields". In: *Physical review letters* 97.1 (2006), p. 013001.

[94] Erik Mansten, JM Dahlström, Per Johnsson, Marko Swoboda, Anne L'Huillier, and Johan Mauritsson. "Spectral shaping of attosecond pulses using two-colour laser fields". In: *New Journal of Physics* 10.8 (2008), p. 083041.

[95] G Doumy, J Wheeler, C Roedig, R Chirla, P Agostini, and LF DiMauro. "Attosecond synchronization of high-order harmonics from midinfrared drivers". In: *Physical review letters* 102.9 (2009), p. 093002.

[96] JM Dahlström, Thomas Fordell, Erik Mansten, T Ruchon, Marko Swoboda, Kathrin Klünder, Mathieu Gisselbrecht, Anne L'Huillier, and Johan Mauritsson. "Atomic and macroscopic measurements of attosecond pulse trains". In: *Physical Review A* 80.3 (2009), p. 033836.

[97] Xinkui He, JM Dahlström, Rafal Rakowski, CM Heyl, Anders Persson, Johan Mauritsson, and Anne L'Huillier. "Interference effects in two-color high-order harmonic generation". In: *Physical Review A* 82.3 (2010), p. 033410.

[98] Cheng Jin, Guoli Wang, Anh-Thu Le, and CD Lin. "Route to optimal generation of soft X-ray high harmonics with synthesized two-color laser pulses". In: *Scientific reports* 4 (2014), p. 7067.

[99] C Chen, Carlos Hernández-Garcıa, Z Tao, Wenjing You, Yingchao Zhang, Dmitriy Zusin, Christian Gentry, P Tengdin, A Becker, A Jaron-Becker, et al. "Influence of microscopic and macroscopic effects on attosecond pulse generation using two-color laser fields". In: *Optics Express* 25.23 (2017), pp. 28684–28696.

[100] Sambit Mitra, Shubhadeep Biswas, Johannes Schötz, Emilio Pisanty, Benjamin Förg, Gautam Aditya Kavuri, Christian Burger, William Okell, Maximilian Högner, Ioachim Pupeza, et al. "Suppression of individual peaks in two-colour high harmonic generation". In: *Journal of Physics B: Atomic, Molecular and Optical Physics* 53.13 (2020), p. 134004.

[101] Kai-Jun Yuan and André D Bandrauk. "Single circularly polarized attosecond pulse generation by intense few cycle elliptically polarized laser pulses and terahertz fields from molecular media". In: *Physical review letters* 110.2 (2013), p. 023003.

[102] Lukas Medišauskas, Jack Wragg, Hugo van der Hart, and Misha Yu Ivanov. "Generating isolated elliptically polarized attosecond pulses using bichromatic counterrotating circularly polarized laser fields". In: *Physical Review Letters* 115.15 (2015), p. 153001.

[103] A Ferré, C Handschin, M Dumergue, F Burgy, A Comby, D Descamps, B Fabre, GA Garcia, R Géneaux, L Merceron, et al. "A table-top ultrashort light source in the extreme ultraviolet for circular dichroism experiments". In: *Nature Photonics* 9.2 (2015), pp. 93–98.

[104] Ofer Kfir, Patrik Grychtol, Emrah Turgut, Ronny Knut, Dmitriy Zusin, Dimitar Popmintchev, Tenio Popmintchev, Hans Nembach, Justin M Shaw, Avner Fleischer, et al. "Generation of bright phase-matched circularly-polarized extreme ultraviolet high harmonics". In: *Nature Photonics* 9.2 (2015), pp. 99–105.

[105] Kevin M Dorney, Jennifer L Ellis, Carlos Hernández-Garcıa, Daniel D Hickstein, Christopher A Mancuso, Nathan Brooks, Tingting Fan, Guangyu Fan, Dmitriy Zusin, Christian Gentry, et al. "Helicity-selective enhancement and polarization control of attosecond high harmonic waveforms driven by bichromatic circularly polarized laser fields". In: *Physical Review Letters* 119.6 (2017), p. 063201.

[106] Álvaro Jiménez-Galán, Nick Zhavoronkov, David Ayuso, Felipe Morales, Serguei Patchkovskii, Marcel Schloz, Emilio Pisanty, Olga Smirnova, and Misha Ivanov. "Control of attosecond light polarization in two-color bicircular fields". In: *Physical Review A* 97.2 (2018), p. 023409.

[107] Genevieve Gariepy, Jonathan Leach, Kyung Taec Kim, Thomas J Hammond, Eugene Frumker, Robert W Boyd, and Paul B Corkum. "Creating high-harmonic beams with controlled orbital angular momentum". In: *Physical review letters* 113.15 (2014), p. 153901.

[108] Y Mairesse, A De Bohan, LJ Frasinski, H Merdji, LC Dinu, P Monchicourt, P Breger, M Kovačev, R Taıeb, B Carré, et al. "Attosecond synchronization of high-harmonic soft x-rays". In: *Science* 302.5650 (2003), pp. 1540–1543.

[109] Pengfei Wei, Jing Miao, Zhinan Zeng, Chuang Li, Xiaochun Ge, Ruxin Li, and Zhizhan Xu. "Selective enhancement of a single harmonic emission in a driving laser field with subcycle waveform control". In: *Physical review letters* 110.23 (2013), p. 233903.

[110] KR Hamilton, HW van der Hart, and AC Brown. "Pulse-shape control of two-color interference in high-order-harmonic generation". In: *Physical Review A* 95.1 (2017), p. 013408.

[111] VA Birulia and VV Strelkov. "Spectral caustic in two-color high-order harmonic generation: Role of Coulomb effects". In: *Physical Review A* 99.4 (2019), p. 043413.

[112] Yu-Chen Cheng, Sara Mikaelsson, Saikat Nandi, Lisa Rämisch, Chen Guo, Stefanos Carlström, Anne Harth, Jan Vogelsang, Miguel Miranda, Cord L Arnold, et al. "Controlling photoionization using attosecond time-slit interferences". In: *Proceedings of the National Academy of Sciences* 117.20 (2020), pp. 10727–10732.

[113] Yi-Yian Yin, Ce Chen, DS Elliott, and AV Smith. "Asymmetric photoelectron angular distributions from interfering photoionization processes". In: *Physical review letters* 69.16 (1992), p. 2353.

[114] Guillaume Laurent, Wei Cao, Itzik Ben-Itzhak, and Charles L Cocke. "Attosecond pulse characterization". In: *Optics express* 21.14 (2013), pp. 16914–16927.

[115] G Laurent, W Cao, I Ben-Itzhak, and CL Cocke. "Attosecond control of electron emission from atoms". In: *Journal of Physics: Conference Series*. Vol. 488. 1. IOP Publishing. 2014, p. 012008.

[116] John Vaughan, Joseph Bahder, Brady Unzicker, Davis Arthur, Morgan Tatum, Trevor Hart, Geoffrey Harrison, Spenser Burrows, Patrick Stringer, and Guillaume M Laurent. "Design of an optically-locked interferometer for attosecond pump-probe setups". In: *Optics express* 27.21 (2019), pp. 30989–31000.

[117] I Jong Kim, Chul Min Kim, Hyung Taek Kim, Gae Hwang Lee, Yong Soo Lee, Ju Yun Park, David Jaeyun Cho, and Chang Hee Nam. "Highly efficient high-harmonic generation in an orthogonally polarized two-color laser field". In: *Physical Review Letters* 94.24 (2005), p. 243901.

[118] Maciej Lewenstein, Pascal Salieres, and Anne L'huillier. "Phase of the atomic polarization in high-order harmonic generation". In: *Physical Review A* 52.6 (1995), p. 4747.

[119] Phillip Donald Keathley, Siddharth Bhardwaj, J Moses, G Laurent, and Franz X Kaertner. "Volkov transform generalized projection algorithm for attosecond pulse characterization". In: *New Journal of Physics* 18.7 (2016), p. 073009.

[120] Volker Schmidt. "Photoionization of atoms using synchrotron radiation". In: *Reports on Progress in Physics* 55.9 (1992), p. 1483.

[121] Diego Guenot, Kathrin Klünder, CL Arnold, David Kroon, JM Dahlström, Miguel Miranda, Thomas Fordell, Mathieu Gisselbrecht, Per Johnsson, Johan Mauritsson, et al. "Photoemission-time-delay measurements and calculations close to the 3 s-ionization-cross-section minimum in ar". In: *Physical Review A* 85.5 (2012), p. 053424.

[122] Caryn Palatchi, J Marcus Dahlström, AS Kheifets, IA Ivanov, DM Canaday, P Agostini, and LF DiMauro. "Atomic delay in helium, neon, argon and krypton". In: *Journal of Physics B: Atomic, Molecular and Optical Physics* 47.24 (2014), p. 245003.

[123] Diego Guenot, David Kroon, E Balogh, Esben Witting Larsen, Marija Kotur, M Miranda, Thomas Fordell, Per Johnsson, Johan Mauritsson, Mathieu Gisselbrecht, et al. "Measurements of relative photoemission time delays in noble gas atoms". In: *Journal of Physics B: Atomic, Molecular and Optical Physics* 47.24 (2014), p. 245602.

[124] Leonard Eisenbud. "The formal properties of nuclear collisions." In: *Ph. D. Thesis* (1948).

[125] Felix T Smith. "Lifetime matrix in collision theory". In: *Physical Review* 118.1 (1960), p. 349.

[126] Carlos AA de Carvalho and Herch M Nussenzveig. "Time delay". In: *Physics Reports* 364.2 (2002), pp. 83–174.

[127] J Marcus Dahlström, Diego Guénot, Kathrin Klünder, Matthieu Gisselbrecht, Johan Mauritsson, Anne L'Huillier, Alfred Maquet, and Richard Taıeb. "Theory of attosecond delays in laser-assisted photoionization". In: *Chemical Physics* 414 (2013), pp. 53–64.

[128] J Marcus Dahlström and Eva Lindroth. "Study of attosecond delays using perturbation diagrams and exterior complex scaling". In: *Journal of Physics B: Atomic, Molecular and Optical Physics* 47.12 (2014), p. 124012.

[129] U Fano. "Propensity rules: An analytical approach". In: *Physical Review A* 32.1 (1985), p. 617.

[130] B. H. Bransden and C. J. Joachain. *Physics of atoms and molecules*. 2nd ed. Prentice Hall, 2003.

[131] ES Toma and HG Muller. "Calculation of matrix elements for mixed extreme-ultraviolet–infrared two-photon above-threshold ionization of argon". In: *Journal of Physics B: Atomic, Molecular and Optical Physics* 35.16 (2002), p. 3435.

[132] RG Houlgate, JB West, K Codling, and GV Marr. "The angular distribution of the 3p electrons and the partial cross section of the 3s electrons of argon from threshold to 70 eV". In: *Journal of Electron Spectroscopy and Related Phenomena* 9.2 (1976), pp. 205–209.

[133] Vincent Loriot, Alexandre Marciniak, Gabriel Karras, Baptiste Schindler, Gina Renois-Predelus, Isabelle Compagnon, Bruno Concina, Richard Brédy, Gulabi Celep, Christian Bordas, et al. "Angularly resolved RABBITT using a second harmonic pulse". In: *Journal of Optics* 19.11 (2017), p. 114003.

[134] Paul Hockett. "Angle-resolved RABBITT: theory and numerics". In: *Journal of Physics B: Atomic, Molecular and Optical Physics* 50.15 (2017), p. 154002.

[135] Filippo Campi, Helene Coudert-Alteirac, Miguel Miranda, Linnea Rading, Bastian Manschwetus, Piotr Rudawski, Anne L'Huillier, and Per Johnsson. "Design and test of a broadband split-and-delay unit for attosecond XUV-XUV pump-probe experiments". In: *Review of Scientific Instruments* 87.2 (2016), p. 023106.

[136] D Rivas, M Weidman, B Bergues, A Muschet, A Guggenmos, O Razskazovskaya, H Schröder, W Helml, G Marcus, R Kienberger, et al. "Generation of high-energy isolated attosecond pulses for XUV-pump/XUV-probe experiments at 100 eV". In: *High Intensity Lasers and High Field Phenomena*. Optical Society of America. 2016, HT1B–1.

[137] Ioannis Makos, I Orfanos, Arjun Nayak, Jasper Peschel, Balázs Major, Ioannis Liontos, Emmanuel Skantzakis, N Papadakis, Constantinos Kalpouzos, Mathieu Dumergue, et al. "A 10-gigawatt attosecond source for non-linear XUV optics and XUV-pump-XUV-probe studies". In: *Scientific reports* 10.1 (2020), pp. 1–18.